University of California

Los Angeles

Equatorial Magnetosonic Waves in the Earth's Inner Magnetosphere

A dissertation submitted in partial satisfaction

of the requirements for the degree

Doctor of Philosophy in Atmospheric and Oceanic Sciences

by

Qianli Ma

2015

Abstract of the Dissertation

Equatorial Magnetosonic Waves in the Earth's Inner Magnetosphere

by

Qianli Ma

Doctor of Philosophy in Atmospheric and Oceanic Sciences

University of California, Los Angeles, 2015

Professor Richard M. Thorne, Chair

This dissertation presents a systematic study of the equatorial magnetosonic waves in the Earth's inner magnetosphere, addressing important issues which include the global distribution, energy source, propagation properties, and potential scattering effects. Equatorial magnetosonic waves are highly oblique whistler-mode electromagnetic emissions between the proton gyrofrequency and the lower hybrid resonant frequency, widely distributed in the Earth's inner magnetosphere, and may potentially cause electron acceleration in the radiation belts. The recent equatorial spacecraft THEMIS and the Van Allen Probes provide excellent observations on equatorial plasma waves. A global survey of magnetosonic waves is performed using THEMIS wave data products. The statistics show that the most intense magnetosonic waves are distributed near the dayside outside the plasmapause, with maximum root-mean-square averaged wave amplitudes between 50 and 100 pT and occurrence rates between 10% and 40%. An instability analysis is performed on a typical magnetosonic wave and locally observed ion ring distribution event. The unstable ion ring distribution could provide free energy for the wave excitation outside the plasmapause or in the outer region of the plasmasphere. Although magnetosonic waves cannot be excited deep inside the plasmapause, the waves observed there can originate from the outer region and re-

main trapped in the plasmasphere. The wave perpendicular propagation analysis demonstrates the importance of wave trapping in explaining the wave existence in the plaspasphere. The magnetosonic waves can cause electron pitch angle and energy scattering via Landau resonance and transit time effects, which lead to electron acceleration in the radiation belts. The investigation of their influences on energetic electrons in the Earth's inner magnetosphere shows that the acceleration time scale is generally tens of days. Using both observational and modeling techniques, this thesis provides comprehensive information about equatorial magnetosonic waves in the inner magnetosphere.

The dissertation of Qianli Ma is approved.

Toshi Nishimura

Vassilis Angelopoulos

Larry R. Lyons

Richard M. Thorne, Committee Chair

University of California, Los Angeles

2015

Dedicated to my parents,

Hanhua Cheng and Shengcai Ma,

who love and support me wherever I go.

Table of Contents

1 Introduction **1**

1.1 The Earth's magnetosphere 1

1.2 Particle motion in the inner magnetosphere 3

1.3 Plasma waves in the inner magnetosphere 6

1.4 Magnetosonic waves and particles 9

1.5 Particle diffusion in the radiation belts 11

1.6 Summary 13

2 General properties of magnetosonic waves **24**

2.1 Observed properties of magnetosonic wave events in the Earth's magnetosphere 24

2.2 The cold plasma dispersion relation 26

2.3 Dispersion and polarization of magnetosonic waves 30

2.4 Properties of magnetosonic waves in the magnetosphere 32

3 Global distribution of equatorial magnetosonic waves observed by THEMIS **40**

3.1 Introduction 41

3.2 The THEMIS database and an observed magnetosonic event . . . 44

3.3 Magnetosonic wave amplitude distribution observed by THEMIS . 48

3.4 Magnetosonic wave occurrence rate distribution observed by THEMIS 51

3.5 Magnetosonic wave intensities at different frequency bands 53

3.6 Conclusions and discussions 54

4 Magnetosonic wave excitation by ion ring distributions in the inner magnetosphere 64

4.1 Introduction 66

4.2 THEMIS observations of the magnetosonic wave event and ion ring distributions 68

4.3 Magnetosonic instability analysis under typical plasma conditions 71

4.4 Wave normal angle dependence of magnetosonic wave instabilities 74

4.5 Total plasma density dependence of magnetosonic wave instabilities 75

4.6 Simulation of magnetosonic wave instabilities across the plasmapause boundary 76

4.7 Simulation of broad band magnetosonic wave instabilities 77

4.8 Discussions and Conclusions 79

5 Propagation of magnetosonic waves in the outer plasmasphere 88

5.1 Introduction 89

5.2 Perpendicular propagation of magnetosonic waves 92

5.3 Intense magnetosonic waves observed by the Van Allen probes . . 94

5.4 Trapping of magnetosonic waves in the plasmasphere 98

5.5 Magnetosonic waves trapped by local density structures 100

5.6 Summary 101

6 Electron scattering due to typical magnetosonic waves in the inner magnetosphere 109

6.1 Introduction 111

6.2 Global distribution of magnetosonic waves using recent Van Allen Probes data 114

6.3 Statistics about magnetosonic wave frequency spectrum 117
6.4 Analytical formula for electron scattering due to equatorial magnetosonic waves 118
6.5 Energy scattering rates due to typical magnetosonic waves 121
6.6 Electron PSD evolutions due to magnetosonic waves outside the plasmapause 122
6.7 Electron PSD evolutions due to magnetosonic waves inside the plasmapause 125
6.8 Summary 126

7 Summary and Future Works 139

7.1 Summary 139
7.2 Future works 143
7.2.1 The rising tone structures of magnetosonic waves 143
7.2.2 The relation between magnetosonic waves and proton distributions 145
7.2.3 The additional electron scattering effects due to magnetosonic waves in presence of other plasma waves 147

BIBLIOGRAPHY 150

List of Figures

1.1 The Earth's dipole magnetic field. R_0 is the equatorial radial distance, λ is the magnetic latitude, r is the distance from the field line to the center of the Earth. 15

1.2 The structure of the Earth's magnetosphere. [Figure from Wikipedia (http://en.wikipedia.org/wiki/Magnetosphere). Original bitmap from NASA. SVG rendering by Aaron Kaase.] 16

1.3 The twenty years variation of solar activities and radiation belt particle fluxes. (top) Yearly averaged sunspot number (black) and weekly averaged solar wind speed (red). (bottom) Monthly averaged electron flux at an energy of $\sim 2MeV$ as a function of L shell. The black line in the bottom panel is the monthly averaged Dst index. [*Li et al.*, 2013b] 17

1.4 The best fitting of the plasma density as a function of L shell based on the averaged plasma density of CRRES measurements. (a) Density at plasmatrough and at the local time of 3.5 UT; (b) density in the plasmasphere. The solid lines are fitting results, and the diamonds are averaged data at each L shell bins with standard variations. [*Sheeley et al.*, 2001] 18

1.5 An illustration about the particle's gyration, bounce, and drift behaviors in the Earth's radiation belts. [*Mars*, 2002] 19

1.6 Spatial distribution of important waves in the inner magnetosphere, in relation to the plasmasphere and the drift-paths of ring current (10-100 keV) electrons and ions and relativistic ($\geq$ 0.3 MeV) electrons. [*Thorne*, 2010] 20

1.7 The ion ring distribution near the dayside magnetosphere observed by THEMIS A around 03:11 UT on November 24, 2010. Phase space density is plotted as a function of parallel and perpendicular energies. [*Ma et al.*, 2013] 21

1.8 Schematic of magnetosonic wave geometry showing (a) obliquity, ray trajectory 'snaking' about the equator, equatorial confinement, and resultant extent of $k_{\|}$, (b) distribution of magnetic amplitude as a function of latitude, and (c) pitch angle scattering of $E_k = 300$ keV, $a_0 = 55°$ electrons due to magnetosonic waves. [*Bortnik and Thorne*, 2010] 22

1.9 The comparison between the observation and simulation of equatorially mirroring electron fluxes from 12:00 UT on 6 March to 12:00 UT on 16 March 2013. The Van Allen Probe observation of electron differential flux as a function of $L*$ for an energy of (a) 0.59 MeV, (b) 1.01 MeV, (c) 2.00 MeV, (d) 3.60 MeV, and (e) the Kyoto Kp index multiplied by 10 (black line), the hiss wave amplitude averaged over $L = 4$ to 5 (red line), and the EMIC wave amplitude with an intensity of $B_w^2 = 0.1\text{nT}^2$ when $Kp \geq 2$ (blue line). Full simulation results of electron differential flux as a function of $L*$ for an energy of (f) 0.59 MeV, (g) 1.01 MeV, (h) 2.00 MeV, (i) 3.60 MeV, and simulation of the electron differential flux evolution without EMIC wave scattering for an energy of (j) 3.60 MeV. [*Ma et al.*, 2015] 23

2.1 Example of data collected by Cluster 4 on 17 February 2002. From the top: (a) sum of the power-spectral densities of the three magnetic components, (b) sum of the power-spectral densities of the two electric components ; (c) ellipticity and (d) planarity are determined using the singular value decomposition of the magnetic spectral matrix. Universal time (UT) and position of the spacecraft are given on the bottom of the figure using the radial distance (R) in the Earth radii (R_E), magnetic dipole latitude (MLat) in degrees, and magnetic local time (MLT) in hours. Maximum possible value of the local lower hybrid frequency (f_{LHR}) is plotted over all four panels. The data in panels (c) and (d) are not shown for weak signals below $10^{-9} nT^2$ Hz. [*Santolík et al.*, 2004] 35

2.2 Magnetic power spectra as a function of wave frequency observed by Cluster 1, 2, and 3 between 16:40 and 16:50 UT on 4 December 2000. Vertical scale is drawn for Cluster 1 (black solid line), spectrum from Cluster 2 (red line) is shifted upward by half an order of magnitude, and the spectrum of Cluster 3 (green line) is shifted by an order of magnitude. [*Santolík et al.*, 2002] 36

2.3 Stix parameters P, R, L, S, and D, refractive index n, and absolute values of wave electric (E) and magnetic (B) field components for typical magnetosonic waves at $L = 4.5$ inside the plasmapause. The wave normal angle is 89.5°. Sheeley's density model is used. . 37

2.4 Stix parameters P, R, L, S, and D, refractive index n, and absolute values of wave electric (E) and magnetic (B) field components for typical magnetosonic waves at $L = 4.5$ outside the plasmapause. The wave normal angle is 89.5°. Sheeley's density model is used. . 38

2.5 Resonant ellipse for magnetosonic waves interacting with electrons, showing (dashed) Landau $n = 0$ and (solid) $n = 1$ Doppler shifted cyclotron resonances, (dotted) circles of constant electron energy, and (dash-dotted) loss cone. The central dashed line is for Landau resonance at $X_m = \tan 89°$, the lines either side are for propagation with a range of wave normal angles $X_m \pm X_w$ where X_m is the width. [*Horne et al.*, 2007] 39

3.1 Average wave electric field intensities of (top) equatorial and (bottom) off-equatorial emissions in the frequency range $0.5 f_{LHR} < f < f_{LHR}$ observed by CRRES outside the plasmasphere as a function of L and magnetic local time. From left to right the results are presented for quiet ($AE* < 100$ nT), moderate ($100 < AE* < 300$ nT), and active ($AE* > 300$ nT) conditions. [*Meredith et al.*, 2008] 58

3.2 Average wave electric field intensities of (top) equatorial and (bottom) off-equatorial emissions in the frequency range $0.5 f_{LHR} < f < f_{LHR}$ observed by CRRES in the plasmasphere as a function of L and magnetic local time. From left to right the results are presented for quiet ($AE* < 100$ nT), moderate ($100 < AE* < 300$ nT), and active ($AE* > 300$ nT) conditions. [*Meredith et al.*, 2008] 59

3.3 Magnetosonic waves observed by THEMIS A on 15 February 2011. The seven panels show: (a) the total plasma density; (b) energy spectrum of ion energy flux at a pitch angle of 90°; (c) the calculated energy spectrum of ion PSD; (d) power spectral density of $E_\perp$; (e) $E_\parallel$; (f) $B_\parallel$; (g) $B_\perp$. 60

3.4 The global distribution of RMS wave amplitude $B_{\rm w}$ for $2 < L < 8$. The wave intensity is categorized by magnetic latitude and AE*, and shown for locations inside (top panels) and outside (bottom panels) the plasmapause. The sample number ($N_{\rm s}$) is shown as smaller plots at the right bottom corner for each panel. White area represents the region where $N_{\rm s}$ is less than 100. 61

3.5 The global distribution of magnetosonic wave occurrence rate for $2 < L < 8$. The wave occurrence rate is categorized by magnetic latitude and wave amplitude range, and shown for locations inside (top panels) and outside (bottom panels) the plasmapause. The sample number is shown as smaller plots at the right bottom corner for each panel. White area represents the region where $N_{\rm s}$ is less than 100. 62

3.6 The global distribution of RMS wave amplitude $B_{\rm w}$ for higher and lower frequency band waves. The wave intensity is categorized by the frequency bands and AE*, and is shown inside (top panels) and outside (bottom panels) the plasmapause. The sample number is shown at the right bottom corner for each panel. White area represents the region where $N_{\rm s}$ is less than 100. 63

4.1 Magnetosonic waves observed by THEMIS A on 24 November 2010. (a) The total plasma density; (b) ion differential energy flux at a pitch angle of 90°; (c) ion PSD; (d) power spectral density of $E_{w\perp}$; (e) $E_{w\parallel}$; (f) $B_{w\parallel}$; and (g) $B_{w\perp}$ from wave spectra data. The 3 selected typical times are indicated by the vertical dashed lines. The red arrows in panel (c) indicate 3 examples of the positive gradients in ion PSD. 82

4.2 The observed ion PSD distributions in the parallel and perpendicular energy space (first row), the ion PSD at a pitch angle of 90° as a function of $E_\perp$ (second row), and the comparisons (third row) of the observed wave intensity (black) with the simulated wave growth rate (blue) as a function of normalized wave frequency. The analyses are performed at time 1 (first column), time 2 (second column), and time 3 (third column), respectively. 83

4.3 Magnetosonic wave growth rates (color-coded) as a function of normalized wave frequency and wave normal angle at time 1 (panel a) and time 2 (panel b). The white area represents the region without wave growth ($\gamma \leq 0$). Note that based on the relative values of E_R and E_A, the frequency of wave growth is different in the two regions. The frequency scale in the horizontal axis is also different in the two panels, adjusted accordingly. Also note that the wave normal angle scales are also different: they are wider on the right, consistent with the broader range of unstable wave normal angles. 84

4.4 Simulation of magnetosonic wave growth rates (blue) with different plasma densities of $0.667N$ (first column), N (second column), and $1.5N$ (third column) at time 1 (row 1) and time 2 (row 2), where N is the total plasma density inferred from the spacecraft potential. The observed wave intensity is indicated with a black line in each panel. 85

4.5 Comparison of the simulated wave growth rate spectrum and the observed magnetosonic wave spectrum on 24 November 2010. (a) Total plasma density; (b) ion PSD as a function of energy for a pitch angle of $\sim 90°$; (c) power spectral density of $B_{\parallel}$; (d) $B_{\perp}$; (e) simulated local wave growth rate. The other notions are the same as in Figure 1. The white area in (e) represents the region without significant wave growth (less than 0.5 dB/R_E). 86

4.6 Comparison of the simulated wave growth rate spectrum and the observed broad band magnetosonic wave spectrum on 19 October 2011. (a) Total plasma density; (b) differential ion energy flux for a pitch angle of $\sim 90°$; (c) energy spectrum of ion PSD for a pitch angle of $\sim 90°$; (d) power spectral density of $B_{\parallel}$; (e) $B_{\perp}$; (f) simulated local wave growth rate. The other notions are the same as in Figure 1. The white area in (f) represents the region without significant wave growth (less than 0.5 dB/R_E). 87

5.1 The radial calculation of $Q(\psi = 90°) = nL$ profile. (top) The assumed total plasma density model with a plasmapause at $L = 4.5$; (middle) the refractive index n; (bottom) the $Q(\psi = 90°) = nL$ profile as a function of L-shell. The dashed line in the bottom panel indicates the trapping region. 104

5.2 The examples of ray traces with an initial azimuthal angle of $\psi = 30°$ (red) and $\psi = 60°$ (blue) launched at $L = 4.5$. (top) The variations of wave azimuthal angle as a function of L-shell when the wave propagates; (bottom) the wave paths in the magnetic equatorial plane, showing the trapping of the waves in a limited radial region. 105

5.3 Magnetosonic waves observed by Van Allen Probe A on 04 December 2012 and the instability analysis. (a) The electric field power spectral density measured by HFR; (b) proton PSD as a function of energy for a pitch angle of 90°; (c) magnetic field power spectral density measured by WFR; (d) magnetic wave amplitudes of magnetosonic waves; (e) magnetosonic wave normal angles; (f) wave magnetic compressibility; (g) calculated magnetosonic wave local growth rates. In panel (c), the white solid line and the white dashed line represent f_{LHR} and $0.5f_{LHR}$ respectively. 106

5.4 Trapping region analysis of magnetosonic wave event on 04 December 2012. (a) The total plasma density; (b) magnetic field power spectral density; (c) azimuthal propagation angle; (d) wave magnetic field power spectral density at 43.79 Hz; (e) calculated $Q(\psi = 90°) = nL$ profile at 43.79 Hz; (f) estimated magnetosonic wave trapping region. In panels (b) and (c), the white solid line and the black dashed line represent f_{LHR} and 43.79 Hz respectively; In panel (e), the red two-way arrow represents the predicted trapping region at 43.79 Hz. 107

5.5 The local instability and trapping analysis of magnetosonic wave event on 06 November 2012. (a) The total plasma density; (b) proton PSD as a function of energy for a pitch angle of 90°; (c) magnetic field power spectral density; (d) wave ellipticity; (e) calculated magnetosonic wave local growth rates; (f) wave magnetic field power spectral density at 55.54 Hz; (g) calculated $Q(\psi = 90°) = nL$ profile at 55.54 Hz; (h) estimated magnetosonic wave trapping region. In panel (b), the white solid line and the black dotted line represent E_A and E_R respectively; In panel (g), the red two-way arrows represent the predicted trapping regions. 108

6.1 The Van Allen Probes observation of magnetosonic waves on 06 October 2012. (a) The AE index; (b) the electric field power spectral density measured by HFR; (c) the plasmapause indicator inferred from ECH wave intensities; (d) the magnetic field power spectral density measured by WFR; (e) the wave ellipticity; (f) the wave normal angle. The dotted, solid, and dashed lines in panel (b) represent $2f_{ce}$, f_{ce}, and $0.5f_{ce}$; the white dashed lines in panel (d) represent f_{LHR}, $0.5f_{LHR}$, and f_{cp}, respectively. 128

6.2 The global distribution of RMS wave amplitude B_{w} for $2 < L < 8$. The wave intensity is categorized by magnetic latitude and AE*, and shown for locations inside (top panels) and outside (bottom panels) the plasmapause. The sample number (N_{s}) is shown as smaller plots at the right bottom corner for each panel. White area represents the region where N_{s} is less than 100. 129

6.3 The global distribution of magnetosonic wave occurrence rate for $2 < L < 8$. The wave occurrence rate is categorized by magnetic latitude and wave amplitude range, and shown for locations inside (top panels) and outside (bottom panels) the plasmapause. The sample number is shown as smaller plots at the right bottom corner for each panel. White area represents the region where N_{s} is less than 100. 130

6.4 The survey of magnetosonic wave magnetic field power intensity inside the plasmapause, as a function of wave frequency at different L shells and different magnetic local time sectors. The two white solid lines represent f_{LHR} and f_{cp}; the black solid line represents the frequency with peak wave intensity; the two dashed lines represent the standard derivations of the wave power. 131

6.5 The survey of magnetosonic wave magnetic field power intensity outside the plasmapause, as a function of wave frequency at different L shells and different magnetic local time sectors. The two white solid lines represent f_{LHR} and f_{cp}; the black solid line represents the frequency with peak wave intensity; the two dashed lines represent the standard derivations of the wave power. 132

6.6 The calculated energy diffusion coefficients due to magnetosonic waves as a function of pitch angle and energy inside the plasmapause, at different L shells from $L = 3$ to $L = 6$. The statistical wave frequency spectra and the wave amplitudes inside the plasmapause during modestly disturbed conditions are used. The density model is Sheeley's density model inside the plasmapause [*Sheeley et al.*, 2001]. The energy diffusion coefficients are drift and bounce averaged. 133

6.7 The calculated energy diffusion coefficients due to magnetosonic waves as a function of pitch angle and energy outside the plasmapause, at different L shells from $L = 3$ to $L = 6$. The statistical wave frequency spectra and the wave amplitudes outside the plasmapause during modestly disturbed conditions are used. The density model is Sheeley's density model outside the plasmapause [*Sheeley et al.*, 2001]. The energy diffusion coefficients are drift and bounce averaged. 134

6.8 The pitch angle, absolute values of mixed pitch angle-momentum, and momentum diffusion coefficients as a function of pitch angle and energy calculated at $L = 4.5$ outside the plasmapause during disturbed conditions. Most of the mixed pitch angle-momentum diffusion coefficients are negative. The diffusion coefficients are drift and bounce averaged. 135

6.9 The 2D Fokker-Planck simulation of the energetic electron PSD evolution due to the interactions with magnetosonic waves during disturbed conditions outside the plasmapause, for a period of 4 days. The electron PSD are plotted as a function of pitch angle at different energies. The diffusion coefficients in Figure 6.8 are used. The initial electron PSD distributions are normalized and assumed to be Kappa distribution with $\kappa = 6$. 136

6.10 The pitch angle, absolute values of mixed pitch angle-momentum, and momentum diffusion coefficients as a function of pitch angle and energy calculated at $L = 4.5$ inside the plasmapause during disturbed conditions. Most of the mixed pitch angle-momentum diffusion coefficients are negative. The diffusion coefficients are drift and bounce averaged. 137

6.11 The 2D Fokker-Planck simulation of the energetic electron PSD evolution due to the interactions with magnetosonic waves during disturbed conditions inside the plasmapause, for a period of 4 days. The electron PSD are plotted as a function of pitch angle at different energies. The diffusion coefficients in Figure 6.10 are used. The initial electron PSD distributions are normalized and assumed to be Kappa distribution with $\kappa = 6$. 138

7.1 The rising tone structures of magnetosonic waves observed by the Van Allen Probes on 30 October 2012. (a) The wave electric intensity spectrogram measured by HFR; (b) the proton PSD as a function of energy at a pitch angle of 90°; (c) the wave electric field power spectral density measured by WFR; (d) the wave magnetic field power spectral density measured by WFR; (e) wave normal angle. The dashed lines in panels (c) and (d) represent f_{LHR} and $0.5f_{LHR}$, respectively. 149

Acknowledgments

I own my greatest gratitude to my advisor, Prof. Richard M. Thorne, who has always been passionate about space sciences research, enthusiastic in guiding my Ph.D. researches, and excellent in spreading his scientific insights during the lectures. This thesis would not have been possible without his continuous guidance and support.

I would like to thank my thesis committee members, Prof. Larry R. Lyons, Prof. Vassilis Angelopoulos, and Dr. Toshi Nishimura, who have taught me space sciences from the most basic element, gave me valuable tips during each presentation, and provided me helpful research guidance.

I really appreciate the great space science group at the Atmospheric and Oceanic Sciences department in UCLA. My special acknowledgement goes to Dr. Wen Li, for the numerous helpful discussions and guidance through each of my thesis projects. I would like to thank Prof. Lunjin Chen and Prof. Binbin Ni, for their help in performing the scientific simulations. I would also like to thank the other space science group members (Jacob Bortnik, Xin Tao, Maria de Soria-Santacruz Pich, Chih-Ping Wang, Yuri Y. Shprits, Xiaojia Zhang, Xiaoyan Xing, Heejeong Kim, Xin An, Ying Zou, Beatriz Gallardo-Lacourt, Chao Yue, Jinxing Li, Xinliang Gao, etc.), who have provided me helpful comments during my Ph.D. thesis research. I am grateful for the excellent space science group and the enjoyable years in our department.

Finally, I would like to thank my parents, who have shared with me their endless love and encouragement.

Qianli Ma

May 2015

Section 1.5 is a version of 'Ma, Q., Li, W., Thorne, R. M., Ni, B., Kletzing, C. A., Kurth, W. S., Hospodarsky, G. B., Reeves, G. D., Henderson, M. G., Spence, H. E., Baker, D. N., Blake, J. B., Fennell, J. F., Claudepierre, S. G. and Angelopoulos, V. (2015), Modeling inward diffusion and slow decay of energetic electrons in the Earth's outer radiation belt. *Geophys. Res. Lett.*, *42*, 987995. doi: 10.1002/2014GL062977'.

Chapter 3 is a version of 'Ma, Q., W. Li, R. M. Thorne, and V. Angelopoulos (2013), Global distribution of equatorial magnetosonic waves observed by THEMIS, *Geophys. Res. Lett.*, *40*, 1895-1901, doi:10.1002/grl.50434'.

Chapter 4 is a version of 'Ma, Q., W. Li, L. Chen, R. M. Thorne, and V. Angelopoulos (2014), Magnetosonic wave excitation by ion ring distributions in the Earth's inner magnetosphere, *J. Geophys. Res. Space Physics*, *119*, 844852, doi:10.1002/2013JA019591'.

Chapter 5 is a version of 'Ma, Q., W. Li, L. Chen, R. M. Thorne, C. A. Kletzing, W. S. Kurth, G. B. Hospodarsky, G. D. Reeves, M. G. Henderson, and H. E. Spence (2014), The trapping of equatorial magnetosonic waves in the Earth's outer plasmasphere, *Geophys. Res. Lett.*, *41*, 63076313, doi:10.1002/2014GL061414'.

I acknowledge NASA grants NNX11AR64G and by JHU/APL contracts 967399 and 921647 under NASA's prime contract NAS5-01072, and NSF grants AGS-1103064, AGS-1405041 and AGS-1405054. The Van Allen probes data analysis at UCLA was supported by the EMFISIS sub-award 1001057397:01 and by the ECT sub-award 13-041. I acknowledge NASA contract NAS5-02099 for the use of data from the THEMIS Mission. I thank the World Data Center for Geomagnetism, Kyoto for providing geomagnetic indices. The Van Allen Probes data from the EMFISIS instrument is available from http://emfisis.physics.uiowa.edu/data/index/, and data from the HOPE, MagEIS and REPT instruments are available from http://www.rbsp-ect.lanl.gov/data_pub/; the THEMIS data is available from http://themis.ssl.berkeley.edu/data/themis/; the Kyoto geomagnetic indices are

available at http://wdc.kugi.kyoto-u.ac.jp/.

Vita

2006–2010	Bachelor of Science, Department of Earth and Space Sciences, University of Science and Technology of China.
2010–2012	Master of Science, Department of Atmospheric and Oceanic Sciences, University of California, Los Angeles.
2012	Teaching Assistant, Department of Atmospheric and Oceanic Sciences, University of California, Los Angeles.
2011-2015	Graduate Student Researcher, Department of Atmospheric and Oceanic Sciences, University of California, Los Angeles.

Publications

1. Baker, D. N., A. N. Jaynes, V. C. Hoxie, R. M. Thorne, J. C. Foster, X. Li, J. F. Fennell, J. R. Wygant, S. G. Kanekal, P. J. Erickson, W. Kurth, W. Li, **Q. Ma**, Q. Schiller, L. Blum, D. M. Malaspina, A. Gerrard, L. J. Lanzerotti (2014), An impenetrable barrier to ultrarelativistic electrons in the Van Allen radiation belts, *Nature*, *515*, 531-534, doi:10.1038/nature13956.

2. Gao, X., W. Li, J. Bortnik, R. M. Thorne, Q. Lu, **Q. Ma**, X. Tao, and S. Wang (2015), The effect of different solar wind parameters upon significant relativistic electron flux dropouts in the magnetosphere. *J. Geophys. Res. Space Physics*, *120*, doi: 10.1002/2015JA021182.

3. Li, J., Binbin Ni, L. Xie, Z. Pu, J. Bortnik, R. M. Thorne, L. Chen, **Q. Ma**, S. Fu, Q. Zong, X.Wang, C. Xiao, Z. Yao, and R. Guo (2014), Interactions between magnetosonic waves and radiation belt electrons: Comparisons of quasi-linear calculations with test particle simulations, *Geophys. Res. Lett.*, *41*, 4828-4834, doi:10.1002/2014GL060461.

4. Li, W., R. M. Thorne, **Q. Ma**, B. Ni, J. Bortnik, D. N. Baker, H. E. Spence, G. D. Reeves, S. G. Kanekal, J. C. Green, C. A. Kletzing, W. S. Kurth, G. B. Hospodarsky, J. B. Blake, J. F. Fennell, and S. G. Claudepierre (2014), Radiation belt electron acceleration by chorus waves during the 17 March 2013 storm, *J. Geophys. Res. Space Physics*, *119*, 4681-4693, doi:10.1002/2014JA019945.

5. Li, W., **Q. Ma**, R. M. Thorne, J. Bortnik, C. A. Kletzing, W. S. Kurth, G. B. Hospodarsky, and Y. Nishimura (2015), Statistical properties of plasmaspheric hiss derived from Van Allen Probes data and their Effects on radiation belt electron dynamics, *J. Geophys. Res. Space Physics*, *120*, doi:10.1002/2015JA021048.

6. **Ma, Q.**, and C. Chen. The Communicating Pipe Model for Icy Plumes in Enceladus (2009), *Chinese Physics Letters*, *26*, 11, 119601-1 – 119601-4.

7. **Ma, Q.**, B. Ni, X. Tao, and R. M. Thorne, Evolution of the plasma sheet electron pitch angle distribution by whistler-mode chorus waves in non-dipole magnetic fields (2012), *Ann. Geophys.*, *30*, 751-760, doi:10.5194/angeo-30-751-2012.

8. **Ma, Q.**, W. Li, R. M. Thorne, and V. Angelopoulos (2013), Global distribution of equatorial magnetosonic waves observed by THEMIS, *Geophys. Res. Lett.*, *40*, 1895-1901, doi:10.1002/grl.50434.

9. **Ma, Q.**, W. Li, L. Chen, R. M. Thorne, and V. Angelopoulos (2014), Magnetosonic wave excitation by ion ring distributions in the Earth's inner magnetosphere, *J. Geophys. Res. Space Physics*, *119*, 844-852, doi:10.1002/2013JA019591.

10. **Ma, Q.**, W. Li, L. Chen, R. M. Thorne, C. A. Kletzing, W. S. Kurth, G. B. Hospodarsky, G. D. Reeves, M. G. Henderson, and H. E. Spence (2014), The trapping of equatorial magnetosonic waves in the Earth's outer plasmasphere, *Geophys. Res. Lett.*, *41*, 6307-6313, doi:10.1002/2014GL061414.

11. **Ma, Q.**, W. Li, R. M. Thorne, B. Ni, C. A. Kletzing, W. S. Kurth, G. B. Hospodarsky, G. D. Reeves, M. G. Henderson, H. E. Spence, D. N. Baker, J. B. Blake, J. F. Fennell, S. G. Claudepierre, and V. Angelopoulos, Modeling inward diffusion and slow decay of energetic electrons in the Earth's outer radiation belt, *Geophys. Res. Lett.*, *42*, 987995, doi:10.1002/2014GL062977.

12. de Soria-Santacruz, M. , W. Li, R. M. Thorne, **Q. Ma,**, J. Bortnik, B. Ni, C. A. Kletzing, W. S. Kurth, G. B. Hospodarsky, H. E. Spence, G. D. Reeves, J. B. Blake, and J. F. Fennell (2015), Analysis of plasmaspheric hiss wave amplitudes inferred from low-altitude POES electron data: Technique sensitivity analysis, *J. Geophys. Res. Space Physics*, *120*,

doi:10.1002/2014JA020941.

13. Ni, B., J. Bortnik, R. M. Thorne, **Q. Ma**, and L. Chen (2013), Resonant scattering and resultant pitch angle evolution of relativistic electrons by plasmaspheric hiss, *J. Geophys. Res. Space Physics*, *118*, 7740-7751, doi:10.1002/2013JA019260.

14. Ni, B., W. Li, R. M. Thorne, J. Bortnik, **Q. Ma**, L. Chen, C. A. Kletzing, W. S. Kurth, G. B. Hospodarsky, G. D. Reeves, H. E. Spence, J. Bernard Blake, J. F. Fennell, and S. G. Claudepierre (2014), Resonant scattering of energetic electrons by unusual low-frequency hiss, *Geophys. Res. Lett.*, *41*, 1854-1861, doi:10.1002/2014GL059389.

15. Thorne, R. M., W. Li, B. Ni, **Q. Ma**, J. Bortnik, D. N. Baker, H. E. Spence, G. D. Reeves, M. G. Henderson, C. A. Kletzing, W. S. Kurth, G. B. Hospodarsky, D. Turner, and V. Angelopoulos (2013), Evolution and slow decay of an unusual narrow ring of relativistic electrons near L 3.2 following the September 2012 magnetic storm, *Geophys. Res. Lett.*, *40*, 3507-3511, doi:10.1002/grl.50627.

16. Thorne, R. M., W. Li, B. Ni, **Q. Ma**, J. Bortnik, L. Chen, D. N. Baker, H. E. Spence, G. D. Reeves, M. G. Henderson, C. A. Kletzing, W. S. Kurth, G. B. Hospodarsky, J. B. Blake, J. F. Fennell, S. G. Claudepierre, S. G. Kanekal (2013), Rapid local acceleration of relativistic radiation-belt electrons by magnetospheric chorus, *Nature*, *504*, 411-414, doi:10.1038/nature12889.

17. Turner, D. L., V. Angelopoulos, W. Li, J. Bortnik, B. Ni, **Q. Ma**, R. M. Thorne, S. K. Morley, M. G. Henderson, G. D. Reeves, M. Usanova, I. R. Mann, S. G. Claudepierre, J. B. Blake, D. N. Baker, C.-L. Huang, H. Spence, W. Kurth, C. Kletzing, and J. V. Rodriguez (2014), Competing source and loss mechanisms due to wave-particle interactions in Earth's outer radiation belt during the 30 September to 3 October 2012 geomagnetic storm, *J. Geophys. Res. Space Physics*, *119*, 1960-1979, doi:10.1002/2014JA019770.

Presentations

1. **Ma, Q.**, B. Ni, X. Tao, R. M. Thorne, Comparison of Dipole and Dungey Model Effects, paper presented in Geospace Environment Modeling meeting, June 2011, Santa Fe, NM.

2. **Ma, Q.**, B. Ni, X. Tao, R. M. Thorne, Evolution of the plasma sheet electron pitch angle distribution by whistler-mode chorus waves in non-dipole magnetic fields, paper presented in American Geophysical Union fall meeting, December 2011, San Francisco, CA.

3. **Ma, Q.**, W. Li, and R. M. Thorne, Statistical results of the magnetosonic waves observed by the THEMIS spacecraft, paper presented in Geospace Environment Modeling meeting, June 2012, Snowmass, CO.

4. **Ma, Q.**, W. Li, R. M. Thorne, and V. Angelopoulos, Typical MS events and the global distribution observed by THEMIS spacecraft, paper presented in American Geophysical Union fall meeting, December 2012, San Francisco, CA.

5. **Ma, Q.**, W. Li, L. Chen, R. M. Thorne, and V. Angelopoulos, Magnetosonic (MS) wave excitation by the ion ring distribution, paper presented in Geospace Environment Modeling meeting, June 2013, Snowmass, CO.

6. **Ma, Q.**, W. Li, L. Chen, R. M. Thorne, and V. Angelopoulos, Excitation of magnetosonic waves by the ion ring distributions in the inner magnetosphere, paper presented in American Geophysical Union fall meeting, December 2013, San Francisco, CA.

7. **Ma, Q.**, W. Li, L. Chen, R. M. Thorne, Trapping of magnetosonic waves in the Earth's inner magnetosphere, paper presented in Geospace Environment Modeling meeting, June 2014, Norfolk, VA.

8. **Ma, Q.**, W. Li, R. M. Thorne, and V. Angelopoulos, Global distribution of magnetosonic waves in the Earth's magnetosphere, paper presented in Geospace Environment Modeling meeting, June 2014, Norfolk, VA.

9. **Ma, Q.**, The recent observation of plasma waves and particles in the inner magnetosphere, paper presented in Geospace Environment Modeling meeting, June 2014, Norfolk, VA.

10. **Ma, Q.**, W. Li, R. M. Thorne, and B. Ni, The inward radial diffusion and slow decay of energetic electrons in the Earths radiation belts, American Geophysical Union fall meeting, December 2014, San Francisco, CA.

11. **Ma, Q.**, Equatorial magnetosonic waves in the Earth's inner magnetosphere, paper presented in AOS 270 seminar, UCLA, March 2015, Los Angeles, CA.

12. **Ma, Q.**, R. M. Thorne, W. Li, and J. Bortnik, Electron scattering due to typical magnetosonic (MS) waves using analytical formula, paper presented in Inner Magnetosphere Coupling meeting III, March 2015, Los Angeles, CA.

13. **Ma, Q.**, W. Li, R. M. Thorne, J. Bortnik, and L. Chen, Global distribution, energy source, and scattering effects of equatorial magnetosonic waves in the Earth's inner magnetosphere, invited talk at AGU Joint Assembly 2015, May 2015, Montreal, QC, Canada.

CHAPTER 1

Introduction

The Earth's inner magnetosphere is home to many spacecraft, which are influenced by the dynamic variability of the radiation belts. Such variability is associated with disturbances on the Sun and coupled to phenomena in the upper atmosphere. This is a brief introduction about the Earth's inner magnetosphere. We will specifically discuss the structure of the Earth's magnetosphere and it's relation with the ambient solar wind influences, the motion and drift path of charged particles in the inner magnetosphere, the important plasma waves and their interactions with the particles, and particle diffusion processes in the radiation belts.

1.1 The Earth's magnetosphere

The magnetosphere is a space area where the Earth's intrinsic magnetic field dominates the motion of charged particles. It expends from several hundred kilometers above the Earth's surface to about ten earth radii (1 $R_E \sim 6370$ km) at the subsolar point near the dayside. The magnetosphere naturally forms a shield for the planet Earth from the direct impacts of outside solar winds [*Kivelson and Russell*, 1995].

The dominant component of the Earth's intrinsic magnetic field is a dipolar magnetic field. The geometry of dipole field line is illustrated in Figure 1.1 and expressed as $r = R_0 \cos^2 \lambda$, where r is the distance from the Earth's center to the field line, R_0 is the equatorial distance on the same field line, and λ is the latitude.

The Earth's magnetic dipole moment is $M_p = 7.9 \times 10^{23}$ cm$^3 G$, and the magnetic field strength near the equator at the surface is about 0.3 G. The magnetic field strength at an equatorial distance of R_0 is $B_0 = M_p/R_0^3$.

The Earth's space environment is significantly influenced by the solar activities [e.g., *Akasofu and Kamide*, 1987]. Solar wind is a stream of tenuous plasma continuously flows from the upper atmosphere of the sun towards the interplanetary region. When the solar wind encounters the Earth's magnetosphere, the bow shock is formed to decelerate the supersonic solar wind flow. As a consequence, the Earth's magnetic fields become distorted, compressed at the sunward direction and elongated at the anti-sunward direction. A sketch of the Earth's distorted magnetosphere is presented in Figure 1.2. The solar wind flow velocity is reduced and deflected in the magnetosheath after impinging on the bow shock. Magnetopause forms as a balance between the solar wind dynamic pressure and the Earth's magnetic pressure, and is the outer boundary of the Earth's magnetosphere. At the distant anti-sunward direction, the magnetosphere has a tail-like structure. The magnetic fields in the northern lobe point towards the Earth, and the fields in the southern lobe direct towards the tail. The northern and southern lobes are separated by plasma sheet, which is a sheet-like region containing denser plasma and lower magnetic fields near the magnetic equator. The plasma transport and particle injection from the tail plasma sheet to the near Earth region cause geomagnetic disturbances.

The Earth's inner magnetosphere generally refers to the region below $\sim 8R_E$, which is closely related to the dynamics of the upper atmosphere. The electrons and ions are injected from the nightside plasma sheet and drift around in the inner magnetosphere. The energetic electrons are subsequently trapped by the Earth's magnetic fields and form the radiation belts, which may become hazardous to the nearby spacecraft. The existence of radiation belts is first confirmed by Explorer 1 and Explorer 3 as early as the year 1958 [*Van Allen and Frank*, 1959], and the

Earth's radiation belts present a two-zone structure in equilibrium state [*Lyons and Thorne*, 1973]. The dynamics of the Earth's inner magnetosphere is strongly affected by the variations in the solar activities, as shown in twenty years variations in Figure 1.3. The top panel in Figure 1.3 presents the sunspot number (black line), which is an evaluation of the solar activity, and the solar wind speed (red line). The sunspot number shows clearly the 11 year solar cycle variations. The bottom panel presents the $\sim$ 2 MeV electron fluxes as a function of L shell, and Disturbance storm time (Dst) index (black line) which is a measure of geomagnetic storm activities. Here L is the equatorial distance of the field line in units of R_E if the magnetic field was adiabatically released into a dipole magnetic field. The radiation belt particles are highly variable during the 20 years, and the variations are closely associated with the sunspot number and solar wind pressure variations.

Thermal particles are completely dominated by the Earth's geomagnetic fields and co-rotate with the Earth in the plasmasphere. Plasmasphere is a region that contains dense (higher than $100/\text{cm}^{-3}$) and low energy (several eV) electrons, with contrast to the plasmatrough where the plasma density drops one order lower. The plasmasphere extends from the top of the ionosphere to about 6 R_E during geomagnetically quiet periods. The outer boundary of the plasmasphere is the plasmapause. Figure 1.4 shows the empirical best fitting of the CRRES measured density as a function of L shell [*Sheeley et al.*, 2001]. For a virtual plasmapause located at $L = 4.6$, the plasma density drops from ~ 100 cm^{-3} to ~ 10 cm^{-3}. The Sheeley's plasmasphere density model is commonly used to provide an estimate of the plasmaspheric density, which is expressed as $n_e = 1390 \times (3/L)^{4.83}$ [cm^{-3}].

1.2 Particle motion in the inner magnetosphere

The dynamics of the charged particle are mainly affected by the electric (E) and magnetic (B) fields in the Earth's inner magnetosphere [e.g., *Walt*, 1994]. The

source of the magnetic field in the Earth's magnetosphere is mainly composed of the Earth's geomagnetic field B_0, the induced magnetic field by the magnetospheric currents, and the plasma wave magnetic fields B_w; the source of the electric field is mainly composed of the convectional electric field E_{con}, co-rotational electric field E_{rot}, and the plasma wave electric fields E_w. In general, the motion of the particles is described by the momentum equation:

$$\frac{d\mathbf{p}}{dt} = q(\mathbf{E} + \mathbf{v} \times \mathbf{B}), \tag{1.1}$$

where $\mathbf{p} = \gamma m_0 \mathbf{v}$ is the particle momentum, q is the charge of the particle, m_0 is the rest mass, $\mathbf{v}$ is the particle velocity, t is time, $\mathbf{E}$ is the electric field, $\mathbf{B}$ is the magnetic field, $\gamma = 1/\sqrt{1 - v^2/c^2}$ is the Lorentz factor, and c is light speed. The motions of the electrons can be solved using the momentum equation by test-particle simulations [e.g., *Gendrin*, 1974; *Inan et al.*, 1978; *Matsumoto and Omura*, 1981; *Bell*, 1984].

In strongly magnetized plasma, the particles perform gyration motion in the plane perpendicular to the magnetic field $\mathbf{B}$. The gyro-radius is $r_g = p \sin\alpha / qB$, and the gyro-period is $T_g = 2\pi\gamma m_0 / qB$. Here α is pitch angle of the particle, which is the angle between the particle velocity and the magnetic field. In the Earth's radiation belts, the particles also experience perturbations other than the background magnetic field, and the background magnetic field may be inhomogeneous. If the spatial scale of the changes is larger than the gyro-radius, and the temporal scale of the changes is longer than the gyro-period, the particle's magnetic moment is conserved. The first adiabatic invariant μ is:

$$\mu = \frac{P^2 \sin^2\alpha}{2m_0 B} = \frac{E_k(E_k + 2m_0c^2)}{2B(m_0c^2)} \sin^2\alpha, \tag{1.2}$$

where E_k is the particle's kinetic energy. As a consequence of the conservation of μ, when the particle moves closer to the Earth, the magnetic field B increases, and the particle gains energy.

The particles perform bounce motion along the magnetic field line due to the parallel component of the velocity. When the particles travel from the magnetic equator to higher latitudes along the field line, the magnetic field increases, and the pitch angle increases to 90° at the mirror point because μ is conserved. Therefore, the particles perform bounce motion between the two conjugate mirror points. If the outside perturbations and variations are slower than the bounce period, the second adiabatic invariant J is conserved:

$$J = \oint p_{\parallel} dl \tag{1.3}$$

where l is the distance from the equator to the particle position along the field line, and the integral is performed for a full bounce period. When the particles moves closer to the Earth where the field line is shorter, the parallel momentum increases due to the conservation of J.

In presence of the electric fields and the in-homogeneous background magnetic fields, the particles perform drift motion perpendicular to the magnetic field. The electric drift velocity is:

$$v_{\mathbf{E}\times\mathbf{B}} = \frac{\mathbf{E}\times\mathbf{B}}{B^2}. \tag{1.4}$$

The magnetic gradient drift velocity is:

$$\mathbf{v}_{gradB} = \frac{p_{\perp}^2}{2m_0 q B^3}(\mathbf{B}\times\nabla B). \tag{1.5}$$

The magnetic curvature drift velocity is:

$$\mathbf{v}_{curvB} = \frac{p_{\parallel}^2}{m_0 q B^3}(\mathbf{B}\times\nabla B). \tag{1.6}$$

Although the electric field drift is independent of the particles, the magnetic drift depends on both the charge and energy of the particles. The dawn-dusk convectional electric field causes the particles in the nightside plasma sheet to drift Earthward; the co-rotational electric field which directs towards the Earth's center leads the particles to drift eastward below the Alfven layer; the magnetic

gradient and curvature leads the electrons to drift eastward and high energy ions to drift westward in the inner magnetosphere. The low energy ions drift eastward due to the dominant electric field drift.

In association with the drift motion, the third adiabatic invariant

$$\Phi = \int \mathbf{B} \cdot d\mathbf{S} \tag{1.7}$$

is conserved when the drift orbit is closed in the magnetosphere and the timescale of other perturbations is longer than the drift period. The third adiabatic invariant is equivalently and more conveniently used as the conservation of $L*$:

$$L* = -\frac{2\pi M_p}{\Phi R_E}. \tag{1.8}$$

The three adiabatic invariants provide a simplified and physically clearer explanation about the dynamics of energetic particles in the Earth's radiation belts. Figure 1.5 is a sketch of the particle's gyration, bounce, and drift motions in the Earth's radiation belts. In absence of the other perturbations, the energetic particles stay trapped in the Earth's radiation belts. However, the various plasma waves in the magnetosphere may have timescales comparable to the periods of the particle's motions, and lead to the violation of the three adiabatic invariants.

1.3 Plasma waves in the inner magnetosphere

The Earth's magnetosphere provides a collision-less magnetized environment where the variations in the trapped energetic particle populations are mainly controlled by the interactions with magnetospheric waves. The knowledge of the presence of the plasma waves (Figure 1.6) and the wave properties are critical for understanding the non-adiabatic dynamics of the particles, simulating the evolution of particle populations, and predicting the space weather changes under the influences of solar activities.

The Ultra Low Frequency (ULF) waves (mHz) are mainly responsible for the violation of the third adiabatic invariant and lead to the particle diffusion across different L shells in the radiation belts [e.g., *Cornwall*, 1972; *Brautigam and Albert*, 2000; *Brautigam et al.*, 2005; *Ozeke et al.*, 2014]. ULF waves are excited by the perturbations on the magnetopause caused by the fluctuating solar winds. The direction of radial transport of the particles is determined by the phase space density gradient as a function of L shell. Normally the electron phase space density increases with increasing L close to the Earth, so the radial diffusion process provides the source of electrons from the outer region to the heart of the radiation belts. However, when the local heating is robust in the radiation belts, the phase space density may form a local peak at lower L shell, causing efficient outward diffusion.

The major source of the local heating of the energetic electrons is whistler-mode Chorus emissions. Chorus waves are coherent electromagnetic emissions with frequencies between $\sim 0.1 f_{ce}$ and f_{ce}, where f_{ce} is the electron gyrofrequency [e.g., *Li et al.*, 2009]. When the plasma sheet electrons are injected from the nightside and drift eastward towards the dayside, the an-isotropic distribution of the electron phase space density gradually forms, and the unstable electron distribution provides the source energy for chorus wave excitation by cyclotron resonances. Chorus waves are typically observed over a broad spatial region on the nightside-dawn-dayside sectors outside the plasmapause [e.g., *Li et al.*, 2011]. During the cyclotron and Landau resonant interactions, chorus waves affect cause loss of plasma sheet electrons at energies around tens of keV by pitch angle scattering [e.g., *Shprits et al.*, 2006; *Tao et al.*, 2011; *Thorne et al.*, 2010; *Ma et al.*, 2012], and enhancement of relativistic electrons at energies around several MeV by stochastic acceleration [e.g., *Reeves et al.*, 2013; *Thorne et al.*, 2013a; *Tu et al.*, 2014; *Fennell et al.*, 2014; *Foster et al.*, 2014; *Li et al.*, 2014b]. Chorus waves provide an efficient way to transfer energy from plasma sheet electrons to

the radiation belts.

Another possible source of electron acceleration is fast magnetosonic waves. Magnetosonic waves are electromagnetic emissions with frequencies between f_{cp} and f_{LHR} and are typically observed near the magnetic equator, where f_{cp} is the proton gyrofrequency and f_{LHR} is the lower hybrid resonance frequency. When the ions perform energy dependent drift from the nightside plasma sheet, positive gradients in ion phase space density distribution as a function of perpendicular energy forms, and provide free energy for magnetosonic wave growth. Magnetosonic waves are widely distributed near the dayside both inside and outside the plasmapause. The waves are highly oblique and can accelerate the radiation belt electrons via Landau resonance. Magnetosonic waves also interact with low energy protons and lead to the loss of protons due to pitch angle scattering. More details about the magnetosonic waves in the Earth's inner magnetosphere will be provided in the following chapters.

Plasmaspheric hiss is frequently observed at high density regions in the inner magnetosphere. Hiss emissions are incoherent electromagnetic waves with a wide frequency band mostly between 50 Hz and 1000 Hz [e.g., *Li et al.*, 2013a]. Unlike chorus or magnetosonic wave events, hiss event is generally structureless with nearly constant frequency band. Besides the local generation by the plasma sheet electron injections, hiss waves may be generated from chorus waves which propagate from the lower density plasmatrough to the higher density plasmasphere [e.g., *Bortnik et al.*, 2008, 2009; *Chen et al.*, 2014]. Hiss waves may propagate along the field lines and be reflected at high latitudes, presenting propagation properties and wide ranges of distribution. During the resonant interactions, hiss waves typically cause the loss of energetic electrons with energies from tens of keV to several MeV in the plasmasphere, causing the decay of radiation belt particle fluxes [e.g., *Ni et al.*, 2013, 2014].

Electro-Magnetic Ion Cyclotron (EMIC) waves provide an efficient loss mech-

anism for highly relativistic electrons [e.g., *Albert*, 2003; *Kersten et al.*, 2014]. EMIC waves are discrete electromagnetic emissions at different frequency bands separated by gyro-frequencies of different ion species. The an-isotropic distributions of the ion phase space densities formed during the drift motion provide the source energy of EMIC wave excitation [e.g., *Chen et al.*, 2009a,b; *Usanova et al.*, 2010]. EMIC waves are generally observed with amplitudes of $\sim$ 1 nT in high density regions near the plasmapause boundary or inside the drainage plume. *Meredith et al.* [2014] have provided the global distribution of EMIC waves under different geomagnetic conditions. EMIC waves cause the pitch angle scattering loss of relativistic electrons with energies higher than 1 MeV due to cyclotron resonance [e.g., *Li et al.*, 2007; *Usanova et al.*, 2014], and also cause the precipitating loss of ring current protons. During the scattering by EMIC waves, the relativistic electrons form a 'top hat' pitch angle distribution which is confirmed by satellite observations [*Usanova et al.*, 2014].

1.4 Magnetosonic waves and particles

As a highly oblique electromagnetic wave mode occasionally observed in the vicinity of the Earth's magnetic equator, magnetosonic waves have been an interesting topic soon after its first discovery in the 1960s. Both theoretical and observational researches have been performed to investigate the potential roles of magnetosonic waves in the Earth's radiation belts.

The ring current ions can provide the energy source for the growth of magnetosonic waves. When the ions perform energy dependent drift [e.g., *Lyons and Williams*, 1984; *Jordanova et al.*, 2010], the ion ring distribution naturally forms near the dayside as shown in Figure 1.7. The ion phase space density (f) distribution has a peak value around the energy of tens of keV and a dip value around the energy of several keV (Figure 1.7). The positive slope between the dip and peak

energies is not stable, and could excite magnetosonic waves if the Alfven energy is close to this range [*Chen et al.*, 2010]. The major part of convective wave growth rate can be approximated as:

$$K_i \approx \int_0^\infty dv_\perp W_\perp \frac{\partial f}{\partial v_\perp}|_{v_\parallel=0}, \tag{1.9}$$

where $v_\perp$ and $v_\parallel$ are perpendicular and parallel velocities respectively, and $W_\perp$ is the weighting function. The magnetosonic waves will significantly grow if $W_\perp$ reaches maximum value at a perpendicular velocity close to the positive slopes of $\frac{\partial f}{\partial v_\perp}$. As a consequence, the magnetosonic waves are typically excited in a wide region near the dayside both inside and outside the plasmapause, and higher (lower) frequency waves are excited where the total plasma density is lower (higher) [*Chen et al.*, 2010].

Intense magnetosonic waves have an impact on the radiation belt electron dynamics. As presented in Figure 1.8, the magnetosonic waves are mainly confined within $2 \sim 3$ degrees near the magnetic equator. When the energetic electrons stream from one side of the hemisphere to another (Figure 1.8c), they encounter the waves and are scattered in pitch angle and energy. The perturbations in pitch angle and energy are evaluated in diffusion coefficients, and the impacts on the electron populations can be simulated by numerically solving the diffusion equations. Landau resonance is mainly responsible for the interactions between energetic electrons and magnetosonic waves [*Horne et al.*, 2007]. Landau resonance is caused by the parallel electric field in the frame of moving electrons, which leads to constant acceleration of electrons in the parallel direction. The investigation of an intense magnetosonic wave event with amplitude greater than 200 pT shows that the magnetosonic wave can accelerate electrons in a timescale of 1 day [*Horne et al.*, 2007]. In addition, because of the equatorial confinement of the waves, the electrons may experience only a fraction of the wave period and be scattered by the perpendicular electric field. This effect is explained as transit-time scattering by *Bortnik and Thorne* [2010], simulated by *Li et al.* [2014a], and

further formularized by *Bortnik et al.* [2015].

1.5 Particle diffusion in the radiation belts

The Earth's outer electron radiation belt is highly variable due to various source and loss processes [e.g., *Reeves et al.*, 2003; *Thorne*, 2010; *Baker et al.*, 2013; *Turner et al.*, 2014]. The dynamics of energetic electrons in the Earth's outer radiation belt are strongly affected by wave-particle interactions, and the evolution of the electron population can be reasonably described using quasi-linear theory [*Kennel and Engelmann*, 1966; *Lyons*, 1974a,b]. Electrons resonant with Ultra Low Frequency (ULF) waves violate the third adiabatic invariant and undergo radial diffusion, causing radial electron transport [e.g., *Cornwall*, 1972; *Shprits et al.*, 2008a; *Ozeke et al.*, 2014]. Electrons resonant with higher frequency electromagnetic waves violate the first and second adiabatic invariants and undergo pitch angle and energy diffusion, causing precipitation loss into the atmosphere and energy exchange with the waves [e.g., *Albert*, 2004, 2007, 2009; *Glauert and Horne*, 2005; *Horne and Thorne*, 1998; *Li et al.*, 2007; *Shprits et al.*, 2008b; *Summers*, 2005; *Xiao et al.*, 2009, 2010].

The evolution of the radiation belt particle phase space density due to the radial, pitch angle, and energy diffusion processes can be described by the modified Fokker-Planck equation [e.g., *Schulz and Lanzerotti*, 1974]:

$$\begin{aligned}
\frac{\partial f}{\partial t} &= L*^2 \frac{\partial}{\partial L*}|_{\mu,J}\left(\frac{D_{L*L*}}{L*^2}\frac{\partial f}{\partial L*}|_{\mu,J}\right) \\
&+ \frac{1}{S(\alpha_{\rm eq})\sin\alpha_{\rm eq}\cos\alpha_{\rm eq}}\frac{\partial}{\partial \alpha_{\rm eq}}|_{L*,p}\left(S(\alpha_{\rm eq})\sin\alpha_{\rm eq}\cos\alpha_{\rm eq}\langle D_{\alpha_{\rm eq}\alpha_{\rm eq}}\rangle\frac{\partial f}{\partial \alpha_{\rm eq}}|_{L*,p}\right) \\
&+ \frac{1}{S(\alpha_{\rm eq})\sin\alpha_{\rm eq}\cos\alpha_{\rm eq}}\frac{\partial}{\partial \alpha_{\rm eq}}|_{L*,p}\left(S(\alpha_{\rm eq})\sin\alpha_{\rm eq}\cos\alpha_{\rm eq}\langle D_{\alpha_{\rm eq}p}\rangle\frac{\partial f}{\partial p}|_{L*,\alpha}\right) \\
&+ \frac{1}{p^2}\frac{\partial}{\partial p}|_{L*,\alpha}\left(p^2\langle D_{p\alpha_{\rm eq}}\rangle\frac{\partial f}{\partial \alpha_{\rm eq}}|_{L*,p}\right) \\
&+ \frac{1}{p^2}\frac{\partial}{\partial p}|_{L*,\alpha}\left(p^2\langle D_{pp}\rangle\frac{\partial f}{\partial p}|_{L*,\alpha}\right), \qquad (1.10)
\end{aligned}$$

where f is the electron phase space density and related with differential energy flux as $f = j/p^2$, $\alpha_{\rm eq}$ is equatorial pitch angle, t is time, p is particle momentum, D_{L*L*} is radial diffusion coefficient, and $\langle D_{\alpha_{\rm eq}\alpha_{\rm eq}}\rangle$, $\langle D_{pp}\rangle$ and $\langle D_{\alpha_{\rm eq}p}\rangle = \langle D_{p\alpha_{\rm eq}}\rangle$ denote bounce-averaged diffusion coefficients in pitch angle, energy, and mixed terms respectively. The drift and bounce frequencies are generally evaluated in a dipole magnetic field [e.g., *Hamlin et al.*, 1961; *Walt*, 1994]. $S(\alpha_{\rm eq})$ is a function related to the bounce period and in a dipole field it can be approximated by $S(\alpha_{\rm eq}) = 1.38 - 0.32\sin\alpha_{\rm eq} - 0.32\sqrt{\sin\alpha_{\rm eq}}$ [*Lenchek et al.*, 1961]. The diffusion equations can be numerically solved using different particle differential equation schemes [e.g., *Albert and Young*, 2005; *Chang and Cooper*, 1970; *Ma and Summers*, 2001; *Su et al.*, 2009; *Subbotin and Shprits*, 2009; *Subbotin et al.*, 2010; *Tao et al.*, 2008; *Tu et al.*, 2013, 2014; *Ma et al.*, 2015].

The Doppler-shifted resonant condition for resonant interactions between electrons and plasma waves is

$$\omega - k_{\|}v_{\|} = n\Omega_{\rm e}/\gamma, \tag{1.11}$$

where ω is the wave frequency, $k_{\|}$ is the wave number parallel to the ambient magnetic field, $v_{\|}$ is the parallel velocity, n is the resonant harmonic order, $\Omega_{\rm e}$ is the electron gyro-frequency, and γ is the relativistic factor.

Figure 1.9 presents one example of radiation belt modeling. During quiet periods, gradual diffusion and slow decay of energetic electrons is a common feature observed by satellites in the radiation belts [*Baker et al.*, 2013, 2014]. The time series analysis of energetic electrons (Figure 1.9 a-d) clearly shows that the electron fluxes at multiple energy channels of Van Allen Probes diffused inward by 0.5 R_E and decayed by one order from March 06 to March 17 in 2013. By incorporating the roles of radial diffusion and scattering by plasmaspheric hiss and EMIC waves, the three dimensional simulation of radiation belt electrons (Figure 1.9 f-i) presents the diffusive profiles during 10 days, in good agreement with the observations. In absence of scattering by EMIC waves, the electrons are energized

when transported from higher $L*$ due to the lack of loss processes. Here $L*$ is obtained from the TS05 magnetic field model [*Tsyganenko and Sitnov*, 2005]. The 3D radiation belt model is a useful technique to explain the dynamics of energetic particles.

When the local wave-particle interaction processes are dominant in the heart of radiation belts, it's useful to perform a local simulation by numerically solving the 2D Fokker-Planck equation:

$$\begin{aligned}\frac{\partial f}{\partial t} &= \frac{1}{S(\alpha_{\rm eq})\sin\alpha_{\rm eq}\cos\alpha_{\rm eq}}\frac{\partial}{\partial\alpha_{\rm eq}}(S(\alpha_{\rm eq})\sin\alpha_{\rm eq}\cos\alpha_{\rm eq}\langle D_{\alpha_{\rm eq}\alpha_{\rm eq}}\rangle\frac{\partial f}{\partial\alpha_{\rm eq}}) \\ &+ \frac{1}{S(\alpha_{\rm eq})\sin\alpha_{\rm eq}\cos\alpha_{\rm eq}}\frac{\partial}{\partial\alpha_{\rm eq}}(S(\alpha_{\rm eq})\sin\alpha_{\rm eq}\cos\alpha_{\rm eq}\langle D_{\alpha_{\rm eq}p}\rangle\frac{\partial f}{\partial p}) \\ &+ \frac{1}{p^2}\frac{\partial}{\partial p}(p^2\langle D_{p\alpha_{\rm eq}}\rangle\frac{\partial f}{\partial\alpha_{\rm eq}}) \\ &+ \frac{1}{p^2}\frac{\partial}{\partial p}(p^2\langle D_{pp}\rangle\frac{\partial f}{\partial p}),\end{aligned} \tag{1.12}$$

The 2D Fokker-Planck equation can be solved efficiently and accurately using the Alternative Directional Implicit (ADI) method. The various diffusion coefficients are calculated based on the wave frequency spectrum, wave normal distribution, wave latitudinal distribution, and wave amplitude [e.g., *Ni et al.*, 2008, 2011; *Shprits and Ni*, 2009]. The local acceleration of highly energetic electrons from 100 keV to several MeV due to the interactions with chorus waves [*Thorne et al.*, 2013a; *Li et al.*, 2014b] and the loss of energetic electrons in the radiation belts due to hiss waves [*Thorne et al.*, 2013b; *Ni et al.*, 2013, 2014] have been successfully simulated using the 2D radiation belt model.

1.6 Summary

The plasma waves and energetic particle populations have significant roles in the inner magnetosphere dynamics and space weather variations. To explain various related phenomena in the inner magnetosphere and apply them to the modern

space technique, it's important to understand the wave distribution under different conditions, the source of important plasma waves, the wave trajectory in the magnetosphere, and the effects on the energetic particle populations due to scattering by the plasma waves. The recent scientific spacecraft provide ideal observations of the space environment, and the theoretical and modeling efforts bring the physical knowledge to a new level.

This thesis focus on the equatorial magnetosonic waves in the inner magnetosphere. The format of this thesis is as follows: the basic properties of equatorial magnetosonic waves is discussed in Chapter 2; the global distribution of magnetosonic waves observed by THEMIS is discussed in Chapter 3; Chapter 4 presents the excitation of mangetosonic waves in typical plasma conditions; Chapter 5 presents the equatorial propagation properties of magnetosonic waves in the plasmasphere; the potential scattering effects due to typical global magnetosonic waves is discussed in Chapter 6; Chapter 7 is the summary of the thesis.

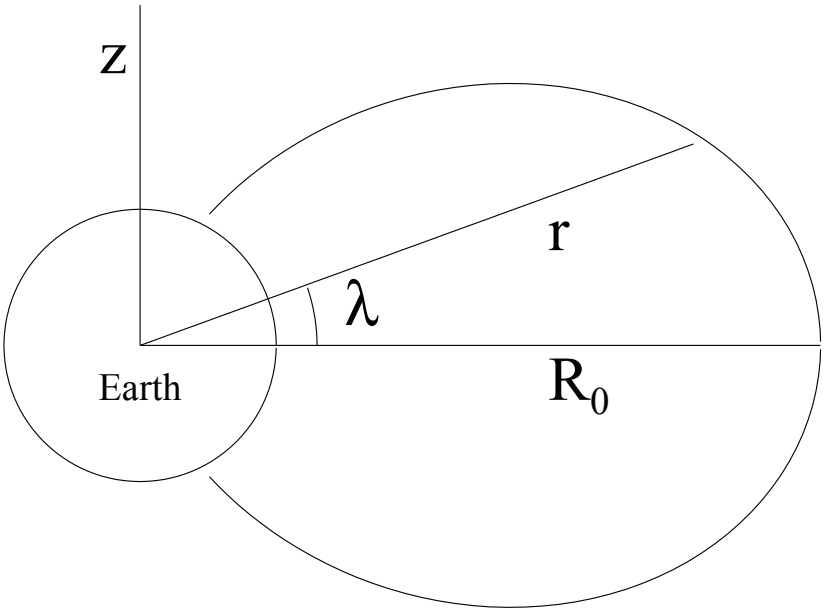

Figure 1.1: The Earth's dipole magnetic field. R_0 is the equatorial radial distance, λ is the magnetic latitude, r is the distance from the field line to the center of the Earth.

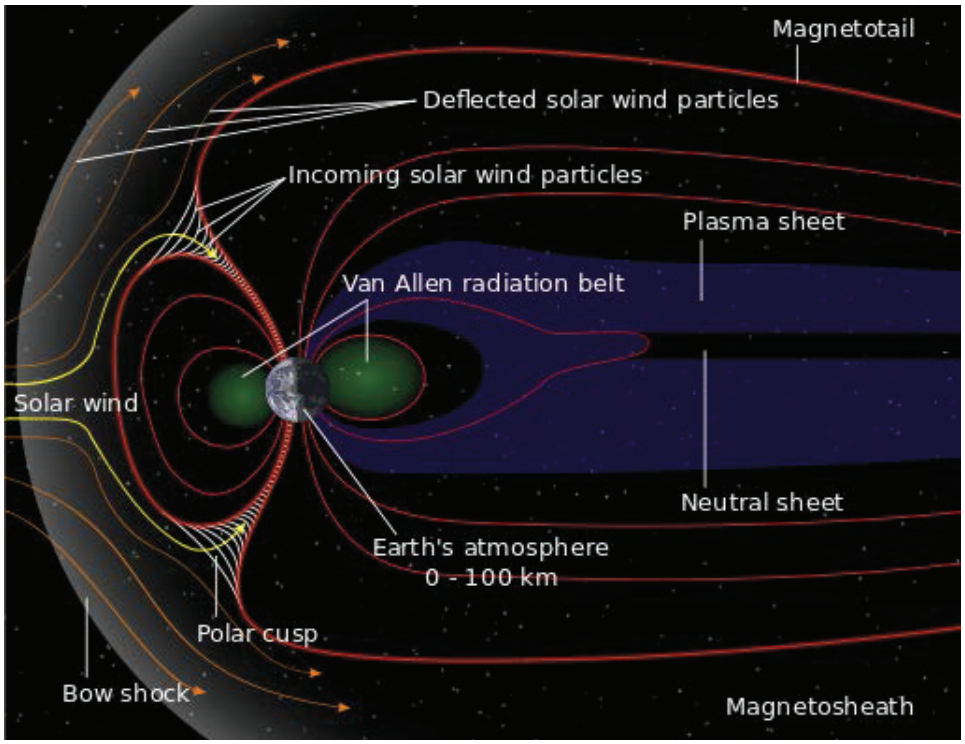

Figure 1.2: The structure of the Earth's magnetosphere. [Figure from Wikipedia (http://en.wikipedia.org/wiki/Magnetosphere). Original bitmap from NASA. SVG rendering by Aaron Kaase.]

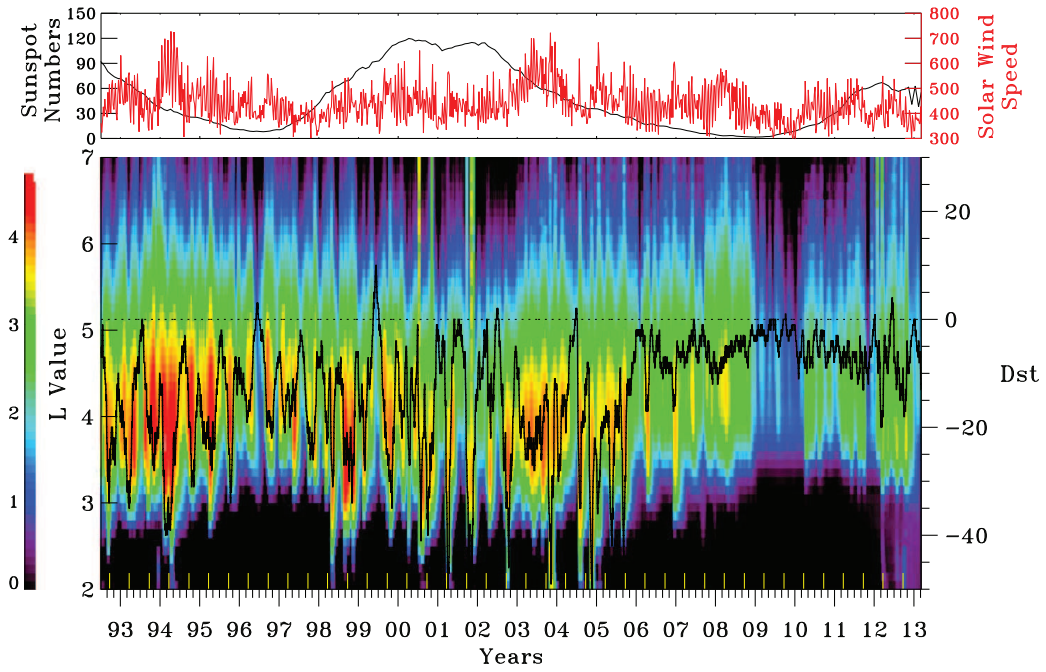

Figure 1.3: The twenty years variation of solar activities and radiation belt particle fluxes. (top) Yearly averaged sunspot number (black) and weekly averaged solar wind speed (red). (bottom) Monthly averaged electron flux at an energy of $\sim 2MeV$ as a function of L shell. The black line in the bottom panel is the monthly averaged Dst index. [*Li et al.*, 2013b]

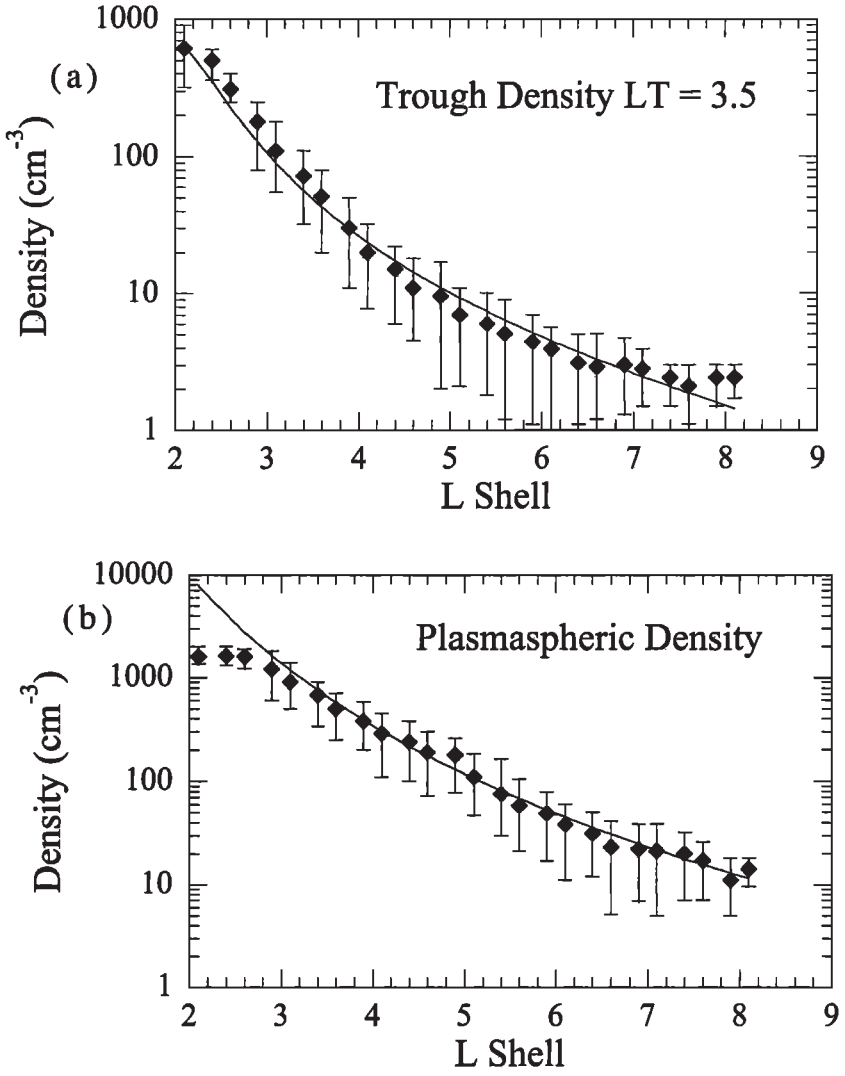

Figure 1.4: The best fitting of the plasma density as a function of L shell based on the averaged plasma density of CRRES measurements. (a) Density at plasmatrough and at the local time of 3.5 UT; (b) density in the plasmasphere. The solid lines are fitting results, and the diamonds are averaged data at each L shell bins with standard variations. [*Sheeley et al.*, 2001]

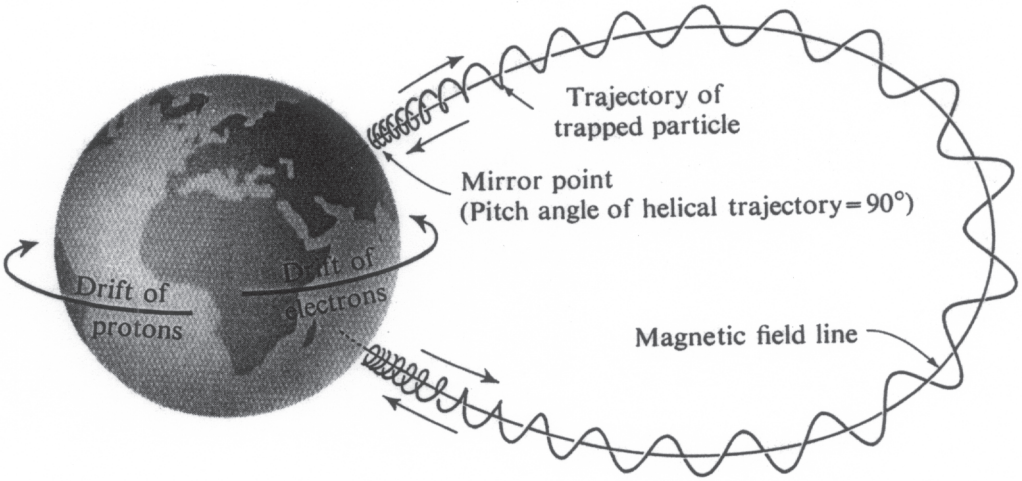

Figure 1.5: An illustration about the particle's gyration, bounce, and drift behaviors in the Earth's radiation belts. [*Mars*, 2002]

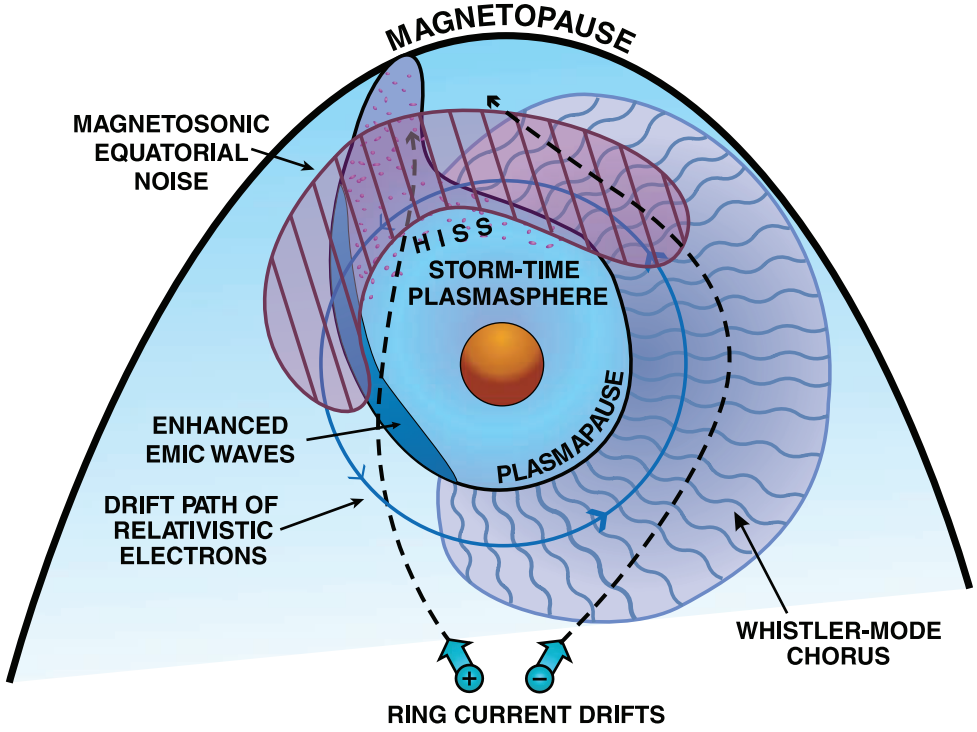

Figure 1.6: Spatial distribution of important waves in the inner magnetosphere, in relation to the plasmasphere and the drift-paths of ring current (10-100 keV) electrons and ions and relativistic ($\geq$ 0.3 MeV) electrons. [*Thorne*, 2010]

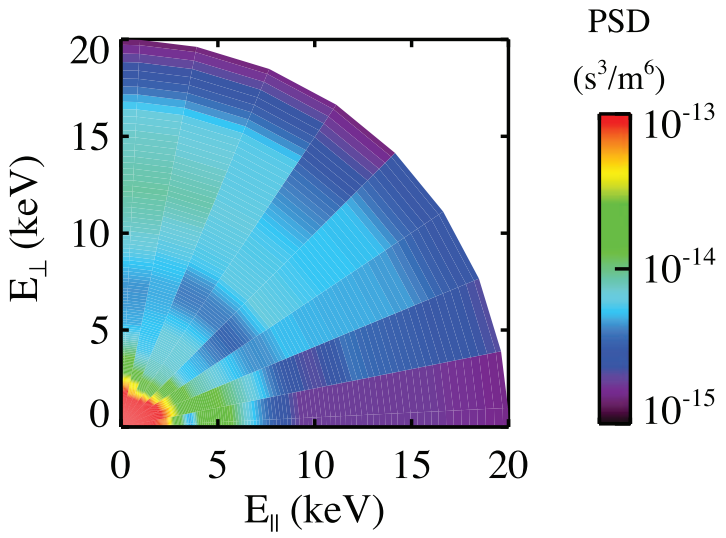

Figure 1.7: The ion ring distribution near the dayside magnetosphere observed by THEMIS A around 03:11 UT on November 24, 2010. Phase space density is plotted as a function of parallel and perpendicular energies. [*Ma et al.*, 2013]

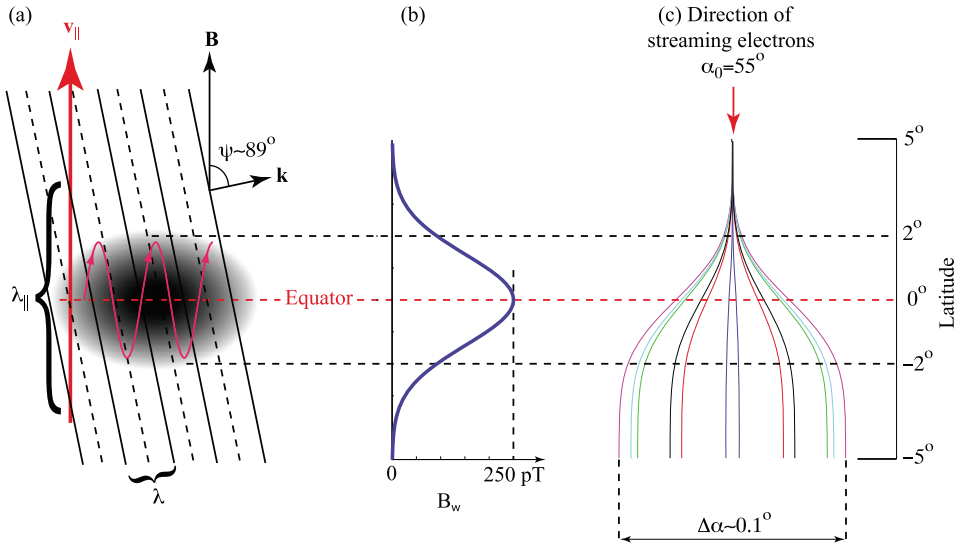

Figure 1.8: Schematic of magnetosonic wave geometry showing (a) obliquity, ray trajectory 'snaking' about the equator, equatorial confinement, and resultant extent of $k_{\|}$, (b) distribution of magnetic amplitude as a function of latitude, and (c) pitch angle scattering of $E_k = 300$ keV, $a_0 = 55°$ electrons due to magnetosonic waves. [*Bortnik and Thorne*, 2010]

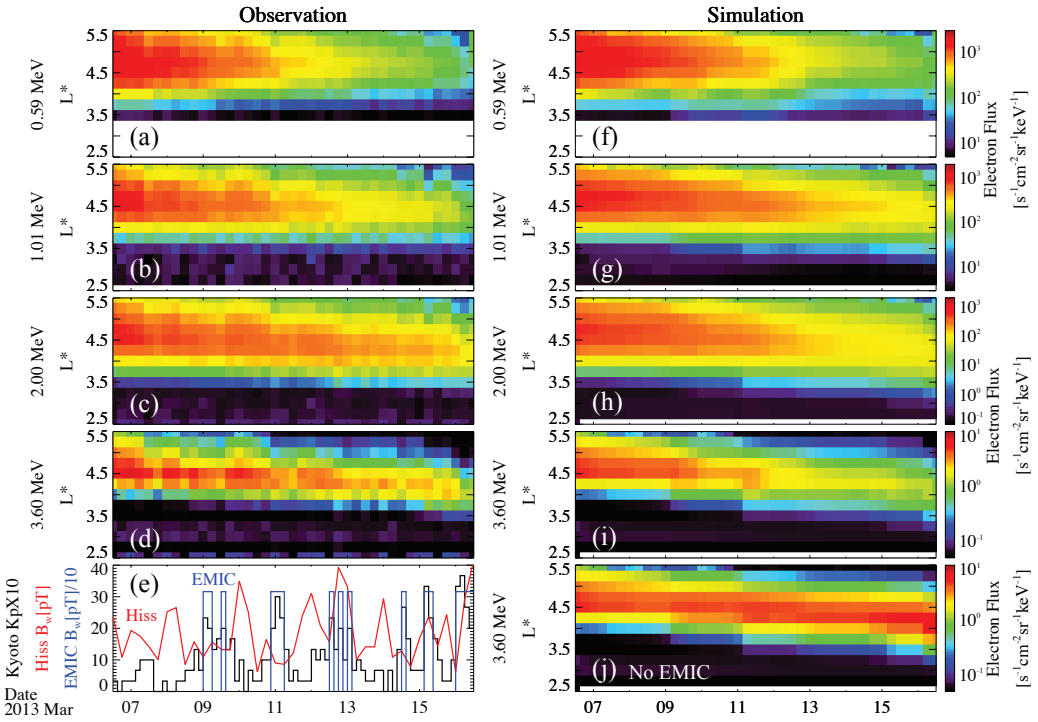

Figure 1.9: The comparison between the observation and simulation of equatorially mirroring electron fluxes from 12:00 UT on 6 March to 12:00 UT on 16 March 2013. The Van Allen Probe observation of electron differential flux as a function of $L*$ for an energy of (a) 0.59 MeV, (b) 1.01 MeV, (c) 2.00 MeV, (d) 3.60 MeV, and (e) the Kyoto Kp index multiplied by 10 (black line), the hiss wave amplitude averaged over $L = 4$ to 5 (red line), and the EMIC wave amplitude with an intensity of $B_w^2 = 0.1\text{nT}^2$ when $Kp \geq 2$ (blue line). Full simulation results of electron differential flux as a function of $L*$ for an energy of (f) 0.59 MeV, (g) 1.01 MeV, (h) 2.00 MeV, (i) 3.60 MeV, and simulation of the electron differential flux evolution without EMIC wave scattering for an energy of (j) 3.60 MeV. [*Ma et al.*, 2015]

CHAPTER 2

General properties of magnetosonic waves

Fast magnetosonic waves are unique whistler-mode emissions with highly oblique wave normal angles and confined narrowly near the Earth's magnetic equator, and have distinct characters from other wave modes in the magnetosphere (e.g., whistler-mode chorus, hiss, and EMIC waves). This chapter will focus on the dispersion relation of magnetosonic waves and their properties in the inner magnetosphere.

2.1 Observed properties of magnetosonic wave events in the Earth's magnetosphere

The wide existence and high obliquity of magnetosonic waves have been confirmed by the real-time satellite observations since the late 1960s. OGO 3 satellite observed Extremely Low Frequency (ELF) signals when it was close to the Earth's magnetic equator at $L \sim 4.5$ on July 5, 1966 [*Russell et al.*, 1970]. Plasmaspheric hiss waves were identified at higher frequencies (300 - 600 Hz) due to the magnetic perturbations at both parallel and perpendicular directions; magnetosonic waves (also called 'equatorial noises') were identified at lower frequencies ($\leq$ 100 Hz) due to the much stronger magnetic perturbations at parallel direction than perpendicular direction and therefore the wave normal angles are large. The observation by OGO 3 also showed that the magnetosonic wave events were mainly confined near the magnetic equator.

The observation of plasma waves in the Earth's magnetosphere has been improved since the launch of recent spacecraft. Cluster satellites provide information about the magnetosonic waves when they cross the magnetic equator. Figure 2.1 is one example of magnetosonic wave event observed by Cluster 4 on 17 February 2002. Magnetosonic waves are identified by both magnetic (Figure 2.1a) and electric (Figure 2.1b) wave power spectra in the frequency band of 20 - 100 Hz at around 21:55 UT. Magnetosonic waves were detected within $\sim 5^{\circ}$ near the equator, and Cluster satellites with high latitude obits can provide ~ 20 min continuous observation of the event around their perigees. The wave polarization properties were obtained using the singular value decomposition of the magnetic spectral matrix. Figure 2.1c shows the ellipticity of the waves which varies from 0 (linear polarization) to 1 (circular polarization). The magnetosonic wave has low ellipticity and therefore are nearly linearly polarized. Figure 2.1d shows the planarity of the waves. The planarity magnetosonic wave is high, which means that the wave is nearly a single 2D plane wave. The wave polarization information can be used to identify magnetosonic waves from other emissions occurring in the similar frequency band and locations (e.g., plasmaspheric hiss).

Magnetosonic waves are observed between the proton gyrofrequency and the lower hybrid resonance frequency. The detailed wave frequency spectrum analysis has shown that the wave frequency spectrum is strongly modulated by the harmonics of proton gyrofrequency. Figure 2.2b presents one example of magnetic power spectrum as a function of wave frequency observed by Cluster satellites. The magnetosonic wave power clearly presents harmonics structures. At higher frequencies between 130 Hz and 190 Hz, the spacing of peak frequencies is ~ 6.5 Hz, which may be the proton gyrofrequency at the source of the waves. Magnetosonic waves are mainly excited at multiple harmonics of the proton gyrofrequency, and propagate in the equatorial plane from the source region.

2.2 The cold plasma dispersion relation

The dynamics of electric ($\mathbf{E}$) and magnetic ($\mathbf{B}$) fields in general are described by Maxwell's equations, and the motion of particle is governed by momentum equation. We will discuss small amplitude waves and linearize the relations. The following assumptions are made in cold plasma theory derivations: 1. background magnetic field $\mathbf{B}_0$ is uniform and $\mathbf{B} = \mathbf{B}_0 + \mathbf{B}_1$; 2. total background plasma density n_0 is homogeneous and $N = n_0 + n_1$; 3. there is no static electric field and $\mathbf{E} = \mathbf{E}_1$; 4. particle temperature is zero and $\mathbf{u} = \mathbf{u}_1$. Here u is particle velocity, subscript '0' represents the zeroth order quantities, and subscript '1' represents the first order quantities caused by wave perturbations.

The linearized Maxwell's equations are:

$$\nabla \cdot \mathbf{E}_1 = \frac{\rho}{\epsilon_0} \tag{2.1}$$

$$\nabla \times \mathbf{E}_1 = -\frac{\partial \mathbf{B}_1}{\partial t} \tag{2.2}$$

$$\nabla \cdot \mathbf{B}_1 = 0 \tag{2.3}$$

$$\nabla \times \mathbf{B}_1 = \mu_0 \mathbf{J} + \frac{1}{c^2}\frac{\partial \mathbf{E}_1}{\partial t}, \tag{2.4}$$

where t is time, c is light speed, m is the mass, ρ is electric charge density, $\mathbf{J}$ is electric current density, $\epsilon_0 = 8.85 \times 10^{-12} F/m$ is vacuum permittivity, and $\mu_0 = 1.26 \times 10^{-6} H/m$ is magnetic permeability.

The linearized continuity equation is:

$$\frac{\partial n_1}{\partial t} + \nabla \cdot (n_0 \mathbf{u}_1) = 0 \tag{2.5}$$

The linearized momentum equation is:

$$\frac{\partial \mathbf{u}_1}{\partial t} = \frac{e}{m}(\mathbf{E}_1 + \mathbf{u}_1 \times \mathbf{B}_0) \tag{2.6}$$

Here we consider two species plasma with protons and electrons. The gyrofrequency is $\Omega = \frac{eB_0}{m}$. The charge density and current density are the sum of each

species:

$$q = \sum en_1 \tag{2.7}$$

$$\mathbf{J} = \sum en_0\mathbf{u}_1 \tag{2.8}$$

Using equations (2.2) and (2.4) we can eliminate $\mathbf{B}_1$ and obtain:

$$\nabla \times (\nabla \times \mathbf{E}_1) = -\frac{1}{c^2}\frac{\partial^2 \mathbf{E}_1}{\partial t^2} - \mu_0 \frac{\partial \mathbf{J}}{\partial t} \tag{2.9}$$

We will use Fourier transform for the perturbations and assume that all varying quantities are proportional to $e^{i(\omega t - \mathbf{k}\cdot\mathbf{x})}$. The wave refractive index is defined as $\mathbf{n} = \dfrac{\mathbf{k}c}{\omega}$, and the conductivity tensor σ is defined as:

$$\mathbf{J} = \sigma \cdot \mathbf{E} \tag{2.10}$$

Equation (2.9) follows that:

$$\mathbf{n} \times (\mathbf{n} \times \mathbf{E}_1) = -\mathbf{E}_1 + \frac{i}{\epsilon_0 \omega}\sigma \cdot \mathbf{E}_1 \tag{2.11}$$

By defining the dielectric tensor $\mathbf{K} = 1 - \dfrac{i}{\epsilon_0\omega}\sigma$, the wave dispersion relation is:

$$\mathbf{n} \times (\mathbf{n} \times \mathbf{E}_1) + \mathbf{K} \cdot \mathbf{E}_1 = 0 \tag{2.12}$$

The particle momentum equation (2.6) is required to solve for σ and $\mathbf{K}$. The momentum equation in (x, y, z) coordinate is:

$$i\omega u_x - \Omega u_y = eE_x/m \tag{2.13}$$

$$i\omega u_y + \Omega u_x = eE_y/m \tag{2.14}$$

$$i\omega u_z = eE_z/m \tag{2.15}$$

The momentum equation can be simplified in a rotating coordinate (+, -, z):

$$I_+ = I_x + iI_y \tag{2.16}$$

$$I_- = I_x - iI_y, \tag{2.17}$$

where **I** represents the quantities **u**, **E**, or **J**. The solution is:

$$u_+ = -i\frac{eE_+}{m(\omega+\Omega)} \tag{2.18}$$

$$u_- = -i\frac{eE_-}{m(\omega-\Omega)} \tag{2.19}$$

$$u_z = -i\frac{eE_z}{m\omega} \tag{2.20}$$

Combining equations (2.8), (2.10), and (2.18) - (2.20), the conductivity tensor is solved as:

$$\sigma = -i\epsilon_0 \begin{pmatrix} \sum \frac{\omega_{p\alpha}^2}{\omega+\Omega_\alpha} & 0 & 0 \\ 0 & \sum \frac{\omega_{p\alpha}^2}{\omega-\Omega_\alpha} & 0 \\ 0 & 0 & \sum \frac{\omega_{p\alpha}^2}{\omega} \end{pmatrix}, \tag{2.21}$$

where $\omega_{p\alpha} = \sqrt{\frac{N_\alpha e^2}{m\epsilon_0}}$ is the plasma oscillation frequency. Equation (2.21) follows that:

$$\mathbf{K} = \begin{pmatrix} R & 0 & 0 \\ 0 & L & 0 \\ 0 & 0 & P \end{pmatrix}, \tag{2.22}$$

where R, L, and P are Stix parameters:

$$R = 1 - \frac{\omega_{pe}^2}{\omega(\omega+\Omega_e)} - \frac{\omega_{pi}^2}{\omega(\omega+\Omega_i)} \tag{2.23}$$

$$L = 1 - \frac{\omega_{pe}^2}{\omega(\omega-\Omega_e)} - \frac{\omega_{pi}^2}{\omega(\omega-\Omega_i)} \tag{2.24}$$

$$P = 1 - \frac{\omega_{pe}^2 + \omega_{pi}^2}{\omega^2} \tag{2.25}$$

Here the gyrofrequencies contain the sign of particles. To transform rotating coordinate (+, -, z) into (x, y, z), equations (2.16) - (2.17) follows that:

$$I_x = \frac{I_+ + I_-}{2} \tag{2.26}$$

$$I_y = \frac{I_+ - I_-}{2i} \tag{2.27}$$

We can obtain the dielectric tensor:

$$\mathbf{K} = \begin{pmatrix} S & iD & 0 \\ -iD & S & 0 \\ 0 & 0 & P \end{pmatrix}, \tag{2.28}$$

where the Stix parameters $S = \frac{R+L}{2}$ and $D = \frac{R-L}{2}$.

We can assume that the wave vector lies in x-z plane, and define the wave normal angle ψ as the angle between $\mathbf{B}_0$ and $\mathbf{k}$, so that $k_x = k\sin\psi$, $k_y = 0$, $k_z = k\cos\psi$. By substituting equation (2.28) into (2.12) we obtain the following wave dispersion relation which is consistent with the results in [*Krall and Trivelpiece*, 1973; *Boyd and Sanderson*, 2003]:

$$\begin{pmatrix} S - n^2\cos^2\psi & iD & n^2\cos\psi\sin\psi \\ -iD & S - n^2 & 0 \\ n^2\cos\psi\sin\psi & 0 & P - n^2\sin^2\psi \end{pmatrix} \begin{pmatrix} E_x \\ E_y \\ E_z \end{pmatrix} = 0 \tag{2.29}$$

By requiring the determinant of the matrix to be zero, this lead to:

$$An^4 - Bn^2 + C = 0, \tag{2.30}$$

where the Stix parameters A, B, and C are:

$$A = S\sin^2\psi + P\cos^2\psi \tag{2.31}$$

$$B = RL\sin^2\psi + PS(1 + \cos^2\psi) \tag{2.32}$$

$$C = PRL \tag{2.33}$$

Equation (2.30) has two solutions

$$n^2 = \frac{B \pm F}{2A}, \tag{2.34}$$

where the Stix parameter F is:

$$F = \sqrt{(RL - PS)^2\sin^4\psi + 4P^2D^2\cos^2\psi} \tag{2.35}$$

2.3 Dispersion and polarization of magnetosonic waves

With the knowledge of wave total magnetic field amplitude, the different electric and magnetic field components can be obtained from their ratios. The wave polarization information is obtained from the Faraday's law of induction (2.2) and wave dispersion relation (2.29):

$$\frac{E_x}{B_y} = \frac{c(P - n^2 \sin^2 \psi)}{Pn \cos \psi} \tag{2.36}$$

$$\frac{E_y}{B_y} = \frac{cD(P - n^2 \sin^2 \psi)}{Pn \cos \psi (S - n^2)} \tag{2.37}$$

$$\frac{E_z}{B_y} = \frac{-cn \sin \psi}{P} \tag{2.38}$$

$$\frac{B_x}{B_y} = \frac{-D(P - n^2 \sin^2 \psi)}{P(S - n^2)} \tag{2.39}$$

$$\frac{B_z}{B_y} = \frac{D \sin \psi (P - n^2 \sin^2 \psi)}{P \cos \psi (S - n^2)} \tag{2.40}$$

Magnetosonic waves are highly oblique electromagnetic emissions between the proton gyfrofrequency Ω_{cp} and the lower hybrid resonance frequency ω_{LHR}. The wave vector is almost perpendicular to the background magnetic field $\mathbf{B}_0$, i.e., $k_x \gg k_z$, and $k_y = 0$. The wave dispersion relation for highly oblique waves ($\psi \sim 90^\circ$) is simplified as:

$$n^2 = \frac{RL}{S} \tag{2.41}$$

For whistler-mode waves with wave frequency $\Omega_{cp} \ll \omega \ll \Omega_{ce}$ and assuming $\Omega_{ce} \ll \Omega_{pe}$ in the inner magnetosphere, we can confirm that $R > 0$ and $L < 0$, and equation (2.41) implies that the wave only propagates where $S < 0$. Since $S = \frac{R + L}{2}$, $S = 0$ leads to the lower hybrid resonance frequency:

$$\omega_{LHR} = \sqrt{\Omega_{ce} \Omega_{cp}} \tag{2.42}$$

S changes sign from negative to positive when wave frequency increases from below ω_{LHR} to above ω_{LHR}, therefore the waves cannot propagate at frequencies larger than ω_{LHR}.

Fast magnetosonic emissions are compressional mode waves. It is clear from the wave polarization that for highly oblique waves $B_z \gg B_x$ and $B_z \gg B_y$, so that the wave mangetic field is almost aligned with the background magnetic field $\mathbf{B}_0$.

The polarization of electric field implies that the perpendicular electric field component is dominant, i.e., $E_z \ll E_x$ and $E_z \ll E_y$. Furthermore, the ratio between E_x and E_y can be simplified as:

$$\frac{E_x}{E_y} = \frac{R - L}{R + L} \tag{2.43}$$

Because $R > 0$ and $L < 0$, E_x is generally much larger than E_y. Therefore, wave electric field is nearly parallel to the wave vector $\mathbf{k}$, and the electric field perturbation is mostly longitudinal.

Figure 2.3 and 2.4 show Stix parameters, dispersion relations, and wave electric and magnetic components under typical plasma conditions at $L = 4.5$ inside and outside the plasmapause, respectively. Full plasma dispersion relation is used for the calculations. All variables are plotted as a function of normalized wave frequency $\frac{f}{f_{cp}}$. The total wave magnetic field amplitude is assumed to be 100 pT at different frequencies. The wave normal angle is assumed to be 89.5°. The background magnetic field is assumed to be a dipole field. Sheeley's total plasma density model is used to estimate n_0 inside and outside the plasmapause. As the wave frequency increases, P decreases significantly, both R and L approach zero, and S increases and changes sign at lower hybrid resonance frequency ($\sim 45 f_{cp}$). The refractive index n increases mono-chromatically and approaches infinity at lower hybrid resonance frequency. For magnetosonic waves, E_x and B_z are dominant components. At lower frequencies, $|B_z| \gg |B_y|$ and $|E_x| \gtrsim |E_y|$; at higher frequen-

cies, $|B_z| \gtrsim |B_y|$ and $|E_x| \gg |E_y|$. The value of refractive index is much higher inside the plasmapause than outside due to the difference in total plasma densities. The ratio of plasma frequency to electron gyrofrequency is $f_{pe}/f_{ce} = 13.2$ inside the plasmapause, and $f_{pe}/f_{ce} = 4.7$ outside the plasmapause.

2.4 Properties of magnetosonic waves in the magnetosphere

Magnetosonic waves in the magnetosphere have some unique properties due to their highly oblique wave normal angle and wave polarization characters. Those properties have significant effects in the wave excitation by ion distributions, propagation in the plasmasphere, and interaction with radiation belt electrons.

Magnetosonic waves are mainly excited at multiple harmonics of proton gyrofrequencies. The wave growth rate calculation can be simplified for highly oblique magnetosonic waves excited at $\omega = m\Omega_{cp}$, where m is a whole number. Because $k_\parallel$ is small, the resonance condition between waves and protons

$$\omega - k_\parallel v_\parallel = m_r \Omega_{cp} \tag{2.44}$$

requires large $v_\parallel$ when $m \neq m_r$. The phase space density decreases significantly with increasing velocity, therefore the major contribution to wave growth is from the resonance with $m_r = m$ and $v_\parallel = 0$.

The wave convective growth rate can be simplified as:

$$K_i \propto \int_0^\infty dv_\perp m^2 J_m^2 (\frac{k_\perp v_\perp}{\Omega_{cp}}) \tag{2.45}$$

where J_m is the Bessel function. When $m > 3$, K_i obtains the maximum value when $v_\perp \sim \frac{\omega}{k_\perp}$. Therefore, magnetosonic waves will grow (damp) if the phase space density gradient is positive (negative) at a perpendicular velocity comparable to the wave phase speed. Because the wave phase speed is related to the Alfven velocity $v_A = \frac{B}{\sqrt{\mu_0 \rho}}$, the wave growth rate is strongly modulated by the

relation between the ion ring distribution and the ion energy corresponding to the Alfven speed.

The wave vector $\mathbf{k}$ of magnetosonic wave is almost perpendicular to the background magnetic field $\mathbf{B}_0$, thus the magnetosonic wave propagates in the equatorial plane which leads to the narrow latitudinal distribution. The waves can propagate both radially and azimuthally. The propagation paths of waves obey Snell's law, which means that the rays are refracted towards higher refractive index direction. In absence of density structures, as L shell increases, since the background magnetic field strongly decreases, the refractive index of magnetosonic waves increases until the wave frequency reaches the local lower hybrid resonance frequency. Therefore, in general the magnetosonic waves are refracted away from the Earth. However, because the density drops significantly near the plasmapause boundary, the refractive index drops significantly from inside to outside the plasmapause. The refractive index forms a local maximum value adjacent to the plasmapause boundary, and the rays on either side are refracted towards the local peak, naturally forming a trapping region of magnetosonic waves in the plasmasphere. The trapped magnetosonic waves are able to obtain multiple energy gains when they pass the energy source from ion ring distributions.

Magnetosonic waves interact with radiation belt electrons mainly through Landau resonance. Landau resonance is due to the wave electric field parallel to the particle's velocity in the frame of moving particle, or equivalently, due to the wave electric field parallel to $\mathbf{B}_0$ in the frame of moving particle when considering the particle's gyration and bounce motion. Figure 2.5 presents one example of the resonance ellipse for the interaction between oblique magnetosonic waves and energetic electrons. The central wave frequency is 33.3 Hz, central wave normal angle is 89°, and the interactions occur around $L = 4.5$ outside the plasmapause. Landau resonance (central vertical line) may lead to electron acceleration from tens of keV up to ~ 1 MeV. The first order cyclotron resonance requires a particle

velocity of $v_{\parallel} = (\omega - \Omega_{ce})/k_{\parallel}$, which corresponds to an electron energy higher than $\sim$ 10 MeV, and therefore is not important in energetic particle dynamics. In addition, because the magnetosonic waves are confined in a narrow region near the equator, the electrons may experience only a fraction of the waves, which may cause the scattering in pitch angle and energy due to the perpendicular electric fields. This transit time effect provides additional scattering to the pure Landau resonance.

The characters of magnetosonic waves are unique and interesting, and may need focused study even with good understanding of other whistler-mode waves in the inner magnetosphere. In the following Chapters, the above properties will be addressed in great detail, constituting a comprehensive study about the equatorial magnetosonic waves.

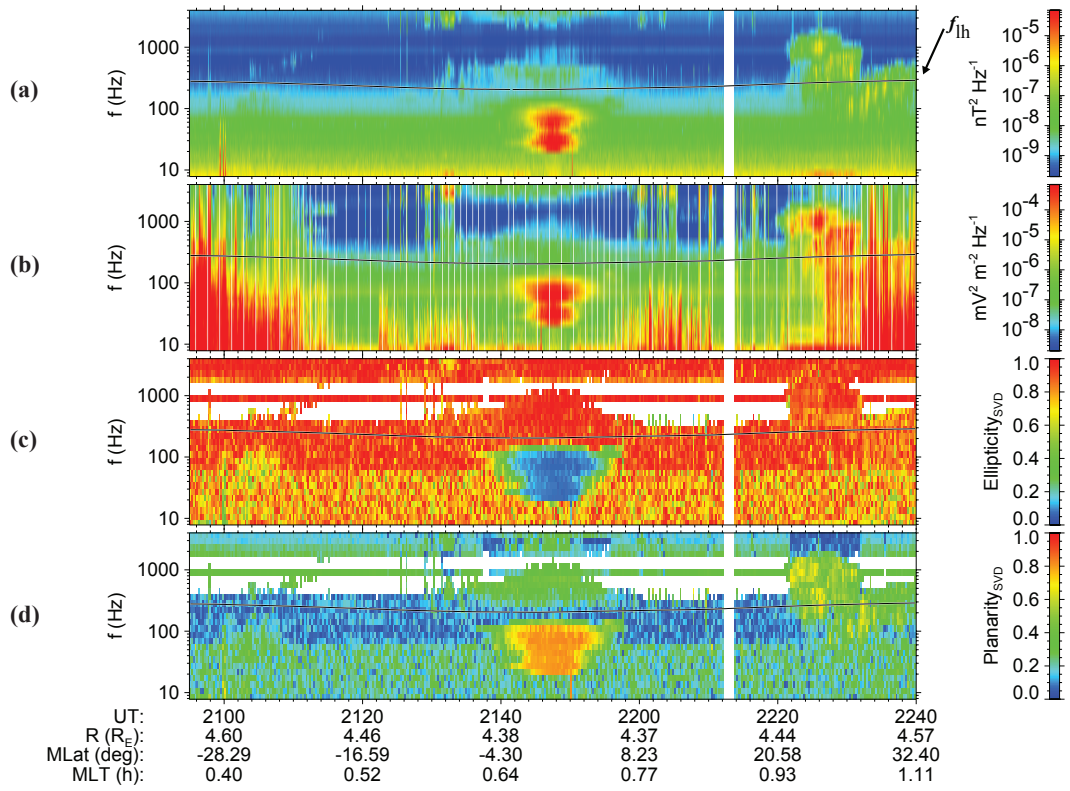

Figure 2.1: Example of data collected by Cluster 4 on 17 February 2002. From the top: (a) sum of the power-spectral densities of the three magnetic components, (b) sum of the power-spectral densities of the two electric components ; (c) ellipticity and (d) planarity are determined using the singular value decomposition of the magnetic spectral matrix. Universal time (UT) and position of the spacecraft are given on the bottom of the figure using the radial distance (R) in the Earth radii (R_E), magnetic dipole latitude (MLat) in degrees, and magnetic local time (MLT) in hours. Maximum possible value of the local lower hybrid frequency (f_{LHR}) is plotted over all four panels. The data in panels (c) and (d) are not shown for weak signals below $10^{-9} nT^2$ Hz. [*Santolík et al.*, 2004]

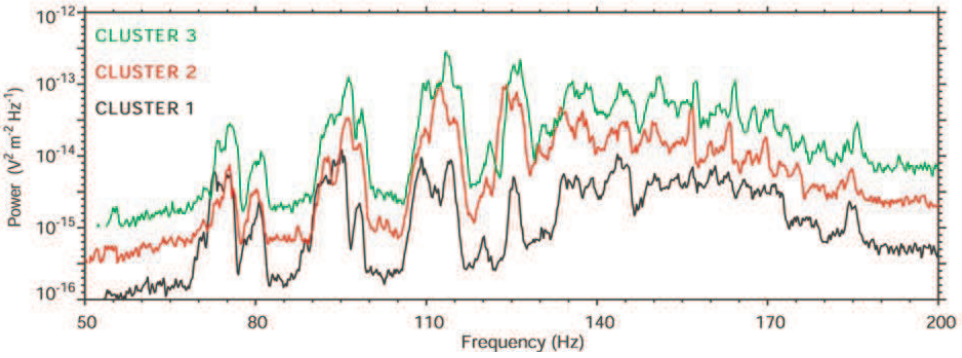

Figure 2.2: Magnetic power spectra as a function of wave frequency observed by Cluster 1, 2, and 3 between 16:40 and 16:50 UT on 4 December 2000. Vertical scale is drawn for Cluster 1 (black solid line), spectrum from Cluster 2 (red line) is shifted upward by half an order of magnitude, and the spectrum of Cluster 3 (green line) is shifted by an order of magnitude. [*Santolík et al.*, 2002]

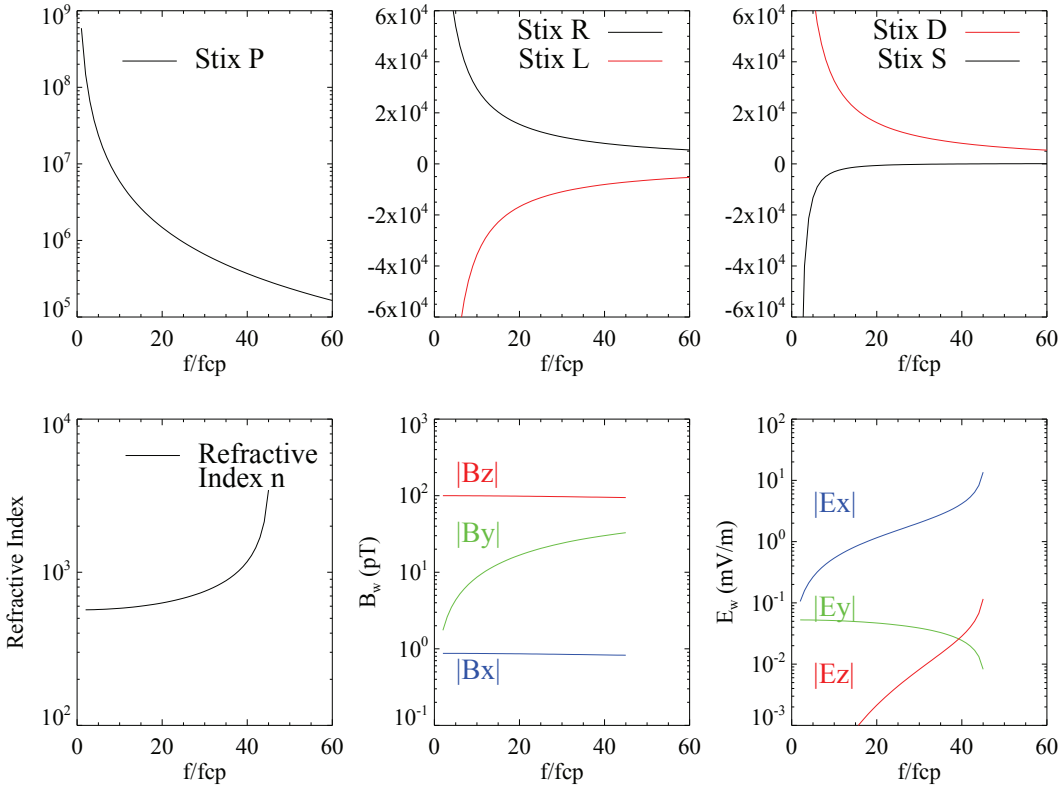

Figure 2.3: Stix parameters P, R, L, S, and D, refractive index n, and absolute values of wave electric (E) and magnetic (B) field components for typical magnetosonic waves at $L = 4.5$ inside the plasmapause. The wave normal angle is 89.5°. Sheeley's density model is used.

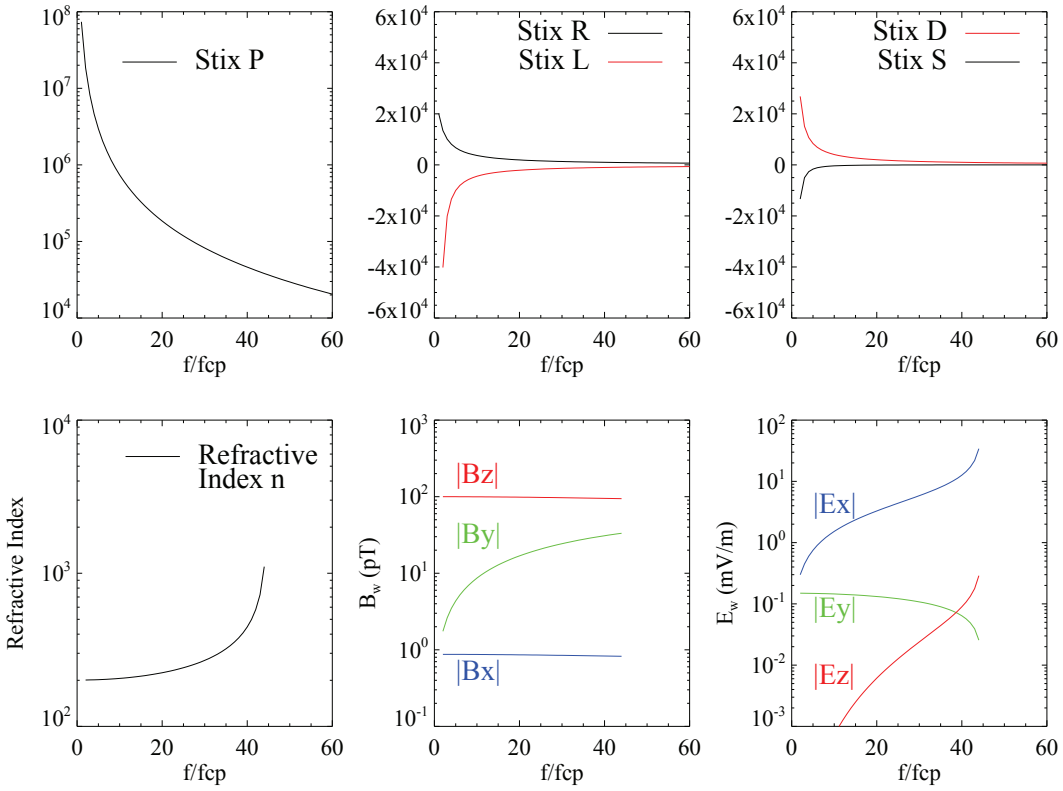

Figure 2.4: Stix parameters P, R, L, S, and D, refractive index n, and absolute values of wave electric (E) and magnetic (B) field components for typical magnetosonic waves at $L = 4.5$ outside the plasmapause. The wave normal angle is 89.5°. Sheeley's density model is used.

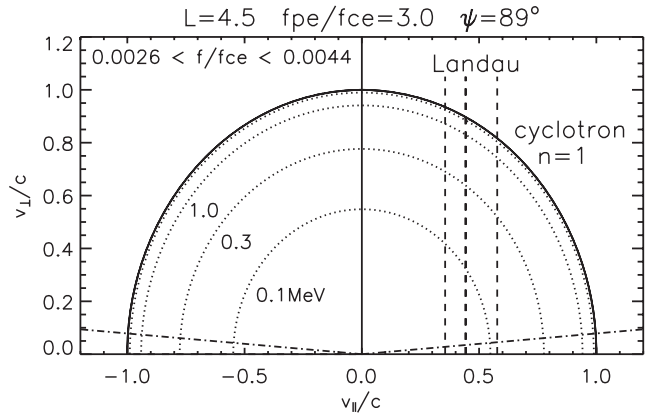

Figure 2.5: Resonant ellipse for magnetosonic waves interacting with electrons, showing (dashed) Landau $n = 0$ and (solid) $n = 1$ Doppler shifted cyclotron resonances, (dotted) circles of constant electron energy, and (dash-dotted) loss cone. The central dashed line is for Landau resonance at $X_m = \tan 89°$, the lines either side are for propagation with a range of wave normal angles $X_m \pm X_w$ where X_m is the width. [*Horne et al.*, 2007]

CHAPTER 3

Global distribution of equatorial magnetosonic waves observed by THEMIS

This Chapter addresses the observation of equatorial magnetosonic waves in the inner magnetosphere. A statistical study of equatorial magnetosonic wave properties and spatial distributions is performed. Specifically, we investigate the wave magnetic power spectrum data from three THEMIS spacecraft over the period from May 2010 to November 2012. The THEMIS spacecraft have equatorial orbits and provide good data coverage for magnetosonic wave observations near the equator and between 2 R_E and 8 R_E. Our global survey result provides essential information of the wave distributions. We have found that strong amplitudes and high occurrence of magnetosonic waves are generally observed near the equator, outside the plasmapause, on the dawnside, around $L = 4$, and during geomagnetically disturbed periods. The increase of geomagnetic activity shifts the magnetosonic wave distribution towards earlier magnetic local time. The strong magnetosonic waves generally have Root-Mean-Square averaged wave amplitude of $\sim$ 50 pT and an occurrence rate of $\sim$20%, which are mainly located on the dawnside outside the plasmapause. Our survey of the wave distribution suggests that magnetosonic waves may have an important influence on pitch angle scattering of ring current ions and Landau acceleration of energetic electrons in the Earth's radiation belts.

This chapter is organized as the following sections: Section 3.1 is a brief introduction about the magnetosonic waves, and we will mainly focus on the previous

observations of magnetosonic waves prior to the THEMIS mission; Section 3.2 discusses the analysis of magnetosonic waves using THEMIS fff dataset, and specifically presents one example of magnetosonic wave event observed by THEMIS; Section 3.3 presents the global distribution of Root-Mean-Square averaged magnetosonic wave amplitudes based on the 31 months THEMIS dataset; using the same dataset, Section 3.4 presents the global distribution of magnetosonic wave occurrence rate; to discuss the wave amplitude at different frequency bands, Section 3.5 presents the global distribution of wave amplitudes divided into lower and upper wave frequency bands; Section 3.6 summarizes the results and provides the necessary wave information for radiation belt modeling.

3.1 Introduction

Equatorial magnetosonic waves are natural electromagnetic emissions occasionally observed in a spatially localized region near the Earth's magnetic equator [*Santolík et al.*, 2004]. The waves are highly oblique, and propagate radially and azimuthally, in the direction nearly perpendicular to the background magnetic field around the magnetic equator [*Kasahara et al.*, 1994; *Chen and Thorne*, 2012; *Nemec et al.*, 2005, 2006].

The waves are excited by the drifting ion ring populations from the plasma sheet at frequencies between the proton gyrofrequency (f_{cp}) and the lower hybrid resonance frequency (f_{LHR}). After energetic ions are injected from the nightside, they perform energy dependent drift motion around the Earth [*Lyons and Williams*, 1984]. As a result, the positive gradients in the perpendicular velocity distribution of protons develop mainly on the dayside. These gradients can provide the free energy to excite magnetosonic waves [*Chen et al.*, 2010; *Thomsen et al.*, 2011] and will be discussed in detail in Chapter 4.

The excited magnetosonic waves are able to resonant interact with energetic

electrons. The scattering is mainly due to Landau resonance, and magnetosonic waves with an amplitude of $\sim$ 200 pT may cause local acceleration of several hundreds keV electrons in one day [*Horne et al.*, 2007]. In addition, magnetosonic waves are spatially confined close to the magnetic equator, therefore the waves can also cause transit time scattering over a broad region of electron velocity space [*Bortnik and Thorne*, 2010]. Magnetosonic waves also cause the pitch angle scattering of plasma sheet protons, and lead to proton precipitation in the Earth's upper atmosphere [*Xiao et al.*, 2014]. In order to understand the potential important role of magnetosonic waves in the Earth's radiation belt dynamics, comprehensive global models for the spatial distribution, the occurrence of strong wave amplitudes, and the frequency spectral properties of magnetosonic waves needs to be developed, for use in future global modeling.

Previous satellites have provided magnetosonic wave observations between 2 R_{E} and 7 R_{E}. It has been confirmed that magnetosonic wave events are mainly confined within 5 degrees in magnetic latitude near the magnetic equator. The OGO 3 spacecraft first observed equatorial noise in the Earth's magnetosphere in the 1960s [*Russell et al.*, 1970]. Using the wide band wave form measurements by the Imp 6 and Hawkeye 1 satellites, *Gurnett* [1976] have shown that the equatorial noise consists of a complex superposition of many harmonically spaced lines. The spacing of the harmonic structures are modulated by the proton gyrofrequencies, and *Gurnett* [1976] suggested hat the waves are interacting with energetic protons, alpha particles, and other heavy ions trapped near the magnetic equator. Using the particle and wave data from GOES, *Perraut et al.* [1982] provided the simultaneous observation of the proton phase space density and the magnetosonic wave event, directly suggesting the close relation between them. The observed magnetosonic wave power spectra may also contain propagation information. Cluster spacecraft [*Santolík et al.*, 2002] provided evidence that the locally generated wave spectra match the harmonics of the local proton gyrofrequency, even though the

waves can propagate with a significant radial component.

Using the electric field data from the Combined Release and Radiation Effects Satellite (CRRES), *Meredith et al.* [2008] performed a more recent survey of magnetosonic waves global distribution. The wave electric field data in the frequency band of $0.5f_{\rm LHR} < f < f_{\rm LHR}$ and the particle data which are potentially unstable to excite magnetosonic waves were investigated. Figure 3.1 and 3.2 present the CRRES observation of magnetosonic wave electric field intensities outside and inside the plasmapause, respectively. The waves are mostly observed in the duskside, near the magnetic equator, between $3R_E$ and $5R_E$, and during geomagnetically disturbed conditions. The waves outside the plasmapause (Figure 3.1) are also stronger than the waves in the plasmasphere (Figure 3.2). However, the CRRES data coverage was very limited on the dayside close to the equator, where magnetosonic waves are expected to frequently occur [*Chen et al.*, 2010]. Magnetosonic waves may also have significant wave power at frequencies below $0.5f_{\rm LHR}$, which are ignored in the CRRES data survey but are important in high energy electron accelerations. In addition, it would be useful to survey the wave magnetic field amplitudes, which are direct inputs for wave-particle interaction studies in the radiation belt models. The survey by *Meredith et al.* [2008] still provided important information on the global distribution of magnetosonic waves and quantitative evaluation of their intensities.

The Time History of Events and Macroscale Interaction during Substroms (THEMIS) spacecraft is a constellation of five NASA satellites (THEMIS A through THEMIS E) which have been launched on February 2007 for the substorm study in the Earth's magnetosphere. The THEMIS spacecraft have also provided reliable and extensive statistical studies of whistler-mode waves in the inner magnetosphere [e.g., *Li et al.*, 2009, 2011]. THEMIS spacecraft have low orbital inclination angles [*Angelopoulos*, 2008], and are equipped with high time and frequency resolution wave measurement instruments, as well as high time and energy resolution

proton and electron measurement instruments. After several years of operation, THEMIS spacecraft are expected to provide good wave data coverage for different magnetic local times at low latitudes in the inner magnetosphere. Therefore, good statistical information on the magnetosonic wave distribution and other wave properties can be obtained from the direct measurements by the THEMIS spacecraft. Using THEMIS wave magnetic fields and electric fields data as well as the background plasma information over a 31 month period, we will investigate the wave magnetic field intensity and occurrence rate of magnetosonic waves, and categorize our dataset as functions of magnetic latitude (LAT), geomagnetic activity, inside or outside the plasmapause, different wave frequency bands, and wave magnetic field amplitudes. Therefore, our study provides important information regarding the regions and conditions in which the magnetosonic waves are intense and may become most effective in scattering the particles in the Earth's radiation belts.

3.2 The THEMIS database and an observed magnetosonic event

The three THEMIS inner spacecraft (A, D, and E) have highly elliptical, near equatorial orbits with the perigee of $\sim$1.5 R_{E} and apogee of $\sim$10 R_{E} to $\sim$12 R_{E} [*Angelopoulos*, 2008]. The orbits and satellites configurations are ideally suited to study the characteristics of various plasma waves and particle populations in the Earth's magnetosphere, including equatorial magnetosonic waves and the simultaneous ion ring distributions.

The THEMIS spacecraft are equipped with fine resolution wave electric and magnetic fields instruments. Electric field variations from below the spin frequency ($\sim \frac{1}{3}$ Hz) up to $\sim$ 4 kHz are measured by the Electric Field Instrument (EFI) [*Bonnell et al.*, 2008]. Magnetic field variations in the same frequency

band are measured by the Search Coil Magnetometer (SCM) [*Roux et al.*, 2008]. After obtaining the field variation measurements in both parallel and perpendicular directions with respect to the background magnetic field $\mathbf{B}_0$, the Digital Fields Board (DFB) performs data acquisition and signal process thereafter [*Cully et al.*, 2008], and produce the wave frequency spectrum information in different components. The background magnetic field is measured by the Flux Gate Magnetometer (FGM) [*Auster et al.*, 2008]. The FGM instrument also measures the low frequency fluctuations up to 64 Hz in the magnetosphere.

The THEMIS spacecraft also measure the particle fluxes in sufficient energy band coverage for the studies in the magnetosphere and fine resolution between adjacent energy channels. The Electrostatic Analyzer (ESA) measures ion distributions from 5 eV up to 25 keV and electron distributions from 6 eV up to 30 keV [*McFadden et al.*, 2008]. The full, reduced, and burst mode data contains different resolutions in pitch angles and time. The particle momentum data including plasma velocity, pressure, and temperature are also provided. The super-thermal particle distributions within the energy range from 25 keV to 6 MeV are measured by the Solid State Telescope (SST) in different pitch angle directions and different energy channels.

In this study, we have used the spacecraft potential to calculate the total electron density, similar to the methods in *Li et al.* [2010]. The spacecraft potential information is obtained from the EFI instrument; the electron thermal speed information is obtained from the ESA instrument. After inferring the total plasma density, we identify whether the spacecraft is inside the plasmapause or outside the plasmapause using the method described in *Li et al.* [2010]. Generally speaking, the spacecraft is identified as inside the plasmapause if the total plasma density stays higher than 30 cm^{-3}; otherwise, the spacecraft is outside the plasmapause.

High resolution wave power spectrum data (fff data product) have been continuously available since 1 May 2010. We have used the fff data from May 2010

to November 2012 to perform a statistical study of magnetosonic waves. The fff data are generally available for about half of the periods each day. The wave electric and magnetic field power spectra data are recorded in 64 or 32 logarithmically spaced frequency bins in the range from ∼4 Hz to 4 kHz. Wave power spectral densities with one component parallel to the spacecraft spin axis and one component in the spacecraft spin plane are recorded every 8 seconds [*Cully et al.*, 2008]. One parallel wave magnetic field and one perpendicular wave magnetic field components are continuously available; one parallel wave electric field and one perpendicular wave electric field components are available before March 2011; two perpendicular wave electric field components are available after March 2011. Although the spin axis of the spacecraft is not exactly along the background magnetic field direction, the angle between them is generally small and are mostly below 11°. We can roughly assume the wave field component along the spin axis to be parallel to the background magnetic field and refer it as the parallel component. Therefore, we define the wave field component parallel (perpendicular) to the spacecraft spin axis to be $B_\parallel$ or $E_\parallel$ ($B_\perp$ or $E_\perp$) hereafter.

Figure 3.3 shows one typical magnetosonic wave event in association with ion ring distributions observed by THEMIS A from 01:00 UT to 02:30 UT on 15 February 2011. The seven panels show: (a) the total plasma density (inferred from the spacecraft potential); (b) energy spectrum of ion energy flux for a pitch angel of $\sim 90°$; (c) energy spectrum of ion phase space density for a pitch angle of $\sim 90°$; (d) power spectral density of $E_\perp$; (e) $E_\parallel$; (f) $B_\parallel$; (g) $B_\perp$. f_{LHR} and $0.5f_{\mathrm{LHR}}$ are denoted as the dash-dotted line and dotted line respectively. The red arrows in panel (c) indicate several examples of the positive gradients in ion PSD distribution. The spacecraft travels from outside the plasmapause to inside the plasmapause. Figure 3.3a shows that the total plasma density is $\sim 10cm^{-3}$ outside the plasmapause, and increases to $\sim 5000cm^{-3}$ inside the plasmapause. The plasmapause boundary is identified around 01:45 UT with a sharp increase

in density.

Magnetosonic waves are highly oblique plasma emissions, and are characterized with much stronger $E_\perp$ and $B_\parallel$ intensities compared with $E_\parallel$ and $B_\perp$, i.e. $E_\perp \gg E_\parallel$ and $B_\parallel \gg B_\perp$. In this event, magnetosonic waves are observed outside the plasmapause before $\sim$ 01:50 UT and inside after $\sim$ 01:50 UT. The waves are located within $\sim$ 2.3° of the magnetic equator and magnetic local time coverage from dawnside to noon. Outside the plasmapause, the magnetosonic wave frequencies vary from 30 Hz to 200 Hz due to the changes in the proton gyrofrequency. Two distinct frequency bands of magnetosonic waves are observed with the frequencies following the variation of $f_{\rm LHR}$ (the white dash-dotted line) or $0.5f_{\rm LHR}$ (the white dotted line). The major magnetic wave power is in the lower frequency band, and the dominant wave power in both frequency bands mainly occurs below $0.5f_{\rm LHR}$ as shown in Figure 3.3d and 3.3f.

Figure 3.3b presents the ion flux distribution with a pitch angle of $\sim 90°$. There are clearly ion ring injections at energies above 10 keV outside the plasmapause. We calculate the ion phase space density distributions for a pitch angle of $\sim 90°$ in Figure 3.3c based on the ion flux data. The positive gradients of the ion PSD as a function of energy are observed simultaneously with the observations of magnetosonic waves for ions with energy higher than $\sim$10 keV. This indicates that the waves outside the plasmapause are probably locally excited consistent with previous studies.

Inside the plasmapause, magnetosonic waves are also characterized by the properties that $E_\perp$ (Figure 3.3d) is much stronger than $E_\parallel$ (Figure 3.3e) and $B_\parallel$ (Figure 3.3f) is much stronger than $B_\perp$ (Figure 3.3g). Magnetosonic waves are observed between 40 Hz and 200 Hz with nearly unstructured frequency spectra. However, the ion phase space density data provide no evidence of local positive ion phase space density gradients, which suggests that the magnetosonic waves inside the plasmapause are not locally generated and have probably propagated

to this location from a distant source. This is a common feature of magnetosonic waves inside the plasmapause. THEMIS A has also observed the plasmaspheric hiss emissions inside the plasmapause in the frequency range from 300 to 600 Hz. The hiss wave frequencies are not modulated by the proton gyrofrequency trends. In addition, the hiss waves propagate mainly in the parallel direction to the background magnetic field. In this event, $B_\perp$ is comparable to $B_\parallel$ for the hiss emissions, which indicates that the emissions in the frequency range from 300 to 600 Hz are not as oblique as magnetosonic waves. This feature allows us to set up the magnetosonic wave automatic selection criteria based on the relative ratio between different directions of wave fields in the following Section 3.3.

3.3 Magnetosonic wave amplitude distribution observed by THEMIS

We use wave electric and magnetic field fff product data in the frequency band of 30 Hz $< f <$ 1000 Hz observed by THEMIS probes A, D, and E for our statistical study of magnetosonic waves. The magnetosonic waves generally occur between the local proton gyrofrequency and the lower hybrid resonance frequency in the inner magnetosphere. Therefore, the frequency band of 30 Hz $< f <$ 1000 Hz should cover the essential part of the magnetosonic wave power especially at low L shells. The analysis of magnetosonic waves needs further caution, however, since there are other emissions that share a similar frequency band and location. As shown in Figure 3.3, plasmaspheric hiss waves are also frequently observed in the frequency band of 30 Hz $< f <$ 1000 Hz near the dayside, which need to be distinguished from the magnetosonic wave emissions.

We utilize the property of highly oblique magnetosonic wave propagation and use the following criteria for selecting magentosonic waves from other emissions, which can be verified in cold plasma theory [e,g., *Stix*, 1992]. 1. $E_\perp/E_\parallel$ is greater

than 3 outside the plasmapause and greater than 4 inside the plasmapause; 2. $B_{\parallel}/B_{\perp}$ is greater than 1.5 outside the plasmapause and greater than 2 inside the plasmapause. Note that we set the ratio inside plasmapause higher in order to remove plasmaspheric hiss waves. Furthermore, since the frequency of magnetosonic waves ranges between $f_{\rm cp}$ and $f_{\rm LHR}$, the region in which the majority of magnetosonic wave power can be measured is also limited due to the frequency range of 30 – 1000 Hz from fff data. We have calculated the wave amplitudes by integrating the magnetosonic wave power as a function of frequency based on the selection criteria.

We have performed data cleaning procedures for the fff data product. The spikes in electric field power spectrum data are not realistic and are automatically removed based on the fact that they present sudden increase in electric field measurements; we have also removed the background magnetic noise signals at frequencies below 40 Hz by subtractions. Figure 3.3 is presenting the wave power spectra after the cleaning procedures.

In our 31 months survey, a valid observation point is defined as the time point in the wave electric and magnetic power spectrum data satisfying the following conditions to observe magnetosonic waves: 1. the valid fff data product in both electric and magnetic fields are available at the time point; 2. the local proton gyrofrequency is lower than 1000 Hz; 3. the lower hybrid resonance frequency is higher than 30 Hz; 4. the spacecraft should be located between 2 R_E and 8 R_E. We require that a reliable statistics should contain measurements of more than 100 time points. Base on the data coverage of the magnetosonic wave measurements, the THEMIS fff wave data are binned into grids of 0.5 $R_{\rm E}$ $\times$ 2 MLT in the region $2 < L < 8$. Therefore, there are 16 data bins in L shell and 12 data bins in local times. The data coverages are presented as the small globes in Figures 3.4, 3.5, and 3.6, which clearly show that the data coverages are excellent near the magnetic equator at latitudes less than 5° under different geomagnetic conditions.

Although there is a data gap in the afternoon sectors at higher latitudes, it will not affect our survey of magnetosonic waves because the waves are mainly confined near the magnetic equator and the occurrence at higher latitudes are lower.

Figure 3.4 shows the global distributions of the root mean square (RMS) magnetic field amplitude ($B_{\rm w}$) of magnetosonic waves. We have categorized our results by AE* and LAT to compare the wave distributions at different geomagnetic conditions and different latitude ranges. Here AE* is the maximum geomagnetic AE index in the previous 3 hours. The wave distributions are also shown both inside (top panels) and outside (bottom panels) the plasmapause. We only integrated the spectral densities above 30 Hz to calculate the magnetosonic wave amplitude, since the fff data product provide reliable wave spectral density above $\sim$ 30 Hz. This ensures that the essential magnetosonic wave power is counted at $L <\sim 6$, but the wave amplitudes at higher L shells are restricted to the higher normalized wave frequencies in general above $\sim 0.4 f_{\rm LHR}$ (about $17 f_{cp}$). The wave amplitudes are plotted as a function of L shell and magnetic local time between 2 R_E and 8 R_E with the Earth at the center. The dayside is in the upward direction.

Strongest magentosonic waves are found on the dawnside, between 3 – 5 R_E, at $|{\rm LAT}| \leq 5^\circ$, in the region outside the plasmapause, for geomagnetically disturbed conditions (AE* $>$ 300 nT), as shown in Figure 3.3i. The magnetosonic wave amplitudes both inside and outside the plasmapause are stronger at lower magnetic latitudes, consistent with previous studies [e.g. *Meredith et al.*, 2008]. It is interesting to note that relatively high latitude ($|{\rm LAT}| > 5^\circ$) but weak magnetosonic waves are observed at low L shells and under disturbed conditions both inside and outside the plasmapause. The magnetosonic wave amplitudes inside the plasmapause are much weaker than those outside the plasmaspause. However, the magnetosonic waves inside the plasmapause have a more uniform distribution than the waves outside the plamapause, probably because of the propagation effects. The magnetosonic wave distribution outside the plasmapause shows

stronger wave amplitudes for larger AE*, therefore the wave activities are strongly related to the particle injection events. Interestingly, as AE* increases the wave distribution outside the plasmapause shifts towards earlier magnetic local time. The strongest RMS averaged wave amplitude of magnetosonic waves is $\sim$ 50 pT, and it is predominantly observed in the prenoon sectors outside the plasmapause near the equator under disturbed conditions, suggesting that magnetosonic waves may be particularly important in particle scattering in those regions [e.g., *Horne et al.*, 2007].

3.4 Magnetosonic wave occurrence rate distribution observed by THEMIS

Besides the time averaged wave amplitude distribution of magnetosonic waves, the percentage of time that the strong magnetosonic waves occur is an other important issue that controls the roles of the waves in the radiation belt dynamics. Figure 3.5 shows the global distribution of the magnetosonic wave occurrence rate for various levels of wave amplitude and at different latitude ranges using a similar format to Figure 3.4. The occurrence rate is defined as the ratio between the number of time points during which magnetosonic waves are observed and the total number of time points with valid observations. The occurrence rates of magnetosonic waves are plotted as a function of L shell and magnetic local time for both inside the plasmapause (upper panels) and outside the plasmapause (lower panels). The sample numbers are also plotted as smaller globes on each right bottom foot, which shows that the data coverage is sufficiently high for reliable statistics.

We are mostly interested in the occurrence rate distributions of strong magnetosonic waves with magnetic wave amplitude greater than 50 pT. Although the small wave amplitude waves have high occurrence rates, the occurrence rates of strong magnetosonic waves are mostly less than 10%. The occurrence rate of

strong magnetosonic waves with $B_{\rm w} > 50$ pT peaks near 20% outside the plasmapause at $L \sim 4$, near the equator, and in the dawn sector. The magnetic local time distribution of the strong amplitude waves maybe related to the shifting trends in MLT with increasing AE*. Consistent with the results in Figure 3.4, the magnetosonic waves at all levels of wave amplitudes occur more frequently near the equator than slightly off equator, and outside the plasmapause than inside the plasmapause. The waves inside the plasmapause have more uniform distribution in MLT than outside, although the strong waves rarely occur inside the plasmapause during the 31 months period. The majority of magnetosonic wave events inside the plasmapause investigated in the present study, although not explicitly shown, tend to have nearly constant frequency spectra, while the waves outside the plasmapause tend to follow the variations of $f_{\rm LHR}$, as shown in Figure 3.3. This supports the concept that the magnetosonic waves inside the plasmapause are likely to have propagated azimuthally and radially from other regions, while the magnetosonic waves outside the plasmapause are more likely to be excited locally.

Magnetosonic waves with amplitude higher than 100 pT may acceleration energetic electrons in several days. We have also investigated the occurrence rate of magnetosonic waves with $B_{\rm w} > 100$ pT (not shown), and found that the peak value is ~ 0.1 and is located in a very limited MLT range in the dawn sector outside the plasmapause near the equator. They correspond to several large amplitude magnetosonic wave events close to the plasmapause boundary during disturbed conditions. When AE* is large, the plasmapause location tends to be pressed to lower L shells as low as 3 R_E. Meanwhile, there are also strong particle injections which provide free energy for magnetosonic wave excitation. Therefore, high amplitude magnetosonic waves are generated at low L shells outside the plasmapause. The generation mechanism will be further discussed in Chapter 4.

3.5 Magnetosonic wave intensities at different frequency bands

Magnetosonic waves in different frequency bands are excited based on the relation between the background plasma conditions and the injecting ion ring populations [e.g., *Chen et al.*, 2010, 2011; *Jordanova et al.*, 2012]. In general, lower (higher) frequency magnetosonic waves may be generated at higher (lower) density region or lower (higher) background magnetic field region [*Ma et al.*, 2014a]. In addition, the wave frequency also determines the resonance energy when the magnetosonic waves resonant interact with the particles. It is therefore necessary to investigate the magnetosonic wave intensities over different frequency bands.

Following the statistical study by *Meredith et al.* [2008], we have simply investigated the amplitude of magnetosonic waves integrated over the lower frequency band ($f_{\rm cp} < f \leq 0.5 f_{\rm LHR}$) and higher frequency band ($0.5 f_{\rm LHR} < f < f_{\rm LHR}$) separately. However, due to the lower cutoff frequency limit of $\sim$ 30 Hz in fff data product, magnetosonic wave amplitudes are probably underestimated for the lower frequency band especially at higher L shells. It is worth noting that both the lower and the higher frequency bands need to be incorporated in radiation belt modeling because the waves in different frequency bands may mainly affect different particle populations.

Figure 3.6 shows the global distribution of RMS averaged wave amplitudes for lower and higher frequency bands. The statistics are categorized by AE* index, both inside (top panels) and outside (bottom panels) the plasmapause. The latitudinal range of magnetosonic waves is not restricted here because the major power of the statistics is from the equatorial region. Although the data coverage of the higher frequency magnetosonic waves (smaller globes at the right bottom side of each panel) are higher than the data coverage of lower frequency waves, the lower frequency band magnetosonic waves are much more intense than the

higher frequency band waves for all geomagnetic conditions both inside and outside the plasmapause. The results indicate that the majority of the wave power is contained in the frequencies lower than $0.5 f_{\mathrm{LHR}}$, consistent with the magnetosonic wave event shown in Figure 3.3. On the other band, as AE* increases, the lower frequency band wave intensity increases significantly both inside and especially outside the plasmapause, but the higher frequency band wave intensity remains similar. Those interesting features may provide more detailed clues about the excitation of magnetosonic waves, and may imply that the magnetosonic waves excited at lower density regions are weaker than the waves excited at higher density regions, or it is more common that the positive gradients in ion phase space density distributions exist in slightly higher density regions even though they are still outside the plasmapause.

3.6 Conclusions and discussions

The main purpose of this chapter is to discuss the global distribution of magnetosonic waves. We have used THEMIS fff data for a statistical study of magnetosonic wave properties and global distributions in the Earth's magnetosphere. The survey has focused on the magnetosonic wave magnetic field intensity in the frequency range roughly from 30 Hz to the lower hybrid resonance frequency.

The THEMIS wave database provides excellent coverage in the major region of magnetosonic waves especially near the magnetic equator. The additional measurements near the dayside improve significantly over the limited range in the earlier analysis by *Meredith et al.* [2008] from CRRES wave data. In general, our THEMIS statistics of magnetosonic wave distribution agrees fairly well with the statistics by *Meredith et al.* [2008]. Our statistical results are also consistent with previous simulation results based on the excitation of magnetosonic waves [*Chen et al.*, 2010; *Jordanova et al.*, 2012] especially outside the plasmapause where lo-

cally excited magnetosonic events are mainly observed. Inside the plasmapause, the wave propagation effects may become more important to account for the uniform wave distributions, which will be addressed in Chapter 5. A recent survey by *Shprits et al.* [2013] has used the THEMIS Filter Bank (FBK) data that provide the spectra of magnetic amplitudes in the direction perpendicular to the spin axis, which is nearly perpendicular to the ambient field B_0. Their results has indicated that typical magnetosonic wave amplitudes detected in the FBK data are relatively small (< 25 pT) and are weaker than our statistical survey results. The probability of occurrence in their results are also much lower than our results. However, since magnetosonic waves are highly oblique whistler-mode emissions, the component of the wave magnetic field parallel to $\mathbf{B}_0$ is the dominant magnetic field component as demonstrated in Figures 2.3, 2.4, and Figure 3.3. Consequently, the use of FBK data in the recent analysis of *Shprits et al.* [2013] greatly underestimates the true amplitude of magnetosonic waves. Our present analysis shows that magnetosonic waves have RMS amplitudes comparable to 50 pT in the pre-noon sector during active conditions, with peak amplitudes over 100 pT. Such waves may have an important impact on electron dynamics [e.g., *Horne et al.*, 2007] and need to be considered in global radiation belt modeling.

Our main conclusions in this chapter are summarized as follows: 1. strongest magnetosonic waves with wave magnetic field amplitude of ~ 50 pT and wave occurrence rate of $\sim 20\%$ occur near the magnetic equator, in the dawn sector, outside the plasmapause, under disturbed conditions; 2. the magnetosonic waves outside the plasmasphere are stronger than the waves inside the plasmapause, and the magnetosonic waves are distributed more uniformly in local times inside the plasmapause than outside; 3. the magnetosonic wave amplitudes are stronger near the equator than those at higher latitudes; 4. the increase in AE* has more influence for the waves outside the plasmapause than inside, and the location of strongest magnetosonic waves shifts to earlier magnetic local times particularly

in the region outside the plamasphere; 5. the wave amplitudes in the lower half frequency band ($f_{\rm cp} < f \leq 0.5 f_{\rm LHR}$) are larger than those in the higher half frequency band ($0.5 f_{\rm LHR} < f < f_{\rm LHR}$) at different geomagnetic conditions both inside and outside the plasmapause. We note that due to the limited reliable frequency range ($>\sim$ 30 Hz) of fff data, magnetosonic wave amplitudes shown at larger radial distances beyond $\sim 6 R_{\rm E}$ in the present study are probably underestimated, especially in the frequency band below $0.5 f_{\rm LHR}$. These waves can be analyzed further using burst captures (waveforms at 128 samples/s) on THEMIS if needed in the future, but the general conclusions should be consistent with our current study in this chapter.

We have also found that the observed magnetosonic wave frequency follows the $f_{\rm LHR}$ variation trends outside the plasmapause, whereas it tends to be constant inside the plasmapause. This suggests that magnetosonic waves observed outside the plasmapause are likely to be generated locally [e.g., *Chen et al.*, 2010, 2011; *Xiao et al.*, 2013; *Ma et al.*, 2014a], whereas magnetosonic waves inside the plasmapause are likely to have propagated from other regions [e.g., *Chen and Thorne*, 2012; *Xiao et al.*, 2012; *Ma et al.*, 2014b]. However, a more definitive study regarding this feature is left for a more extensive statistical analysis and ray tracing simulation in the future. Furthermore, since both previous simulations and event studies suggested that magnetosonic waves are probably generated by a proton ring distribution in the Earth's magnetosphere, a more extensive statistical study about the occurrence of magnetosonic waves and the ion ring distributions is needed to further investigate the generation mechanism of magnetosonic waves.

With the understanding of the equatorial magnetosonic wave distributions in the inner magnetosphere, we will discuss the formation factors of the wave distribution characters in the following chapters. In Chapter 4, we will focus on the wave generation mechanisms. It will be directly demonstrated that the magnetosonic waves outside the plasmapause tends to be locally excited; inside

the plasmapause, the waves are excited in the outer region and subsequently propagate in the plasmasphere. These results will confirm our hypotheses above.

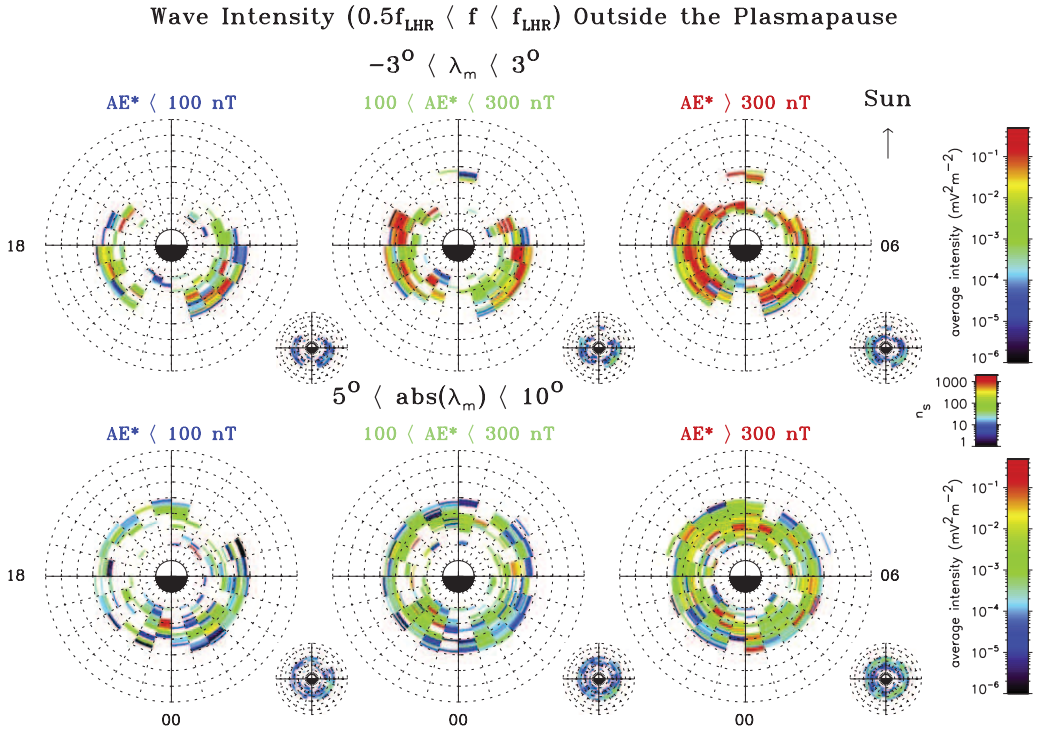

Figure 3.1: Average wave electric field intensities of (top) equatorial and (bottom) off-equatorial emissions in the frequency range $0.5f_{LHR} < f < f_{LHR}$ observed by CRRES outside the plasmasphere as a function of L and magnetic local time. From left to right the results are presented for quiet ($AE* < 100$ nT), moderate ($100 < AE* < 300$ nT), and active ($AE* > 300$ nT) conditions. [*Meredith et al.*, 2008]

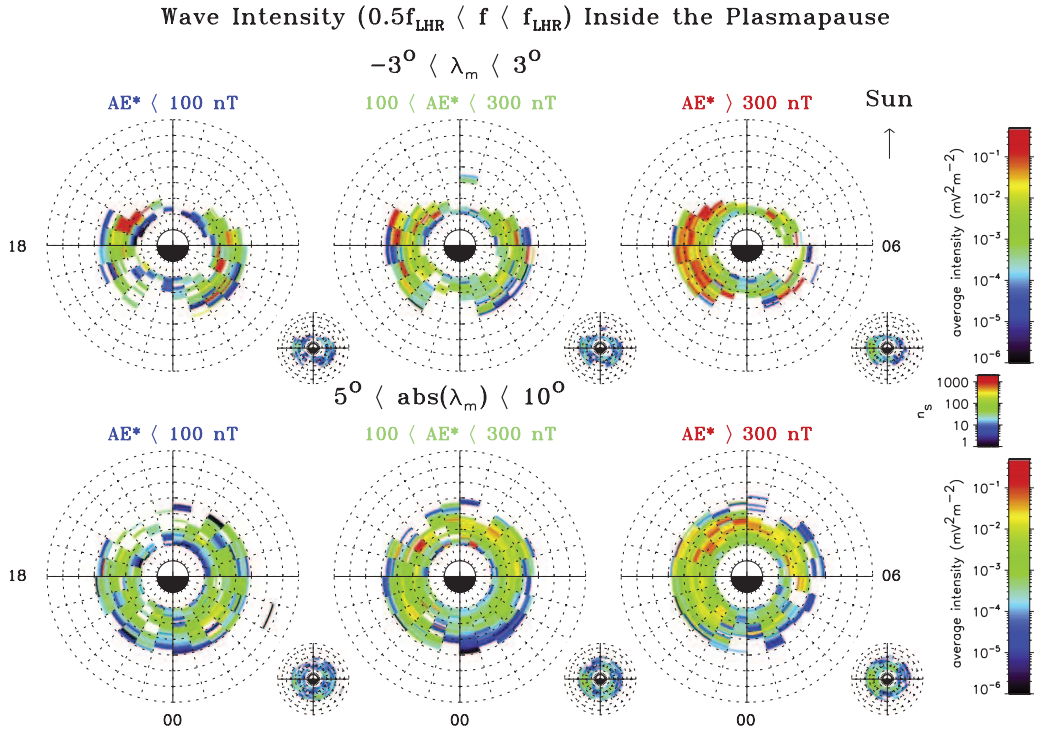

Figure 3.2: Average wave electric field intensities of (top) equatorial and (bottom) off-equatorial emissions in the frequency range $0.5f_{LHR} < f < f_{LHR}$ observed by CRRES in the plasmasphere as a function of L and magnetic local time. From left to right the results are presented for quiet ($AE* < 100$ nT), moderate ($100 < AE* < 300$ nT), and active ($AE* > 300$ nT) conditions. [*Meredith et al.*, 2008]

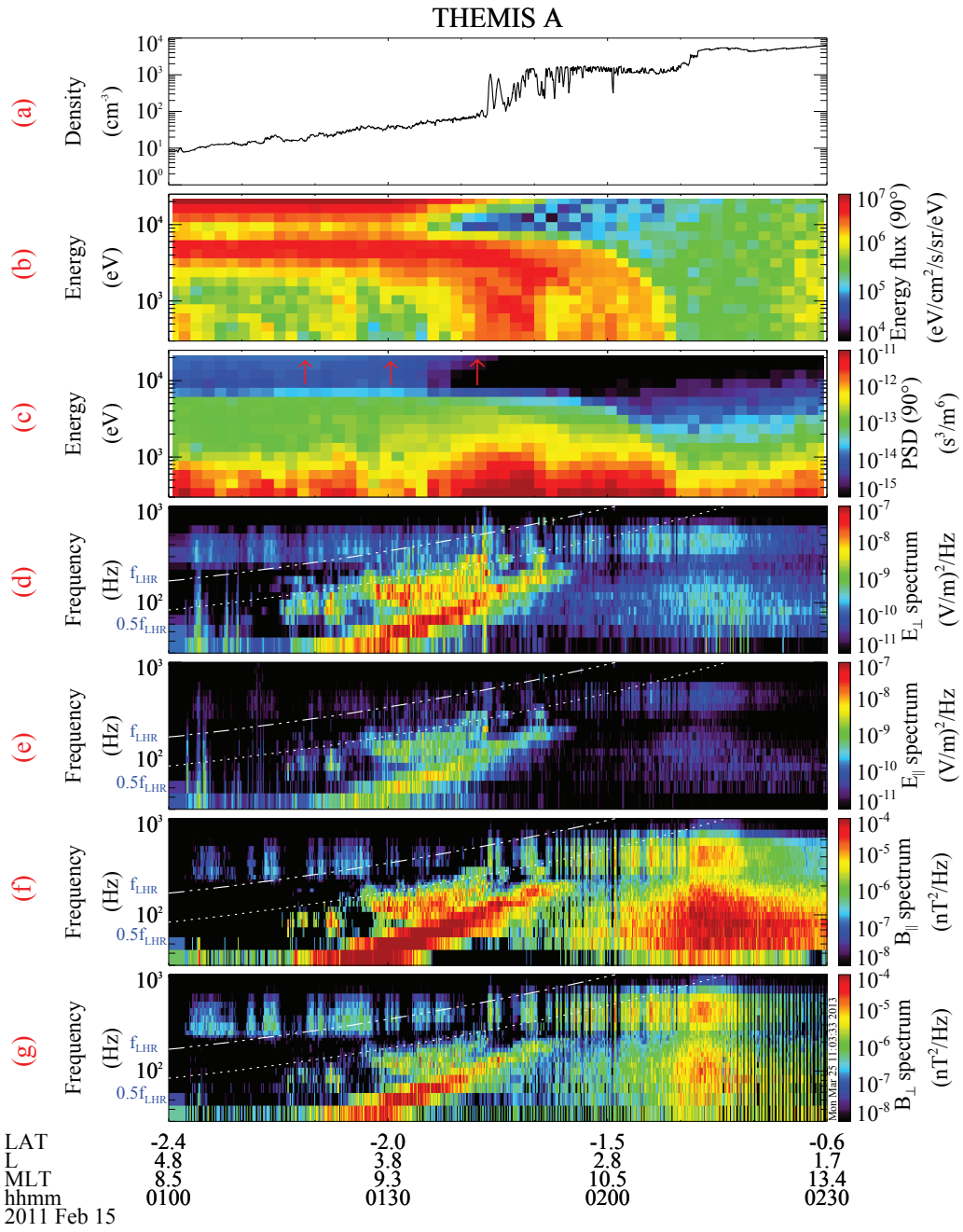

Figure 3.3: Magnetosonic waves observed by THEMIS A on 15 February 2011. The seven panels show: (a) the total plasma density; (b) energy spectrum of ion energy flux at a pitch angle of 90°; (c) the calculated energy spectrum of ion PSD; (d) power spectral density of $E_\perp$; (e) $E_\parallel$; (f) $B_\parallel$; (g) $B_\perp$.

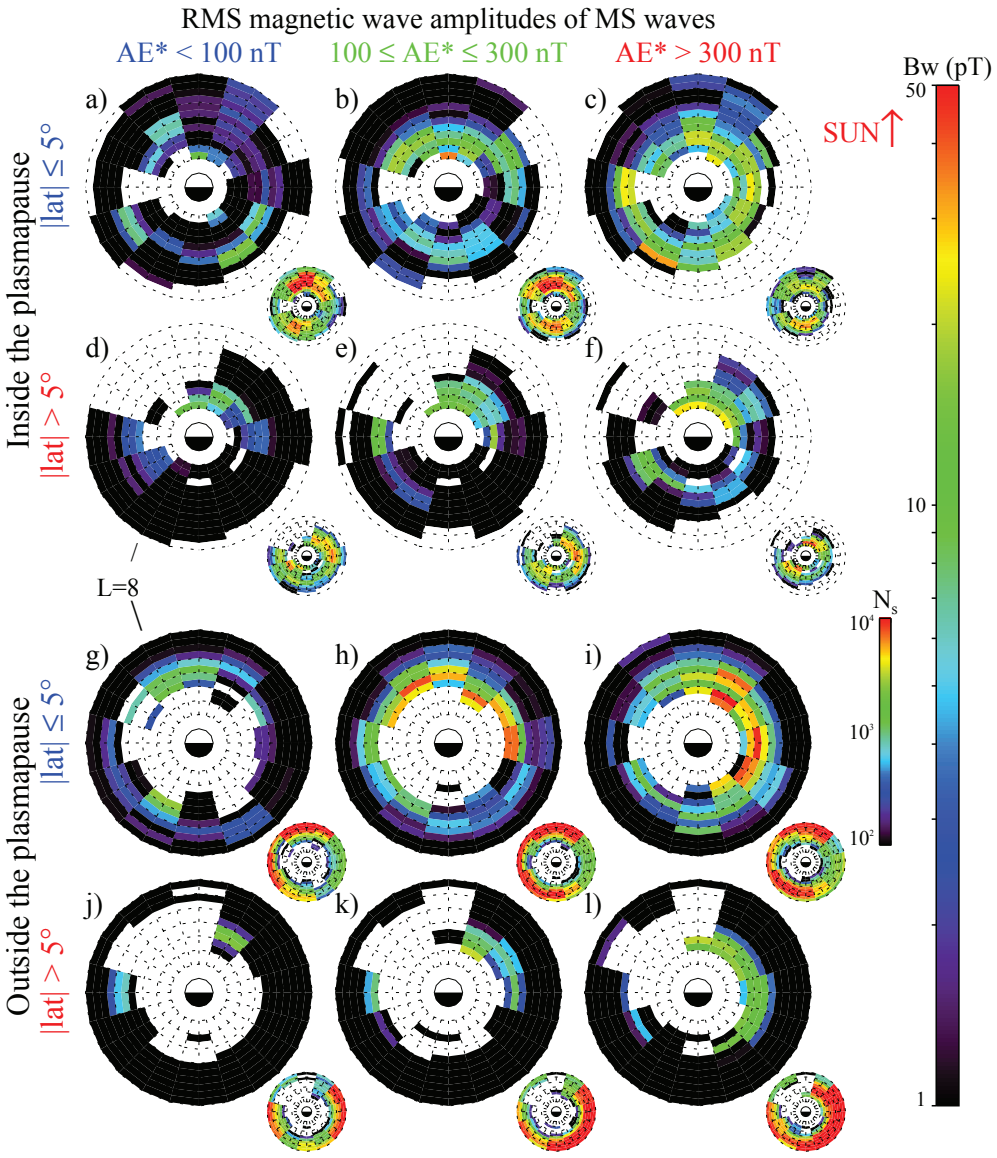

Figure 3.4: The global distribution of RMS wave amplitude B_{w} for $2 < L < 8$. The wave intensity is categorized by magnetic latitude and AE*, and shown for locations inside (top panels) and outside (bottom panels) the plasmapause. The sample number (N_{s}) is shown as smaller plots at the right bottom corner for each panel. White area represents the region where N_{s} is less than 100.

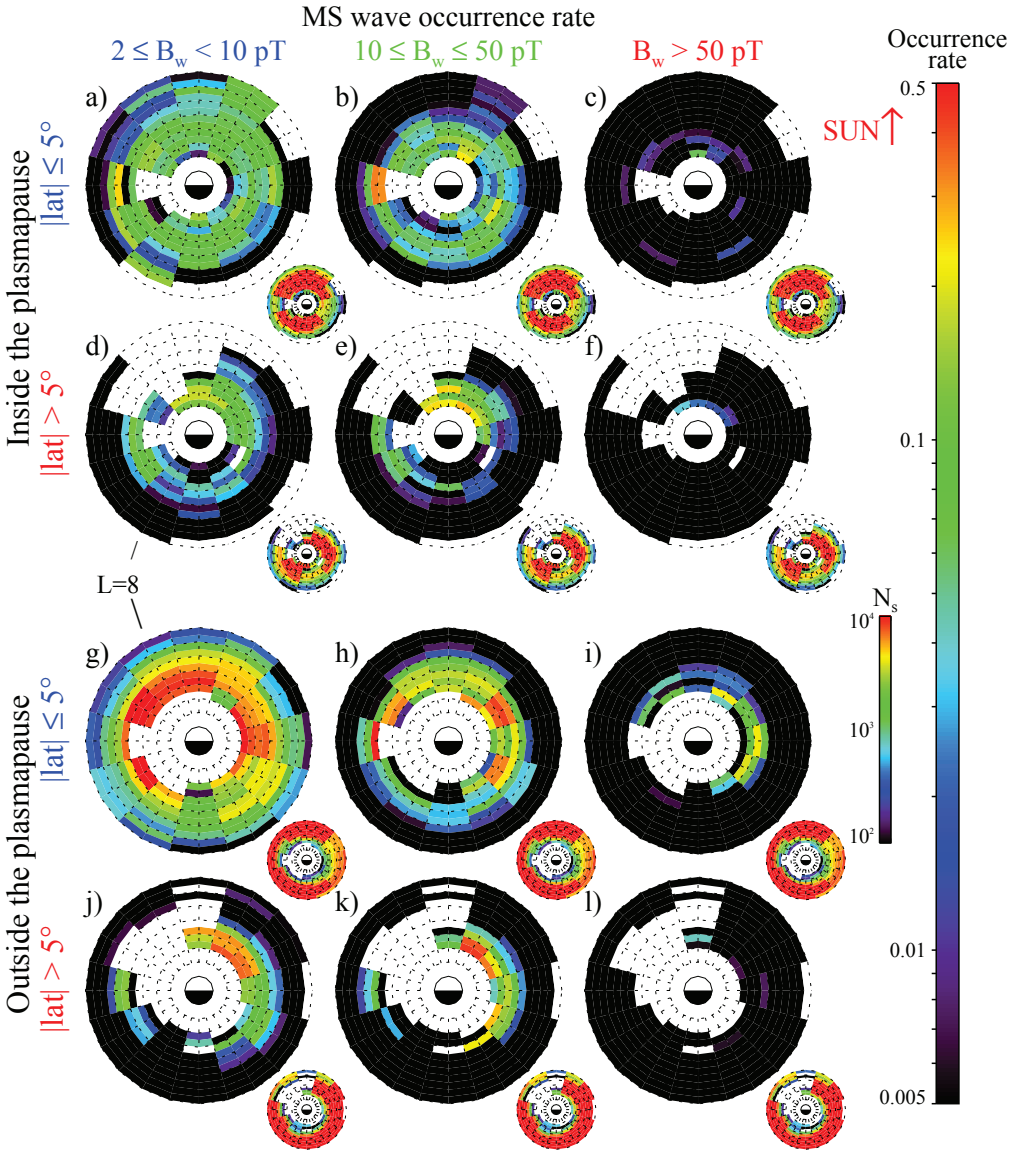

Figure 3.5: The global distribution of magnetosonic wave occurrence rate for $2 < L < 8$. The wave occurrence rate is categorized by magnetic latitude and wave amplitude range, and shown for locations inside (top panels) and outside (bottom panels) the plasmapause. The sample number is shown as smaller plots at the right bottom corner for each panel. White area represents the region where N_s is less than 100.

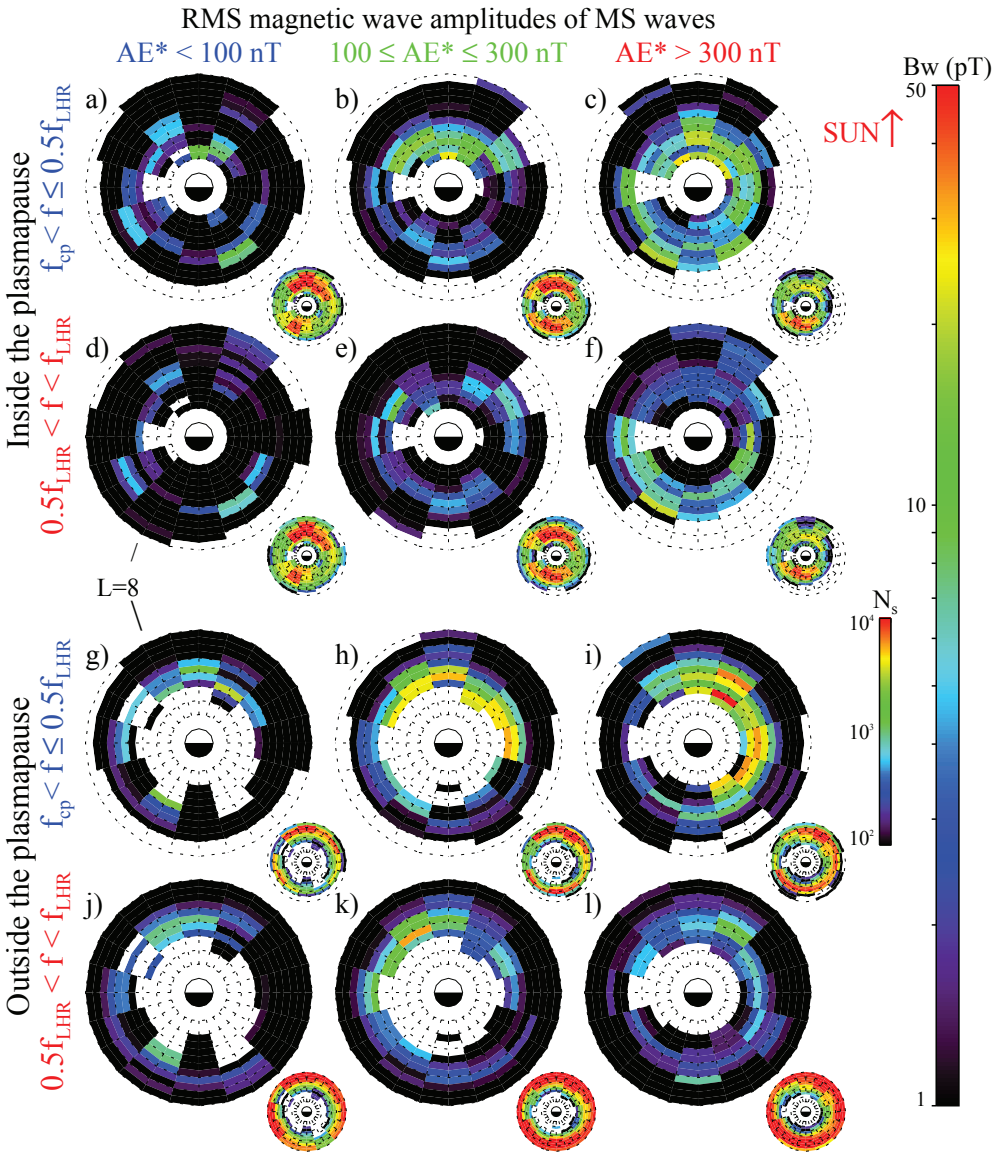

Figure 3.6: The global distribution of RMS wave amplitude B_w for higher and lower frequency band waves. The wave intensity is categorized by the frequency bands and AE*, and is shown inside (top panels) and outside (bottom panels) the plasmapause. The sample number is shown at the right bottom corner for each panel. White area represents the region where N_s is less than 100.

CHAPTER 4

Magnetosonic wave excitation by ion ring distributions in the inner magnetosphere

The physical understanding about the occurrence of equatorial magnetosonic waves is an important issue in addition to the in-situ observations. The global distribution of magnetosonic waves is presented in Chapter 3. One of the important factors that determine the wave amplitude and occurrence distribution is the energy source of the waves, i.e., the wave excitation mechanism. This chapter mainly addresses the magnetosonic wave excitation by the simultaneous evidences of ion ring distributions both inside and outside the plasmapause.

To analysis the relation between the equatorial magnetosonic waves and the potentially unstable ion ring distributions, we combine THEMIS wave and particle observations and a quantitative calculation of linear wave growth rate based on the measured proton distributions and background plasma conditions. We demonstrate that magnetosonic waves can be locally excited by ion ring distributions in the Earth's magnetosphere when the ion ring energy is comparable to the local Alfven energy. Magnetosonic waves in association with ion ring distributions were observed by THEMIS A on 24 November 2010 in the afternoon sector. Similar with other typical magnetosonic wave events, the waves were observed both outside the plasmapause where the wave spectrum varied with the trend of lower hybrid resonance frequency, and inside the plasmapause where the wave frequency band remained nearly constant. We perform plasma instability analysis in three different and representative regions. Our analysis shows that

higher and narrower frequency band magnetosonic waves are excited locally outside the plasmapause, and lower and broader frequency band magnetosonic waves are excited in the region where the density slightly increases. However, there is no evidence for wave excitation well inside the plasmapause. Our study implies that the wave propagation from a distant source is needed to explain the existence of the magnetosonic waves deep inside the plasmasphere. The simulation of the magnetosonic wave growth rate spectra during this event agrees reasonably well with the observed wave magnetic field power spectra. We also simulate another typical magnetosonic wave event on 19 October 2011 in the dusk sector. Broad band magnetosonic waves are observed in association with the ion ring distributions outside the plasmapause. We find that the ion ring distribution with an ion ring energy slightly higher than the local Alfven energy can excite the typical broad band magnetosonic waves outside the plasmapause. This chapter provides explanation for the existence of locally excited magnetosonic waves under typical plasma conditions in the Earth's inner magnetosphere.

This chapter is organized as the following: Section 4.1 is a brief introduction about the local excitation of magnetosonic waves, with a focus on the previous theoretical and observational studies about the relation between equatorial magnetosonic waves and ion ring distributions in the inner magnetosphere; Using the THEMIS spacecraft real-time observations and the magnetosonic wave instability analysis, Section 4.2 - 4.7 discuss the magnetosonic wave instability analysis under different conditions and the sensibility of our results; Section 4.8 summarizes the results and provides the scenario about the source of the magnetosonic waves in the Earth's inner magnetosphere.

4.1 Introduction

Fast magnetosonic waves are natural electromagnetic emissions excited at frequencies between the proton gyrofrequency (f_{cp}) and the lower hybrid frequency (f_{LHR}) near the Earth's magnetic equator [*Santolík et al.*, 2004]. In recent years, fast magnetosonic waves have acquired significant research interest because of their potential importance for particle scattering in the Earth's radiation belts [*Horne et al.*, 2007; *Bortnik and Thorne*, 2010]. Magnetosonic waves were first detected in the Earth's magnetosphere by the OGO 3 spacecraft and described as "equatorial noise" in the late 1960s [*Russell et al.*, 1970; *Gurnett*, 1976]. The Geostationary Operational Environment Satellite (GOES) [*Perraut et al.*, 1982] and the Cluster spacecraft [*Santolík et al.*, 2002] provided evidences that these waves could be locally generated at harmonics of the proton gyrofrequency, and that they are confined to the magnetic equatorial plane when they propagate from the source. *Meredith et al.* [2008] used the Combined Release and Radiation Effects Satellite (CRRES) data to obtain a statistical model for the magnetosonic wave electric field intensity distribution and its relationship with ion ring distributions (Figure 3.1 and 3.2). More recently, the statistical study of magnetosonic waves by *Ma et al.* [2013] using the Time History of Events and Macroscale Interaction during Substorms (THEMIS) high resolution spectral data provided the global distribution of equatorial magnetosonic waves in the Earth's inner magnetosphere, and showed that the most intense magnetosonic waves exist on the dawnside to dayside sectors outside the plasmapause. During disturbed conditions, the strongest magnetosonic waves near the magnetic equator have a root mean square averaged wave amplitudes of $\sim$ 50 pT (Figure3.4). Averaged over all different conditions, the occurrence rates of strong magnetosonic waves with amplitude greater than 50 pT is about 20% near the magnetic equator (Figure3.5).

It is generally accepted that the equatorial magnetosonic waves are excited by

the thermal ion distributions in the magnetosphere. After the particles are injected from the nightside plasma sheet to the inner magnetosphere, they perform energy and charge dependent drift around the Earth. The ring current forms due to the difference in the ion and electron behaviors. Moreover, the lower energy ions drift eastward due to the dominant co-rotational and convectional electric field drift effects, while the higher energy ions drift westward due to the dominant magnetic field's gradient and curvature drift effects. As a consequence, the ion ring current in the Earth's inner magnetosphere naturally forms positive phase space density (PSD) gradients in the perpendicular velocity distribution [*Thomsen et al.*, 2011]. The positive slopes in PSD distribution are unstable and can cause magnetosonic wave instability when the ion ring energy (E_R) is comparable to the local Alfven energy (E_A) [*Horne et al.*, 2000; *Jordanova et al.*, 2012], where E_R is the proton energy corresponding to the ion ring velocity with a peak in PSD distribution, and E_A is the energy corresponding to the local Alfven velocity which is related to the total plasma density and the background magnetic field strength.

In addition to the theoretical proof about the relation between the magnetosonic waves and the ion ring distributions, the satellite wave and particle measurements have also provided the evidence for their correlations [e.g., *Perraut et al.*, 1982]. Intense magnetosonic waves outside the plasmapause are typically observed simultaneously with positive gradients in the ion PSD distribution [*Meredith et al.*, 2008; *Ma et al.*, 2013]. *Chen et al.* [2010] have coupled the Rice Convection Model (RCM) and the Ring Current-Atmospheric Interactions Model (RAM) to model the ion ring distributions in the Earth's magnetosphere. Using the modeled particle distributions, they have further simulated the global distribution of magnetosonic waves, and found the growth rate dependencies on the wave frequency and the total plasma density. Utilizing the proton ring distributions observed by the Los Alamos National Laboratory (LANL) satellites, *Chen et al.* [2011] have calculated the magnetosonic wave growth rates, and suggested

that the proton ring distributions during the 2001 April storm could excite broad band magnetosonic waves over a broad range of magnetic local time (MLT).

To study the generation of magnetosonic wave in the typical Earth's space environment, in the following Section 4.2 - 4.7, we calculate the magnetosonic wave growth rate under several representative plasma conditions. We combine the THEMIS particle and wave observations, and demonstrate that the observed ion ring distribution can excite magnetosonic waves when E_R is comparable with E_A, in reasonably good agreement with the observed wave frequency spectra. In Section 4.2, we identify a typical magnetosonic wave event and the associated ion ring distribution as observed by THEMIS. In Section 4.3, we present a detailed analysis of the magnetosonic wave instability under different plasma conditions. In Section 4.4, we study the sensitivity of magnetosonic wave growth rate on the assumed wave normal angle. The wave growth rates also depend on the total plasma density, and this dependence is studied in Section 4.5. In Section 4.6, we perform the wave instability analysis for the entire magnetosonic wave event observed by THEMIS using the observed in situ proton distributions. Since broad band magnetosonic waves are also occasionally observed outside the plasmapause, we analysis another magnetosonic wave event using the similar method in Section 4.7. Our analysis covers various conditions for the generation of magnetosonic waves in the Earth's magnetosphere.

4.2 THEMIS observations of the magnetosonic wave event and ion ring distributions

Magnetosonic waves are reported to frequently occur near the equator over a broad MLT region in the Earth's inner magnetosphere [*Santolík et al.*, 2004; *Meredith et al.*, 2008; *Ma et al.*, 2013]. The typical magnetosonic wave events are observed by the satellites in the magnetosphere when they cross the equatorial plane [*San-*

tolík et al., 2002; *Horne et al.*, 2007]. The three THEMIS inner spacecraft (A, D, and E) have nearly equatorial orbits in the Earths magnetosphere [*Angelopoulos*, 2008], and occasionally provide more than 1 h continuous observation of magnetosonic wave events when they pass through the region near the magnetic equator. Relatively narrow and high frequency band magnetosonic wave events are typically observed outside the plasmapause, and the wave frequency spectra varies according to the changing proton gyrofrequency along the trajectory of the spacecraft. Simultaneously, the ion ring distributions in the energy range from several keV to tens of keV are also observed in good correlation with the wave measurements. Magnetosonic waves are highly oblique electromagnetic emissions, with a large ratio between the parallel and perpendicular wave magnetic field components $B_{w\parallel}/B_{w\perp} \ll 1$ and a large ratio between the perpendicular and parallel wave electric field components $E_{w\perp}/E_{w\parallel} \ll 1$. The waves are capable of propagating both radially and azimuthally in the magnetosphere [*Kasahara et al.*, 1994; *Santolík et al.*, 2002; *Chen and Thorne*, 2012].

Figure 4.1 shows a typical magnetosonic wave event in the afternoon sector observed by THEMIS A during 03:00 - 04:00 UT on 24 November 2010. The different panels are presenting (from top to bottom): (a) the total plasma density; (b) ion differential energy flux as a function of energy for a pitch angle of $\sim 90°$; (c) ion PSD as a function of energy for a pitch angle of $\sim 90°$; (d) power spectral density of the wave perpendicular electric field $E_{w\perp}$; (e) wave parallel electric field $E_{w\parallel}$; (f) wave parallel magnetic field $B_{w\parallel}$; and (g) wave perpendicular magnetic field $B_{w\perp}$. The frequencies of f_{LHR} and $0.5f_{LHR}$ are denoted as white dash-dotted and dotted lines in Figure 4.1d - 1g.

The profile of the total plasma density N (Figure 4.1a) is inferred from the Electric Field Instrument (EFI) measurement of spacecraft potential together with the electron thermal speed measured from the Electrostatic Analyzer (ESA) instrument [*Li et al.*, 2010]. The density profile indicates that the spacecraft was

traveling towards the Earth and crossed the plasmapause between $\sim$ 03:30-03:40 UT. The background magnetic field B_0 is measured by the Flux Gate Magnetometer (FGM) [*Auster et al.*, 2008]. The ESA instrument also measures the ion differential energy flux from several eV to 25 keV at different pitch angles [*McFadden et al.*, 2008]. The ion PSD distribution (Figure 4.1c) is calculated from the ion differential energy flux spectra for a pitch angle of $\sim 90°$. To visualize the relative relation between E_R and E_A, the local Alfven energy is shown as the black line in Figure 4.1c. The EFI [*Bonnell et al.*, 2008] and the Search Coil Magnetometer (SCM) [*Roux et al.*, 2008] instruments observe the wave electric (Figure 4.1d - e) and magnetic (Figure 4.1f - g) field respectively. High resolution wave spectra from the fast survey data show the intensification of plasma wave emissions below the lower hybrid resonant frequency f_{LHR} (estimated as 43 f_{cp} in Figure 4.1d - g). Before $\sim$ 03:28 UT, the narrow frequency band oblique whistler mode emissions are characterized by a stronger power in $E_{w\perp}$ than $E_{w\parallel}$, and a stronger power in $B_{w\parallel}$ than $B_{w\perp}$. These waves also follow the varying trend of the lower hybrid frequency f_{LHR}. We identify them as magnetosonic waves outside the plasmapause. Inside the plasmapause, the oblique emissions within a nearly constant frequency band below $\sim$ 150 Hz are also identified as magnetosonic waves. It should be noted that the emissions with nearly constant frequency band above $\sim$ 200 Hz have comparable $B_{w\parallel}$ and $B_{w\perp}$ components, and are therefore identified as plasmaspheric hiss waves.

The proton ring distributions that potentially provide the free energy to excite the waves are observed throughout the entire magnetosonic wave event. The examples of the positive PSD slopes as a function of ion perpendicular energy are shown by the three red arrows in Figure 4.1c. During the period 03:00-04:00 UT, as THEMIS A traveled from the region outside to inside the plasmapause, the positive gradient in the ion PSD as a function of the perpendicular kinetic energy $E_{k\perp}$ is most prominent at around 03:40 UT. In addition to the existence of

the ion ring distribution, the relative ratio between the Alfven energy E_A and the ion ring energy is important for magnetosonic wave excitation. Here the Alfven energy E_A is defined as $E_A = B_0^2/(2\mu_0 N)$, where μ_0 is the vacuum permeability, N is the total plasma density, and B_0 is the background magnetic field intensity; the ion ring energy E_R is defined as the peak energy in the ion ring PSD profile as a function of $E_{k\perp}$. Outside the plasmapause, the local E_A is slightly higher than E_R, with a representative example shown at time 1 (the first dashed vertical line). When the spacecraft was completely inside the plasmapause, E_A is much lower than E_R, as represented at time 3 (the third dashed vertical line). Interestingly, in between these two regions THEMIS A also traveled through a density plateau region where the density slightly increased to $\sim$ 40 cm^{-3}. Around time 2 (the second dashed vertical line), E_A is slightly lower than E_R for $\sim$ 5 min, which is representative for the case near the plasmapause boundary. The following analysis at these 3 different times results in different characteristics of the magnetosonic waves, and these features will be discussed in Section 4.3.

4.3 Magnetosonic instability analysis under typical plasma conditions

Magnetosonic waves in the Earth's magnetosphere are known to be excited by the positive gradients in the ion phase space density (f) distribution as a function of perpendicular energy of the ions [*Horne et al.*, 2000; *Chen et al.*, 2010]. In general, the local convective growth rate K_i can be calculated as the summation of the contributions from the resonant wave particle interactions at different resonant harmonic numbers [*Chen et al.*, 2010]:

$$K_i = \sum_{n=-\infty}^{+\infty} \int_0^{\infty} dv_\perp (W_{n\perp} \frac{\partial f}{\partial v_\perp} + W_{n\parallel} \frac{\partial f}{\partial v_\parallel})|_{v_\parallel = v_{res\parallel}}, \tag{4.1}$$

where n is the harmonic number, $v_\perp$ and $v_\parallel$ are the perpendicular and parallel velocities respectively, and $W_{n\perp}$ and $W_{n\parallel}$ are the perpendicular and parallel weighting functions respectively. Here $v_\parallel$ is evaluated as the resonant velocity $v_{res\parallel}$, which satisfies the following resonant condition:

$$\omega - k_\parallel v_{res\parallel} = n\Omega_{cp}, \tag{4.2}$$

where ω is the magnetosonic wave frequency, Ω_{cp} is the proton gyrofrequency, and $k_\parallel$ is the parallel wave number.

For highly oblique magnetosonic waves with wave normal angles generally greater than 89°, $k_\parallel$ is small, so $v_{res\parallel}$ becomes small only when $\omega \sim n\Omega_{cp}$, especially for low harmonic resonances. Therefore, the wave growth rates peak at frequencies close to the harmonics of local proton gyrofrequency f_{cp}. Using the cold plasma dispersion relation for perpendicularly propagating magnetosonic waves, the wave phase speed ω/k can be approximated as the Alfven velocity v_A, except for frequencies near the local hybrid resonance frequency f_{LHR}. This is especially true at low harmonic frequencies. Therefore, v_A is an important factor in controlling the wave growth rate and the unstable wave frequency band.

THEMIS instruments provide the ion differential energy flux data and the background plasma condition information, which are key parameters in calculating the magnetosonic wave growth rate during the real-time observed event. Figure 4.2 shows the magnetosonic wave instability analysis at the 3 representative times as indicated by the magenta vertical lines in Figure 4.1. The different panels in Figure 4.2 present ion PSD 2D distribution as a function of perpendicular ($E_{k\perp}$) and parallel ($E_{k\parallel}$) kinetic energy (panels a, d, g), ion PSD at a pitch angle of $\sim 90°$ (panels b, e, h) as a function of perpendicular energy, and the resultant magnetosonic wave growth rate in comparison with the observed wave intensity as a function of normalized wave frequency f/f_{cp} (panels c, f, i), respectively. The ion PSD at pitch angles from $\sim 0°$ to $\sim 90°$ and energies from $\sim$ 10 eV to

$\sim$ 21 keV are measured from the ESA instrument. The ion ring distributions are clearly seen at around 12.3 keV at time 1 and time 2, and around 16.2 keV at time 3, indicating the injection of ions from the plasma sheet to inside the plasmasphere. However, as shown in Figure 4.1c, due to the varying background plasma density N and magnetic field strength B_0, the value of E_A is $\sim$ 24.2 keV at time 1, $\sim$ 7.47 keV at time 2, and $\sim$ 0.43 keV at time 3. The positive gradients in the energy range of 1 - 20 keV are considered to be potentially responsible for exciting magnetosonic waves, and the positive gradients out of this range may provide little contribution to wave excitation in the Earth's inner magnetosphere environment.

The local magnetosonic wave convective growth rates K_i are calculated in the normalized frequency range from Ω_{cp} to $50\Omega_{cp}$ with a frequency resolution of $0.1\Omega_{cp}$. The frequency grids are shifted away from $n\Omega_{cp}$ by $0.05\Omega_{cp}$ to avoid the singularities occurring at wave normal angles extremely close to 90° because of requirement of finite $k_{\|}$ in the growth rate formula. The total contributions from resonant harmonics in the n range from -10 to 60 are calculated to evaluate the convective growth rates as a function of the normalized wave frequency. The wave growth rates are calculated at wave normal angles from 89.1° to 89.9° with a step of 0.1° at time 1, and from 88.2° to 89.8° with a step of 0.2° at time 2 and time 3, based on the sensitivity on wave normal angles which will be discussed in Section 4.4. The maximum wave growth rate over all wave normal angles at each frequency is subsequently chosen as the resultant local convective growth rate of magnetosonic waves in the simulation.

The comparisons between the simulated magnetosonic wave growth rate (blue) and the observed wave intensity (black) are shown in the lower panels in Figure 4.2. The simulated magnetosonic waves occur at higher normalized frequencies at time 1, consistent with the observations. The frequency band of the simulated wave is located towards the higher end of the observed wave frequency band, and this

feature will be discussed in Section 4.5. At time 2, magnetosonic waves in lower and broader normalized frequency band are excited from the simulation, with fairly good agreement with the observations. Although the ion ring distribution is most prominent at time 3, the calculated wave growth is too small compared to the observed magnetosonic waves below $\sim 25 f_{cp}$. Our simulation suggests that wave propagation from a distant source is needed to explain the presence of the magnetosonic waves inside the plasmapause during this event, and in Chapter 5 we will perform the propagation analysis on a similar magnetosonic wave event to confirm our hypothesis. The observed wave profile above $\sim 30 f_{cp}$ are confirmed to be plasmaspheric hiss emissions, which are well separated from the magnetosonic waves in the lower frequency band.

4.4 Wave normal angle dependence of magnetosonic wave instabilities

Magnetosonic waves are excited at highly oblique directions with wave normal angles larger than $\sim 88.0°$. Figure 4.3 shows the wave normal dependence of magnetosonic wave instabilities at time 1 (left panel) and time 2 (right panel). The wave local growth rates are calculated as a function of normalized wave frequencies and the wave normal angle. Based on the major difference in background plasma densities, the wave growth rates are shown at wave frequencies between $25\omega/\Omega_{cp}$ and $50\omega/\Omega_{cp}$ at time 1 and between $0\omega/\Omega_{cp}$ and $50\omega/\Omega_{cp}$ at time 2, and wave normal angles between 89.0° and 90.0° at time 1 and between 88.0° and 90.0° at time 2.

Although the wave growth rate is sensitive to the wave normal angle, the frequency band of the major wave growth is relatively insensitive over a range of wave normal angles. Consistent with the observed frequency spectra of the waves, our modeling shows positive growth rates at higher harmonic frequencies within

a narrower frequency band at time 1, and at lower harmonic frequencies over a broader frequency band at time 2. The waves appear to be more oblique outside the plasmapause (time 1) than in the density plateau region (time 2), but the small difference is within the observational uncertainty given that the low frequency geophysical noise is present in the ambient magnetic field. The major peak of the wave normal angle feature shifts towards the higher normalized frequency band as the wave normal angle increases, indicating that the wave normal angles of the locally excited magnetosonic waves are higher at higher normalized wave frequencies. In the following simulations, we will calculate the wave growth rates for wave normal angles from 89° to 90° outside the plasmapause and from 88° to 90° inside the plasmapause, at normalized wave frequencies from ω/Ω_{cp} to $60\omega/\Omega_{cp}$, which fully covers the regime of possible wave growths. Therefore, the wave growth rates in our simulation presents the possible highest wave growth under the observed background plasma conditions.

4.5 Total plasma density dependence of magnetosonic wave instabilities

As discussed in Section 4.3, compared to the fairly good agreement between the observation and simulation at time 2 in Figure 4.2f, at time 1 the calculated wave frequency band in Figure 4.2c is located in the higher end of the observed wave frequency band. We also note that the total plasma density of $\sim 10cm^{-3}$ was used to calculate wave growth rates at time 1, while the total plasma density is higher than $\sim 100cm^{-3}$ at time 2. However, there can be a factor of two uncertainty in the total plasma density inferred from the spacecraft potential especially outside the plasmapause, according to the analysis by *Li et al.* [2010]. Therefore, we calculate the wave growth rates by varying the plasma density for a sensitivity study about the wave growth rates on the total plasma densities.

Figure 4.4 shows the comparison between the calculated magnetosonic wave growth rates (blue) and the observed magnetosonic wave frequency spectra (black) outside the plasmapause (time 1, top) and near the plasmapause boundary (time 2, bottom). The wave growth rates and wave intensities are presented as a function of normalized wave frequency. We have varied the total plasma density as $0.667N$, N, and $1.5N$ to study the role of density in the excited wave frequency spectra, where N is the total plasma density inferred from the spacecraft potential. Generally, the calculated peak wave growth rates shift to lower (higher) normalized frequencies, when the higher (lower) density is used, consistent with *Chen et al.* [2010]. The density value also affects the strength of wave growth as it changes the ratio between E_R and E_A. The strength of wave growth tends to be larger when E_R approaches close to E_A by varying the density. Our sensitivity test shows that the best agreement with the observation is obtained when the density outside the plasmapause (time 1) is increased by a factor of 1.5. However, the simulation result is fairly good at time 2 when using the nominal inferred density data from the spacecraft potential. Figure 4.4 confirms that the observed magnetosonic wave frequency spectra are resultant of the background plasma conditions as observed by THEMIS.

4.6 Simulation of magnetosonic wave instabilities across the plasmapause boundary

We will perform a simulation of the magnetosonic wave event as observed by THEMIS in this section. Simulation of the entire magnetosonic wave event is feasible using the ion flux measurements from the ESA instrument and the simultaneous fast survey wave spectra recorded by the SCM instrument aboard THEMIS. The 3 times discussed in section 3 show representative excitation mechanisms in typical regions with different E_R/E_A ratios. The simulation for the

entire sequence of the magnetosonic wave event is shown in Figure 4.5. The panels in Figure 4.5 presents THEMIS observation of total plasma density, ion PSD as a function of perpendicular energy, power spectral density of $B_{\parallel}$ and $B_{\perp}$, and the simulated local wave growth rate from our local instability analysis.

The excited magnetosonic wave growth rates have similar trends as the observed intensity spectrum from $\sim$ 03:00 UT to $\sim$ 03:40 UT. When E_R is comparable to E_A, the local wave growth can account for the presence of both narrow band magnetosonic waves with frequencies varying with f_{LHR} and broad-band magnetosonic waves near the plasmapause boundary. The modulation of the excited magnetosonic wave profile with varying density is also clear when the density fluctuates during $\sim$ 03:30-03:40 UT. However, the proton ring distribution inside the plasmapause after $\sim$ 03:40 UT cannot provide sufficient free energy for the observed local magnetosonic waves. The fact that the frequency band of waves inside the plasmapause does not follow the local f_{LHR} and the intensity of magnetosonic waves becomes weaker away from the plasmapause suggests that these magnetosonic waves may have propagated into the plasmasphere from a source region at or near the density fluctuating region near the plasmapause. The comparison between observed magnetosonic wave spectra (Figure 4.5c) and the simulated wave growth rates (Figure 4,5e) clearly illustrates the energy source of magnetosonic waves.

4.7 Simulation of broad band magnetosonic wave instabilities

In addition to the narrow band magnetosonic waves outside the plasmapause, magnetosonic wave events within a broad frequency band away from the plasmapause boundary are also occasionally observed by THEMIS. However, it is unclear whether these broad-band features are caused by the local excitation mechanism

or by propagation effects. Using the same method as described above, we will simulate another typical broad frequency band magnetosonic wave event in this section.

Figure 4.6 presents the comparison of the simulated wave growth rate spectrum and the observed broad band magnetosonic wave spectrum on 19 October 2011. In a similar format with Figure 4.5, the different panels shows the THEMIS observations of total plasma density, differential ion energy flux, energy spectrum of ion PSD, power spectral density of $B_{\parallel}$ and $B_{\perp}$, and the simulated wave growth rate from our local instability analysis.

The magnetosonic waves are observed outside the plasmapause and become weaker after the spacecraft enters the plasmasphere. Throughout this wave event, an ion ring distribution with E_R between a few keV and 10 keV is clearly evident in the ion spectra. The positive gradients which are potentially capable of providing free energy for magnetosnic wave excitation are indicated by the red arrows in Figure 4.6c. E_A (black line) is slightly lower than E_R outside the plasmapause. Broad band strong wave growth is expected based on the simulation with remarkable agreement with the observed $B_{\parallel}$ power spectrum. When the density increases to above $100cm^{-3}$ after $\sim$ 10:04 UT, E_A drops to an order of magnitude below E_R, and much weaker magnetosonic waves are excited over a slightly lower frequency band. When the density increases even more inside the plasmasphere after $\sim$ 10:30 UT, there is little wave growth. Similar to the magnetosonic event on 24 November 2010, the weaker magnetosonic waves observed inside the plasmapause may come from a source in the outer unstable region. After being locally excited by the ion ring distribution outside the plasmapause, the broad band magnetosonic waves could propagate radially into the plasmasphere in the magnetic equatorial plane as suggested by *Chen and Thorne* [2012] and *Xiao et al.* [2012]. Outside the plasmapause, our simulation suggests that the broad band magnetosonic waves are mainly locally excited.

4.8 Discussions and Conclusions

This chapter mainly addresses the local excitation scenario of magnetosonic waves under typical plasma conditions in the inner magnetosphere. We analyzed the magnetosonic wave instability using simultaneously observed wave and proton distributions from THEMIS and modeled the wave linear growth rates. Our modeling provides a reasonable explanation of the excited wave frequency spectra based on the observed proton distributions and identifies the spatial regions potentially unstable to excite magnetosonic waves.

The main conclusions are summarized as follows: (1) the ion ring distributions observed simultaneously with the magnetosonic wave emissions exhibit unstable positive slopes in phase space density, which can potentially provide the free energy to excite magnetosonic waves; (2) higher frequency, narrower bandwidth magnetosonic waves are excited in a broad spatial region outside the plasmapause where E_A is slightly higher than E_R; whereas (3) lower frequency and wider bandwidth magnetosonic waves are excited near the plasmapause boundary if E_A becomes slightly lower than E_R; (4) magnetosnic waves observed inside the plasmasphere, where E_A is much lower than E_R, are likely to propagate from a source in the unstable wave regions just outside the plasmasphere; (5) magnetosonic waves are excited at highly oblique wave normal angles (higher than 88°), and the unstable frequency band is dependent on the wave normal angle; (6) the magnetosonic wave growth rate and unstable wave frequency band are dependent on the plasma density, due to the dependence on the ratio E_A/E_R; (7) both narrow and broad frequency band magnetosonic waves outside the plasmapause are mainly due to local excitation under different background plasma conditions; (8) the simulation of magnetosonic instability due to the ion ring distributions with E_R between 1 keV and $\sim$ 20 keV agrees well with the frequency spectra of the observed magnetosonic wave events in the afternoon sector outside the plasmapause, demonstrating that

those ion ring distributions are responsible for the wave generation.

In order to obtain the full ion ring distribution, in the analyzed events above we have limited the ion ring energy to less than 20 keV, which is near the upper energy limit of the ESA instrument. Beyond that the SST instrument can measure proton distributions but requires special processing in order to remove sun contamination and background (penetrating) electrons. As shown in Figure 4.1c and Figure 4.6c, E_R can reach close to $\sim$ 20 keV for the ion ring events in the afternoon sectors. However, higher energy ions can drift to earlier magnetic local times [*Lyons and Williams*, 1984; *Thomsen et al.*, 2011], therefore E_R may become higher than 20 keV in the morning sectors. The statistical study of positive slopes in PSD distribution by *Thomsen et al.* [2011] has shown that, although E_R values are infrequent above 24 keV at geosynchronous orbit, they tend to become most probable in the 06-13 MLT range. It will be therefore interesting to investigate the magnetosonic instability near the dawnside where magnetosonic waves are reported to be strong [*Ma et al.*, 2013], with the ion flux observations at higher energies. Our simulation result implies that the observed magnetosonic waves near the dawnside are also probably caused by similar mixture of local excitation mechanisms and propagation effects. Since our study has directly demonstrated a close relation between the ion ring distribution and the excited magnetosonic wave, it will be interesting to study statistically both the global distribution of the ion ring that can potentially excite magnetosonic waves, and the magnetosonic waves themselves from multiple THEMIS and Van Allen Probes satellites. It will also be interesting to compare statistically the global distribution of the magnetosonic growth rate with the observed magnetosonic waves to verify the relative importance of propagation and local instability in the observed waves. These studies will be left for the future work of interest, and will contribute to better understanding of the dynamic relation between the plasma waves and particle distribution in the Earth's inner magnetosphere.

As discussed in both magnetosonic wave events in this chapter, the local excitation mechanism cannot provide explanation for the observed magnetosonic waves when E_A becomes much lower than E_R in high density regions, especially deep in the plasmasphere. However, the magnetosonic waves with noticeable wave amplitude are occasionally observed in the plasmasphere regardless of the high densities. The waves tend to present a broad and nearly constant frequency spectra with highest intensity near the plasmapause boundary, suggesting a potential source near the boundary and further propagation effects in the plasmasphere. Therefore, we will investigate the capability of wave propagation in the plasmasphere in the next chapter.

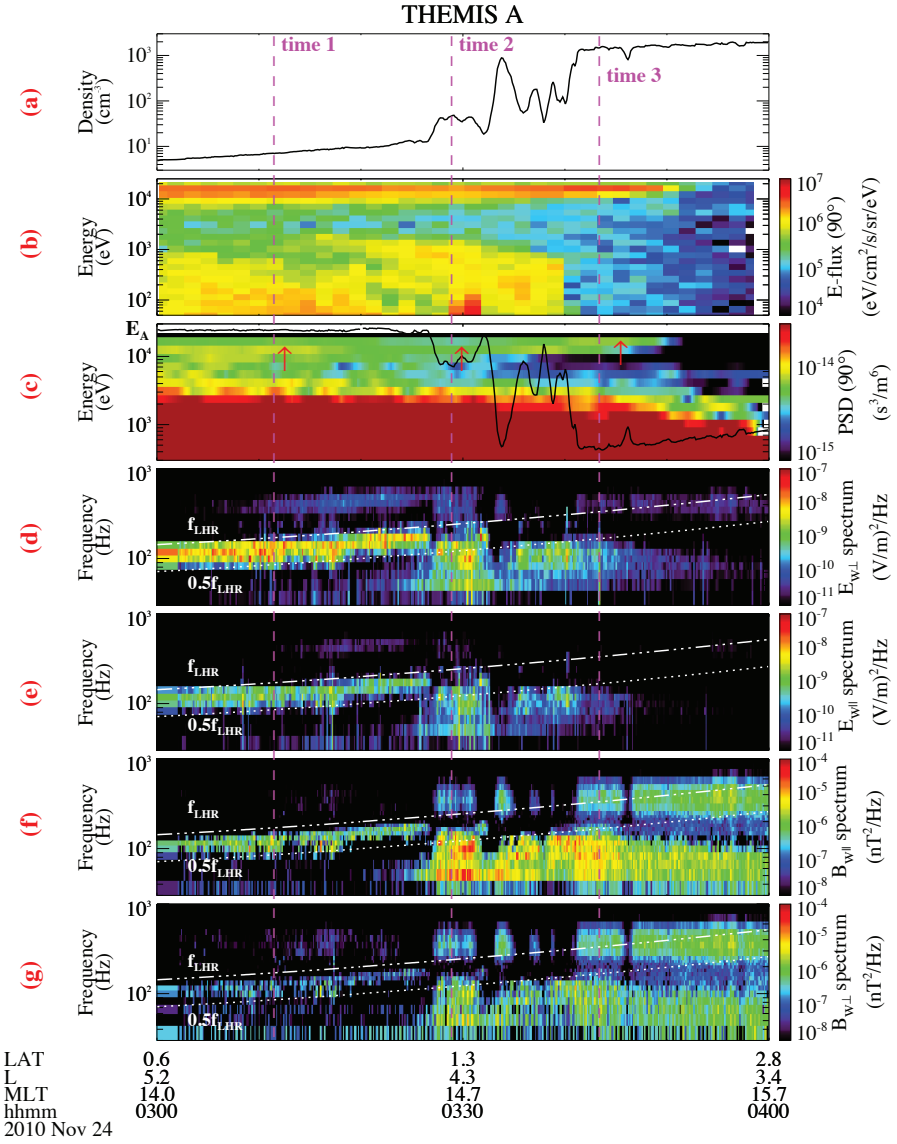

Figure 4.1: Magnetosonic waves observed by THEMIS A on 24 November 2010. (a) The total plasma density; (b) ion differential energy flux at a pitch angle of 90°; (c) ion PSD; (d) power spectral density of $E_{w\perp}$; (e) $E_{w\parallel}$; (f) $B_{w\parallel}$; and (g) $B_{w\perp}$ from wave spectra data. The 3 selected typical times are indicated by the vertical dashed lines. The red arrows in panel (c) indicate 3 examples of the positive gradients in ion PSD.

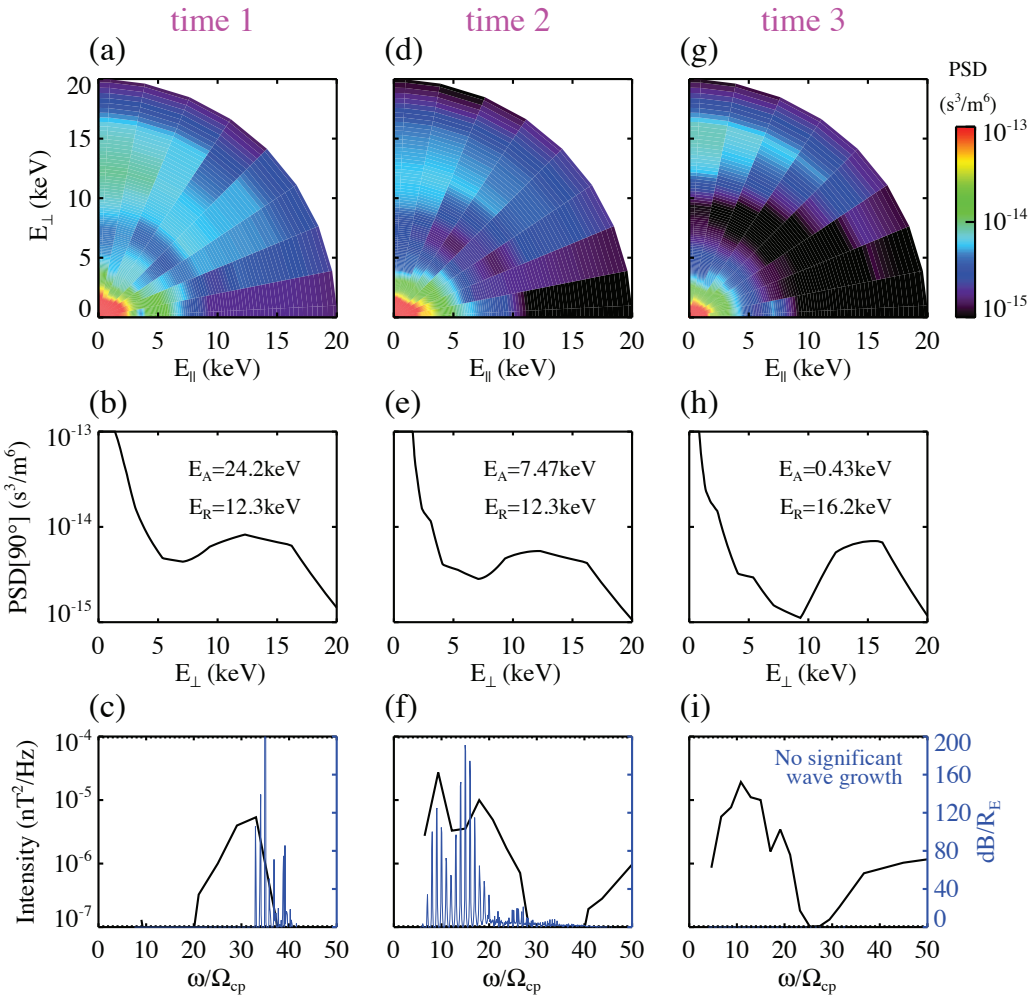

Figure 4.2: The observed ion PSD distributions in the parallel and perpendicular energy space (first row), the ion PSD at a pitch angle of 90° as a function of $E_\perp$ (second row), and the comparisons (third row) of the observed wave intensity (black) with the simulated wave growth rate (blue) as a function of normalized wave frequency. The analyses are performed at time 1 (first column), time 2 (second column), and time 3 (third column), respectively.

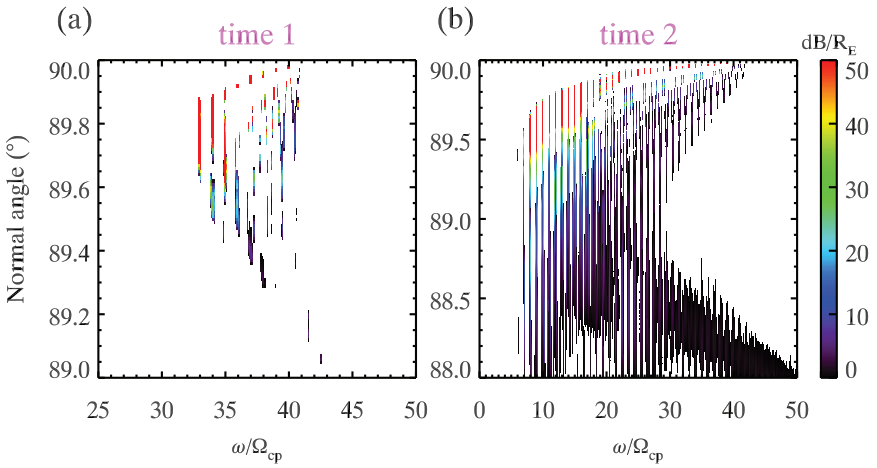

Figure 4.3: Magnetosonic wave growth rates (color-coded) as a function of normalized wave frequency and wave normal angle at time 1 (panel a) and time 2 (panel b). The white area represents the region without wave growth ($\gamma \leq 0$). Note that based on the relative values of E_R and E_A, the frequency of wave growth is different in the two regions. The frequency scale in the horizontal axis is also different in the two panels, adjusted accordingly. Also note that the wave normal angle scales are also different: they are wider on the right, consistent with the broader range of unstable wave normal angles.

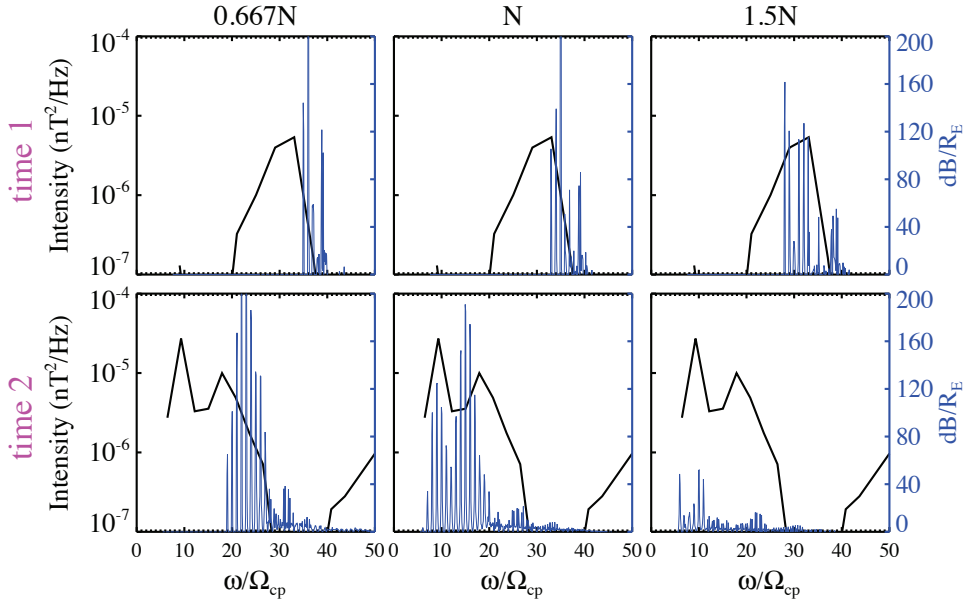

Figure 4.4: Simulation of magnetosonic wave growth rates (blue) with different plasma densities of $0.667N$ (first column), N (second column), and $1.5N$ (third column) at time 1 (row 1) and time 2 (row 2), where N is the total plasma density inferred from the spacecraft potential. The observed wave intensity is indicated with a black line in each panel.

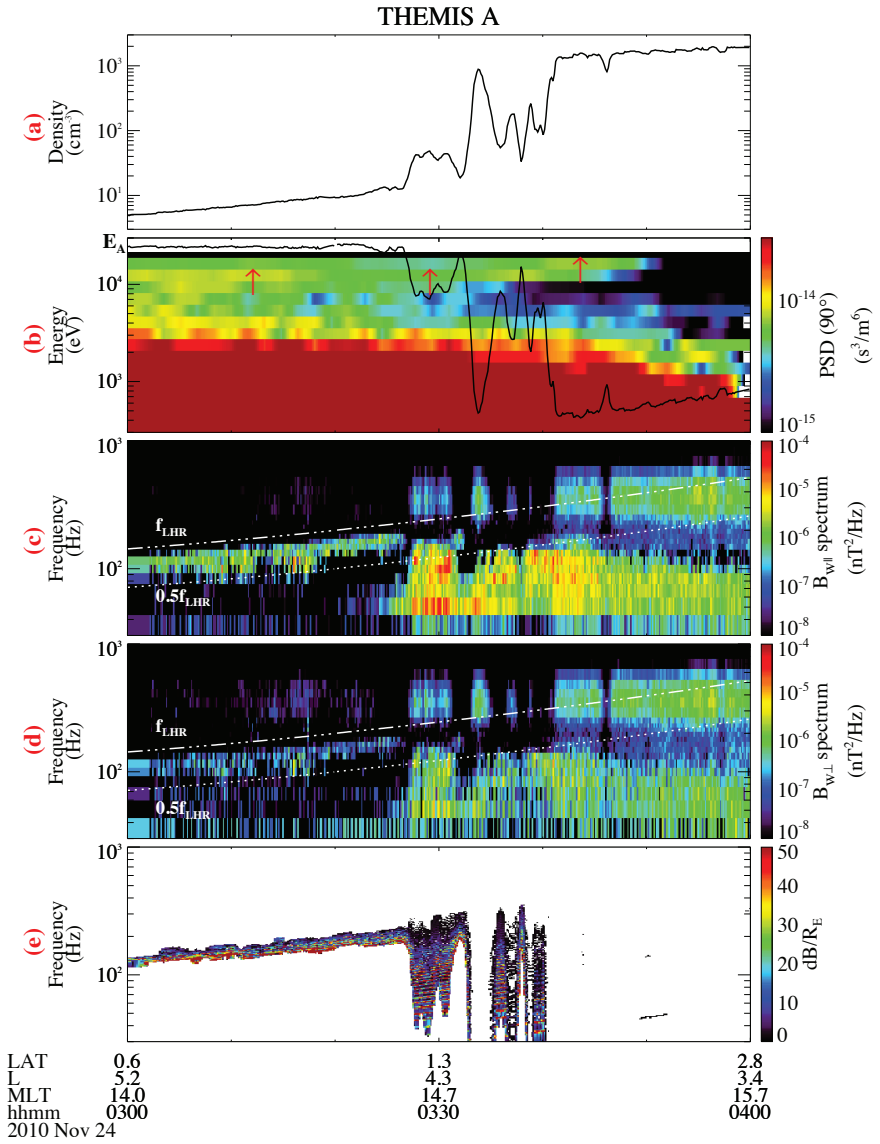

Figure 4.5: Comparison of the simulated wave growth rate spectrum and the observed magnetosonic wave spectrum on 24 November 2010. (a) Total plasma density; (b) ion PSD as a function of energy for a pitch angle of $\sim 90°$; (c) power spectral density of $B_{\|}$; (d) $B_{\perp}$; (e) simulated local wave growth rate. The other notions are the same as in Figure 1. The white area in (e) represents the region without significant wave growth (less than 0.5 dB/R_E).

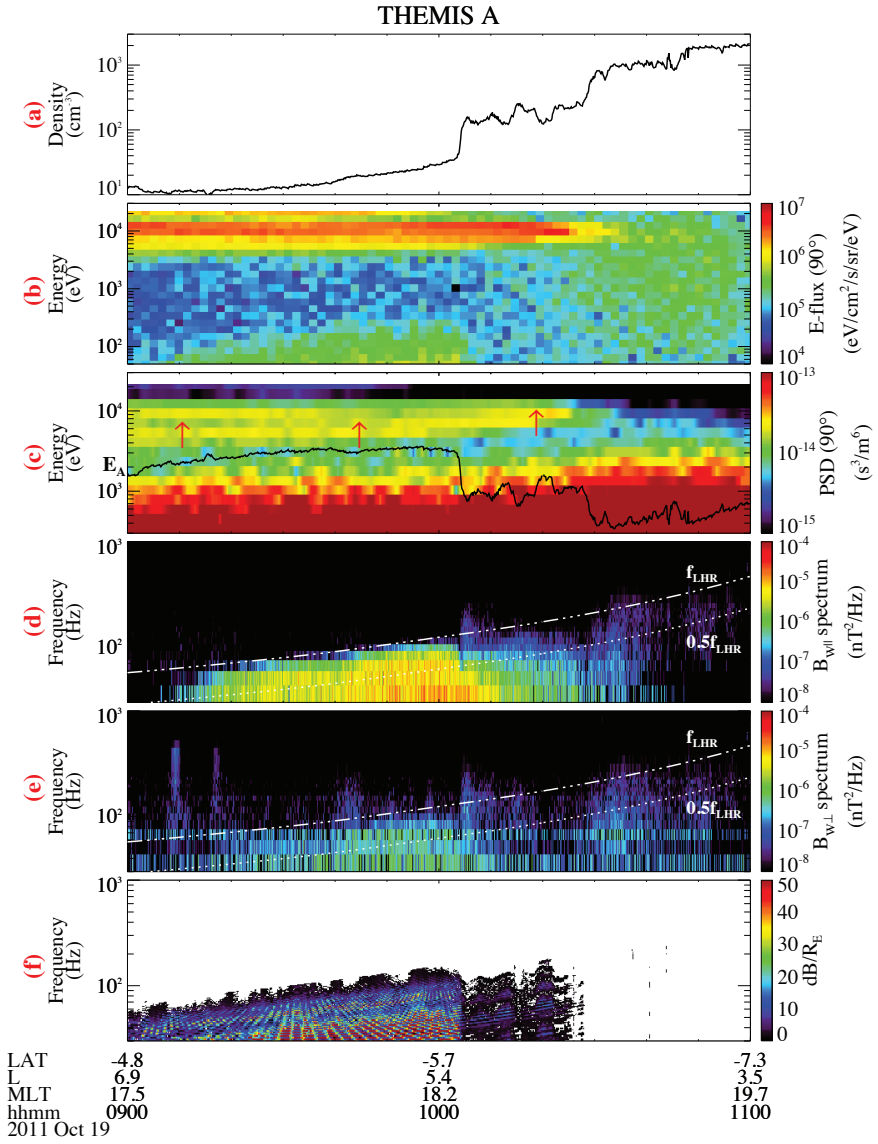

Figure 4.6: Comparison of the simulated wave growth rate spectrum and the observed broad band magnetosonic wave spectrum on 19 October 2011. (a) Total plasma density; (b) differential ion energy flux for a pitch angle of $\sim 90°$; (c) energy spectrum of ion PSD for a pitch angle of $\sim 90°$; (d) power spectral density of $B_{\|}$; (e) $B_{\perp}$; (f) simulated local wave growth rate. The other notions are the same as in Figure 1. The white area in (f) represents the region without significant wave growth (less than 0.5 dB/R_E).

CHAPTER 5

Propagation of magnetosonic waves in the outer plasmasphere

Besides the local excitation by ion ring distributions, the global distribution of magnetosonic waves is also determined by the trace of the emissions from their energy source. As discussed in Chapter 4, equatorial magnetosonic waves are typically excited outside the plasmapause or near the plasmapause boundary. However, the waves are also observed in a widely extended region in the plasmasphere as shown in Chapter 3. The full understanding of the existence of magnetosonic waves requires further study about the propagation effects in the plasmasphere, which is the objective of this chapter.

In this chapter, we investigate the excitation and propagation of equatorial magnetosonic waves observed by the Van Allen Probes, and describe evidence for a trapping mechanism for magnetosonic waves in the Earth's plasmasphere. The recent Van Allen Probes mission provides excellent observation of plasma waves and particle distributions in the inner magnetosphere. Intense equatorial magnetosonic waves were observed inside the plasmasphere in association with a pronounced proton ring distribution, which provides free energy for wave excitation. Instability analysis along the inbound orbit demonstrates that broad-band magnetosonic waves can be excited over a localized spatial region near the plasmapause. The waves can subsequently propagate into the inner plasmasphere and remain trapped over a limited radial extent, consistent with the predictions of near-perpendicular propagation. By performing a similar analysis on another ob-

served magnetosonic wave event, we demonstrate that magnetosonic waves can also be trapped within local density structures. We suggest that perpendicular wave propagation is important for explaining the presence of magnetosonic waves in the Earth's plasmasphere at locations away from the generation region.

This chapter is organized as the following: Section 5.1 provides a brief introduction about the equatorial magnetosonic waves in the Earth's inner magnetosphere, and we will mainly focus on summarizing the previous studies about the propagation of the waves near the equatorial plane; Section 5.2 provides a simplified illustration of the magnetosonic wave propagation, and demonstrates the existence of a potential trapping region of the equatorial magnetosonic waves in the plasmasphere; Section 5.3 presents an intense magnetosonic wave event observed by the Van Allen Probes in the plasmasphere, and shows that the observed ion ring distributions could provide the excitation of magnetosonic waves near the plasmapause boundary; using the wave trapping theory, the possible trapping region is simulated in Section 5.4, which demonstrates that the observed wave spectra are resultant of the wave trapping in the plasmasphere; satellite observation occasionally shows that magnetosonic waves are modulated by the density structures in the plasmasphere, and Section 5.5 proves that the waves can be trapped and therefore constrained within a local density enhancement region; we summarize our results in Section 5.6 and illustrate the magnetosonic wave excitation and propagation scenario in the outer plasmapshere.

5.1 Introduction

Equatorial magnetosonic waves are oblique whistler-mode electromagnetic emissions between the proton gyrofrequency and the lower hybrid resonant frequency [e.g., *Perraut et al.*, 1982; *Laakso et al.*, 1990; *Santolík et al.*, 2004]. The waves are typically observed near the Earth's magnetic equator [e.g., *Russell et al.*,

1970; *Gurnett*, 1976; *Santolík et al.*, 2002], and may have potentially important effects in particle scattering in the radiation belts [e.g., *Horne et al.*, 2007; *Bortnik and Thorne*, 2010; *Mourenas et al.*, 2013; *Xiao et al.*, 2014]. Recent spacecraft missions in the Earth's magnetosphere have provided excellent coverage for investigating magnetosonic wave spectral properties, spatial distributions, and their dependencies on the local plasma conditions [*Santolík et al.*, 2004; *Meredith et al.*, 2008; *Ma et al.*, 2013]. Magnetosonic waves in the Earth's inner magnetosphere are excited by positive phase space density (PSD) slopes in the ion ring distribution over the energy range from $\sim$ 1 keV to $\sim$ 30 keV [*Perraut et al.*, 1982; *Horne et al.*, 2000; *Thomsen et al.*, 2011; *Chen et al.*, 2011; *Liu et al.*, 2011; *Xiao et al.*, 2013], and the unstable frequency spectra and local wave growth rates are modulated by the relative ratio between the local Alfven energy (E_A) and ion ring energy (E_R) [*Boardsen et al.*, 1992; *Chen et al.*, 2010].

The global surveys of magnetisonic waves have shown that magnetosonic waves have higher occurrence rates outside the plasmapause than inside the plasmapause, due to their strong dependence on the presence of ion ring distributions [*Meredith et al.*, 2008; *Ma et al.*, 2013]. With simultaneous observations of ion ring distributions with E_R close to E_A, magnetosonic waves outside the plasmapause can generally be explained by a local excitation mechanism [e.g., *Ma et al.*, 2014a]. However, the local excitation mechanism cannot explain the presence of magnetosonic waves deep inside the plasmapause where E_A becomes much less than E_R and the conditions for local generation of magnetosonic waves are typically not satisfied [*Chen et al.*, 2010; *Ma et al.*, 2014a]. Nonetheless, magnetosonic waves are observed over a wide range of L-shells inside the plasmasphere, and their distributions are more uniform inside the plasmapause than outside the plasmapause [*Meredith et al.*, 2008; *Ma et al.*, 2013]. The magnetic power intensities of magnetosonic waves are also observed to exist at frequencies off the whole harmonics of the local proton gyrofrequency, indicating that magnetosonic waves can

propagate both radially and azimuthally [*Santolík et al.*, 2002]. In addition, the equatorial contineous observation of magnetosonic waves inside the plasmapause typically presents a nearly constant wave frequency band, which is a character of wave propagation perpendicular to the background magnetic field. Consequently, it is necessary to incorporate propagation effects together with the local excitation mechanism to reconstruct the observed magnetosonic wave events inside the plasmapause as presented in the subsequent sections.

The analysis by *Chen and Thorne* [2012] has shown the wave propagation effects under different circumstances. Outside the plasmapause, the magnetosonic waves propagate in the equatorial plane and are refracted before reaching the plasmapause boundary; however, inside the plasmapause, magnetosonic waves within a wide range of azimuthally propagating angles may become trapped between the outer edge of the plasmapause and deep in the plasmasphere; only a small portion of the magnetosonic waves with wave azimuthal angle pointing nearly radially can penetrate through the plasmapause and propagate inward into the plasmasphere or outward into the plasmatrough. When the waves are trapped in the plasmasphere, they obtain extended periods of energy gains if the ion ring distribution is present. Therefore, wave trapping inside the plasmapause is an important factor for explaining the existence of the waves. A simplified illustration of this effect in the plasmasphere will be further discussed in Section 5.2.

Using the Van Allen Probes wave and particle measurements, we will perform a combined wave excitation and propagation analysis on two magnetosonic wave events, and directly demonstrate that magnetosonic waves can be excited near the plasmapause and subsequently be trapped inside the plasmasphere or within local density structures. Our study indicates the importance of wave propagation in understanding the magnetosonic wave distribution in the plasmasphere.

5.2 Perpendicular propagation of magnetosonic waves

The magnetosonic waves are highly oblique electromagnetic emissions narrowly confined near the Earth's magnetic equator, and therefore the trace of the waves can be approximated as propagating perpendicular to the background magnetic field in the equatorial plane in the Earth's inner magnetosphere. This simplifies the ray-tracing technique into a 2-D problem, i.e., the solve of the wave path in L-MLT regime. In the analysis in this section, we further assume that the Earth's magnetic field to be a dipole field, and the plasma density in the plasmasphere obeys Sheeley's density model [*Sheeley et al.*, 2001] which only depends on L-shell. Therefore, the background plasma condition is azimuthally symmetric around the Earth.

When the plasma waves propagate through two different refractive media, the wave frequency and the component of wave vector parallel to the interface of the two media are conserved. As a consequence, the trajectory of the waves obey Snell's law which describes the relation between the direction of the incoming wave trace and the direction of the outgoing wave trace. In polar coordinates, the Snell's law is expressed as:

$$n_1 L_1 \sin\psi_1 = n_2 L_2 \sin\psi_2, \tag{5.1}$$

where subscripts '1' and '2' denote the refractive medium on different sides, n is the refractive index, ψ is the wave azimuthal angle in the equatorial plane, which is defined as 0° when pointing outward and 90° when pointing eastward.

Equivalently, Snell's law implies that the quantity Q is conserved when the magnetosonic wave propagates through the continuously varying media in the Earth's magnetosphere:

$$Q = nL \sin\psi. \tag{5.2}$$

Consequently, the wave azimuthal angle varies as the wave propagate across different L-shells. The trajectory of the equatorial magnetosonic waves can be obtained using the conservation of Q.

We use a simplified Earth's plasmasphere model to illustrate the path of the waves in the plasmasphere. We use Sheeley's plasma density model in the plasmasphere to model the total plasma density at $L \leq 4.4$, and Sheeley's plasma density model in the plasmatrough to model the total plasma density at $L \geq 4.6$; the plasma density linearly decreases from 219 cm^{-3} to 22.4 cm^{-3} as L increases from 4.4 to 4.6. A source of magnetosonic waves at a constant frequency of 60 Hz is assumed to be located at $L = 4.5$, and the waves may propagate radially and azimuthally in the equatorial plane.

Figure 5.1 presents the total plamsma density, refractive index, and the Q value with azimuthal angle equal to 90° as a function of L-shell. A plasmapause boundary is defined around $L = 4.5$. The refractive index generally increases as L-shell increases but decreases significantly near the plasmapause due to the decrease in total plasma density. n increases to infinity around $L = 7$ when the local lower hybrid resonance frequency approaches the wave frequency. The $Q(\psi = 90°)$ profile presents a maximum value near the plasmapause boundary. When the waves propagate in the equatorial plane, the Q value is conserved, and the wave azimuthal angle reaches 90° when the ray reaches the $Q(\psi = 90°)$ profile. Subsequently, the waves are refracted backward and trapped in the limited region in the plasmasphere. The dashed line in the bottom panel in Figure 5.1 therefore indicates a potential trapping region.

Figure 5.2 clearly illustrates the wave path in the plasmasphere. At initial point located at L = 4.5, the magnetosonic waves with initial azimuthal angles of 30° (red) and 60° (blue) are launched inside the plasmapause. The top panel of Figure 5.2 shows the variation of wave azimuthal angle as a function of L-shell. Clearly, when the waves propagate away from the Earth, the azimuthal angle

reaches 90° quickly due to the density drop; when the waves propagate towards the Earth, the azimuthal angle also reaches 90° as the refractive index and L decrease. Waves with smaller azimuthal angle extend into a wider region in L shells, yet waves within a large range of azimuthal angles are well trapped in the plasmasphere. The bottom panel of Figure 5.2 presents the trajectory of the trapped magnetosonic waves in the equatorial plane. The waves bounce in a limited radial region in the outer plasmasphere near the magnetic equator. In addition, the ion ring distribution that potentially amplify the wave amplitude of magnetosonic waves may be present in a wide MLT region near the plasmapause boundary, and the trapped magnetosonic waves may obtain energy gain in a prolonged period and extended area.

We will use this technique to study the potential trapping of equatorial magnetosonic waves observed by the Van Allen Probes. However, it's not practical to exactly obtain the initial wave azimuthal angle and the location of the wave source. Without those information, the calculation of $Q(\psi = 90°)$ profile, which only depends on the radial profile of background magnetic field and total plasma density, still provides the predictions about the potential trapping region of magnetosonic waves as shown in Figure 5.1. The utilization of this method for the real-time observation of magnetosonic waves will be shown in the following sections.

5.3 Intense magnetosonic waves observed by the Van Allen probes

The Van Allen Probes are two identical spacecraft (Probe A and B) in nearly equatorial orbits with a perigee $\sim 1.1\ R_E$ and an apogee $\sim 5.9\ R_E$ [*Mauk et al.*, 2013]. Designed for the scientific study about the Earth's inner magnetosphere and the radiation belts, the Van Allen Probes provide high-resolution particle and wave measurements in the Earth's inner magnetosphere. The Energetic Particle

Composition and Thermal Plasma Suite (ECT) [*Spence et al.*, 2013] measures the radiation belt electron and ion spectra with sufficient energy and pitch angle coverage, and the Helium Oxygen Proton Electron (HOPE) instrument [*Funsten et al.*, 2013] covers the particle energy range from $\sim$ 1 eV to $\sim$ 50 keV. The Electric and Magnetic Field Instrument Suite and Integrated Science (EMFISIS) [*Kletzing et al.*, 2013] measures the DC magnetic field and the wave electric and magnetic fields using the magnetometer and the Waves instrument, respectively. The Waveform Receiver (WFR) of the Waves instrument measures wave spectra from 10 Hz to 12 kHz for all the three components of both electric field and magnetic field. The WFR not only measures wave power spectral density but also provides wave polarization properties including wave normal angle, azimuthal angle, and ellipticity, calculated by the Singular Value Decomposition (SVD) method [*Means*, 1972; *Santolík et al.*, 2003]. The High Frequency Receiver (HFR) of the Waves instrument measures the electric field spectra density from 10 kHz to 400 kHz [*Kletzing et al.*, 2013], which covers the upper hybrid resonance frequency f_{UHR} range in the inner magnetosphere and can therefore be used to infer the total plasma density in the Earth's radiation belts.

Figure 5.3 presents the intense magnetosonic wave and ion ring event observed by Van Allen Probe A during 09:30 – 12:00 UT on 04 December 2012. The different panels presents: (a) the electric field power spectral density in the Waves HFR channel; (b) proton PSD as a function of energy for a pitch angle of $\sim 90^\circ$ measured by the HOPE instrument; (c) magnetic field power spectral density in the Waves WFR channel; (d) magnetic wave amplitudes of magnetosonic waves; (e) magnetosonic wave normal angles; (f) wave magnetic compressibility; (g) calculated magnetosonic wave local growth rates using the same methods in Chapter 4. Here the magnetic compressibility is defined as $(|B_{w,\parallel}|/|B_w|)^2$, where $B_{w,\parallel}$ and B_w are the parallel component of the wave magnetic field power spectral density and the total wave magnetic field power spectral density respectively.

The spacecraft was traveling nearly radially inward near the Earth's magnetic equator. The upper hybrid resonance frequency line as highlighted by the white solid line in the HFR spectra (Figure 5.3a) indicates that the spacecraft was inside the plasmapause after $\sim$ 09:50 UT. The proton phase space density (PSD) measurements at different energies and pitch angles (not explicitly shown here) indicate the existence of the ion ring distribution. The energy spectra of proton PSD at a pitch angle of 90° (Figure 5.3b) show that an ion ring distribution was formed inside the plasmapause and extended deep into the plasmasphere. The proton ring energy E_R, which is defined as the proton perpendicular energy associated with the peak PSD value, is a few keV during this event. Previous analysis [e.g., *Chen et al.*, 2010, 2011] has demonstrated that an ion ring distribution may potentially excite magnetosonic waves when E_R is close to the local Alfven energy E_A ($E_A = B_0^2/(2\mu_0 N)$, where μ_0 is the vacuum permeability, N is the plasma density, and B_0 is the background magnetic field intensity). Magnetosonic waves below the lower hybrid resonance frequency f_{LHR} (the white solid line) are captured in the WFR magnetic field power spectrogram (Figure 5.3c). Between $\sim$ 10:08 UT and $\sim$ 11:15 UT, the magnetosonic waves have nearly constant frequencies. Following the inward trajectory of the spacecraft, the magnetosonic waves become most intense at around 10:20 UT, and gradually fade further inside the plasmasphere. After $\sim$ 11:15 UT, the spacecraft observed weaker magnetosonic waves extending to increasingly higher frequencies, following the f_{LHR} trend. We integrated the magnetic field power spectral density over the frequencies between f_{cp} and f_{LHR} to obtain the wave amplitude during the magnetosonic wave event. As shown by the wave normal angle, wave compressibility, and wave ellipticity distribution, most of the wave power between f_{cp} and f_{LHR} are identified as fast magnetosonic waves. The magnetosonic wave amplitude (Figure 5.3d) remained higher than 100 pT for $\sim$ 15 minutes, indicating that strong magnetosonic waves were present over a broad region near the equatorial plane. The wave normal angle

distribution (Figure 5.3e) shows that the waves are highly oblique, thus the wave vectors lie near the equatorial plane and the waves can propagate both radially and azimuthally. The high wave magnetic compressibility (Figure 5.3f) indicates that the wave magnetic component parallel to the background magnetic field is the dominant component, and these waves are fast magnetosonic mode.

Using the same technique as [*Ma et al.*, 2014a] also shown in Chapter 4, we perform a local magnetosonic wave instability analysis on the observed proton PSD distribution. The full pitch angle coverage of the ion ring distribution is obtained from the HOPE instrument with sufficient pitch angle resolution. The wave growth rates (Figure 5.3g) are calculated from $\sim$ 10:08 UT to $\sim$ 12:00 UT when the ion ring distributions are present, and the results are clearly modulated by the relative ratio of E_A (the white solid line in Figure 5.3b) to E_R (the black dotted line in Figure 5.3b). Close to the plasmapause, E_A is slightly lower than E_R, and strong growth rates occur over a broad frequency band. The local growth rates fade away after $\sim$ 10:40 UT when the ratio of E_A/E_R drops below $\sim$ 0.1. Deeper inside the plasmasphere after $\sim$ 11:30 UT, E_A gradually increases due to the increase of the background magnetic field strength. When E_A becomes slightly lower than E_R, the calculation of magnetosonic wave growth rate exhibits modestly positive values associated with the weak proton ring distributions. The local instability analysis is consistent with the observed magnetosonic wave power spectrum in the outer region before $\sim$ 10:40 UT, but cannot account for the existence of relatively strong magnetosonic waves between 10:45 UT and 11:15 UT. This feature is similar with the magnetosonic wave event studied in Chapter 4, and will be addressed in the next section.

5.4 Trapping of magnetosonic waves in the plasmasphere

According to the magnetosonic wave propagation analysis in [*Chen and Thorne*, 2012], the quantity $Q = nL\sin\psi$ is conserved along the ray path during near-perpendicular propagation in an axisymmetric or locally axisymmetric medium, where n is the refractive index and ψ is the wave azimuthal angle, with 0° (180°) being directing radially outward (inward) and 90° (270°) being directing azimuthally toward later (earlier) local time. Consequently, magnetosonic waves launched over a wide range of azimuthal angles may be trapped in the outer plasmasphere due to the maximum of the refractive index at the inner edge of plasmapause for a given wave frequency. As the wave propagates away from the inner edge, the refractive index decreases rapidly, thus the azimuthal angle approaches 90° and radial reflection occurs. The ray can be reflected radially at the innermost or outermost L-shell corresponding to the azimuthal angle of 90°. For a wave launched at given L, ψ and wave frequency, we can calculate corresponding Q and then determine the radial range of the innermost and outermost L-shell of trapping region by the reflection condition $Q(\psi = 90°) = nL$ [*Chen and Thorne*, 2012]. We can use this range, which has wave frequency dependence, to predict the radial extent of magnetosonic wave trapping at different wave frequencies.

To analyze the trapping region of the observed magnetosonic wave event, we have made several assumptions: (1) the magnetosonic waves propagate in a two dimensional equatorial plane; (2) the azimuthal spatial variations in the background plasma density are small; (3) the temporal variations during the $\sim$ 2 hours period of the observation are small; (4) the wave source is well captured by the spacecraft during its inbound or outbound orbit. These assumptions are necessary and consistent with the assumptions in Section 5.2 and *Chen and Thorne* [2012].

In Figure 5.4, we use the conservation of Q to study the effects of magnetosonic wave propagation during 10:00 – 12:00 UT on 04 December 2012. The different

panels show the following: (a) The total plasma density inferred from the upper hybrid resonance frequency line in Figure 5.3a; (b) magnetic field power spectral density in the Waves WFR channel; (c) wave azimuthal propagation angle; (d) wave magnetic field power spectral density at 43.79 Hz; (e) calculated $Q(\psi = 90°) = nL$ profile at 43.79 Hz; and (f) estimated magnetosonic wave trapping region from the trapping analysis.

During the inbound path of the spacecraft, the plasma density (Figure 5.4a) increases from $\sim$ 60 cm^{-3} at $L \sim 5.2$ to $\sim$ 800 cm^{-3} at $L \sim 4.2$ where the magnetosonic waves fade out. The distribution of observed azimuthal wave angles (Figure 5.4c) is scattered, yet magnetosonic waves at the outer regions are observed to be mainly propagating inward to lower L-shells. The magnetosonic wave intensity at 43.79 Hz is shown in Figure 5.4d, and we calculated the value of $Q(\psi = 90°) = nL$ at the same frequency in Figure 5.4e. After magnetosonic waves are locally excited inside $L \sim 5.2$, the outer boundary of the observed wave trapping (indicated by the left end of the red two-way arrow in Figure 5.4e) is used to identify the minimum $Q(\psi = 90°)$ value (Q_{min}), and the inner boundary of the trapping region is then determined at the location where $Q(\psi = 90°)$ drops below Q_{min} deep inside the plasmasphere, which is indicated by the right end of the red two-way arrow in Figure 5.4e. The predicted trapping region in Figure 5.4e agrees well with the observed wave intensity in Figure 5.4d. We also calculated the trapping region at different frequencies in Figure 5.4f. The simulated trapping region covers the observed wave extent reasonably well, indicating that magnetosonic waves are excited at relatively larger L-shells mainly between $\sim$ 5.0 and $\sim$ 5.2, subsequently are able to propagate inward to $L =\sim$ 4.0, and thus become trapped at L-shells between $\sim$ 4.0 and $\sim$ 5.2. The magnetosonic waves with nearly constant frequency bands are occasionally observed by the spacecraft in the plasmasphere, and the similar technique can be used to verify the possible trapping of the observed waves.

5.5 Magnetosonic waves trapped by local density structures

Because the Q values are dependent on total plasma density values, the local plasma density structures may produce a maximum value of nL, therefore affecting the trapping regions and subsequently controlling the presence of trapped magnetosonic waves. This may provide a reasonable explanation for the modulation of magnetosonic waves by the total plasma density variations.

Figure 5.5 shows an example of magnetosonic waves that are modulated by the local density structures in the plasmasphere. The different panels show the following: (a) the total plasma density inferred from the upper hybrid resonance frequency line measured by the Waves HFR channel; (b) proton PSD as a function of energy for a pitch angle of $\sim 90^\circ$ measured by the HOPE instrument; (c) magnetic field power spectral density in the Waves WFR channel; (d) wave ellipticity; (e) calculated magnetosonic wave local growth rates; (f) wave magnetic field power spectral density at 55.54 Hz; (g) calculated $Q(\psi = 90^\circ) = nL$ profile at 55.54 Hz; (h) estimated magnetosonic wave trapping region.

The spacecraft was traveling nearly radially away from the Earth. The total plasma density (Figure 5.5a) inferred from the wave power spectra in the HFR channel drops from more than 100 cm^{-3} to around 50 cm^{-3} at $L \sim 5.35$ and $L \sim 5.48$ respectively. The wave magnetic field power spectral intensity (Figure 5.5c) shows the intensification of magnetosonic waves with low ellipticity ~ 0 (Figure 5.5d), and the wave intensity modulation is associated with the density variations after $\sim$ 05:30 UT. The magnetosonic waves are also observed in a broad region inside the plasmasphere from $\sim$ 03:50 UT to 05:40 UT. Clear ion ring distributions (Figure 5.5b) are observed after $\sim$ 04:40 UT, and the calculation of local magnetosonic wave growth rates (Figure 5.5e) shows that the ion rings can locally excite magnetosonic waves outside $L \sim 5.1$ where E_R (the black dotted line

in Figure 5.5b) becomes comparable to E_A (the white solid line in Figure 5.5b).

We calculated the nL profile for 55.54 Hz in Figure 5.5g, which presents a potential trapping region at 55.54 Hz. The trapping region corresponding to each frequency band is calculated in Figure 5.5h. Our simulation of the trapping region clearly shows that the magnetosonic waves are trapped by the local density structure between $L \sim 5.35$ and $L \sim 5.48$ from ~ 40 Hz to ~ 100 Hz, which agrees well with observations. Inside $L \sim 5.35$, magnetosonic waves can be trapped over a limited inward radial extent to $L \sim 4.2$ at a frequency of ~ 40 Hz, or to $L \sim 5.0$ at a frequency of ~ 100 Hz. However, magnetosonic waves are observed much further inside the plasmasphere to $L \sim 3.35$. Also, the observed magnetosonic waves between $L \sim 3.7$ and $L \sim 4.2$ are much stronger than those in the identified source region outside $L \sim 5.1$. The observations are still consistent with our analysis provided that the magnetosonic waves inside $L \sim 4.2$ originate from another source that is not encountered by the localized trajectory of the Van Allen probes. In sum, our trapping region analysis demonstrates that the wave trapping (and therefore, the radial extent of the equatorial magnetosonic waves) is modulated by the local density enhancements.

5.6 Summary

The important features of the propagation of equatorial magnetosonic waves in the plasmasphere is addressed in this chapter. A simplified 2D propatation model for the wave trajectory near the magnetic equator inside the plasmapause is analyzed, and we have found that the wave trapping is an important and common feature for the radial extent of equatorial magnetosonic waves. We have used the Van Allen Probes EMFISIS wave data and HOPE proton flux data to investigate the instability and trapping mechanisms of magnetosonic waves in the Earth's plasmasphere. The EMFISIS instrument suite provides continuous high-

resolution equatorial magnetosonic wave measurements, as well as the essential information about the wave power spectrogram and polarization properties. The HOPE instrument provides high-resolution particle flux measurements which are needed for the analysis of magnetosonic wave instabilities. Using the observed background plasma conditions and assuming near-perpendicular propagation, we have estimated the trapping region of magnetosonic waves in the Earth's plasmasphere. The simulated trapping region agrees fairly well with the in-situ observed radial extent of the magnetosonic waves.

Our analysis on the magnetosonic wave and proton ring event on 04 December 2012 has demonstrated that the magnetosonic waves are locally excited near the equatorial plasmapause, subsequently propagate inwards to lower L-shells, and then become trapped over a limited radial region in the outer plasmasphere. This scenario is consistent with magnetosonic wave local excitation mechanism and perpendicular propagation properties in the previous studies [*Chen et al.*, 2010; *Chen and Thorne*, 2012; *Ma et al.*, 2014a]. A similar analysis of the magnetosonic wave event on 06 November 2012 has shown that magnetosonic waves can be excited and trapped in a localized region with enhanced density, and can therefore be modulated by density structures in the plasmasphere. However, magnetosonic waves observed deep inside the plasmapause may originate from a source region at very different magnetic local time (MLT), which was not sampled along the satellite orbit. The simulations on both events show that the existence of the equatorial magnetosonic waves may be controlled by the wave trapping mechanism.

Our proposed trapping mechanism provides a reasonable explanation for most observations of magnetosonic waves in the plasmasphere. The reconstruction of the observed wave power spectrogram requires a full ray tracing technique [e.g., *Xiao et al.*, 2012], and incorporation of the local wave excitation, damping and the propagation effects, which are interesting future topics but are beyond the scope of our current study. Nevertheless, using a simplified 2D wave trapping model, our

study clearly demonstrates that the propagation and subsequent trapping in the outer plasmasphere are important to account for magnetosonic wave observations in the plasmasphere.

The combined effects of local excitation and subsequent propagation of equatorial magnetosonic waves provide complete explanation about the wave distribution in the Earth's inner magnetosphere. Another important topic about the magnetosonic wave is the scattering effects, especially the influences on the electron distributions in the outer radiation belt. It has been found that intense magnetosonic waves can provide energy for electron acceleration, yet the effectiveness of typical magnetosonic waves and the detailed influences are not clear. With the recent survey of magnetosonic wave distributions, the electron scattering effects due to typical magnetosonic waves will be investigated in the next chapter.

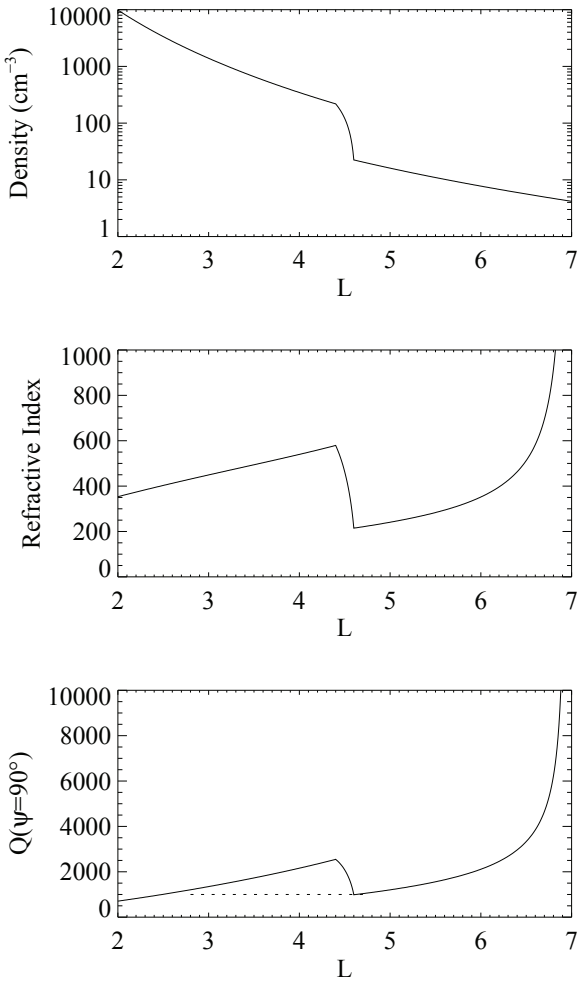

Figure 5.1: The radial calculation of $Q(\psi = 90°) = nL$ profile. (top) The assumed total plasma density model with a plasmapause at $L = 4.5$; (middle) the refractive index n; (bottom) the $Q(\psi = 90°) = nL$ profile as a function of L-shell. The dashed line in the bottom panel indicates the trapping region.

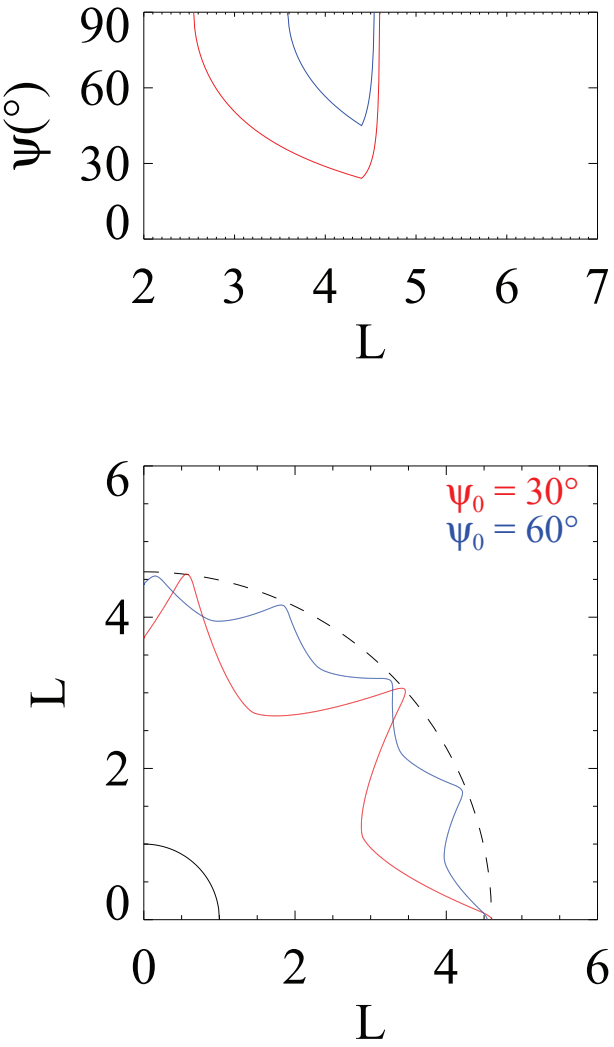

Figure 5.2: The examples of ray traces with an initial azimuthal angle of $\psi = 30°$ (red) and $\psi = 60°$ (blue) launched at $L = 4.5$. (top) The variations of wave azimuthal angle as a function of L-shell when the wave propagates; (bottom) the wave paths in the magnetic equatorial plane, showing the trapping of the waves in a limited radial region.

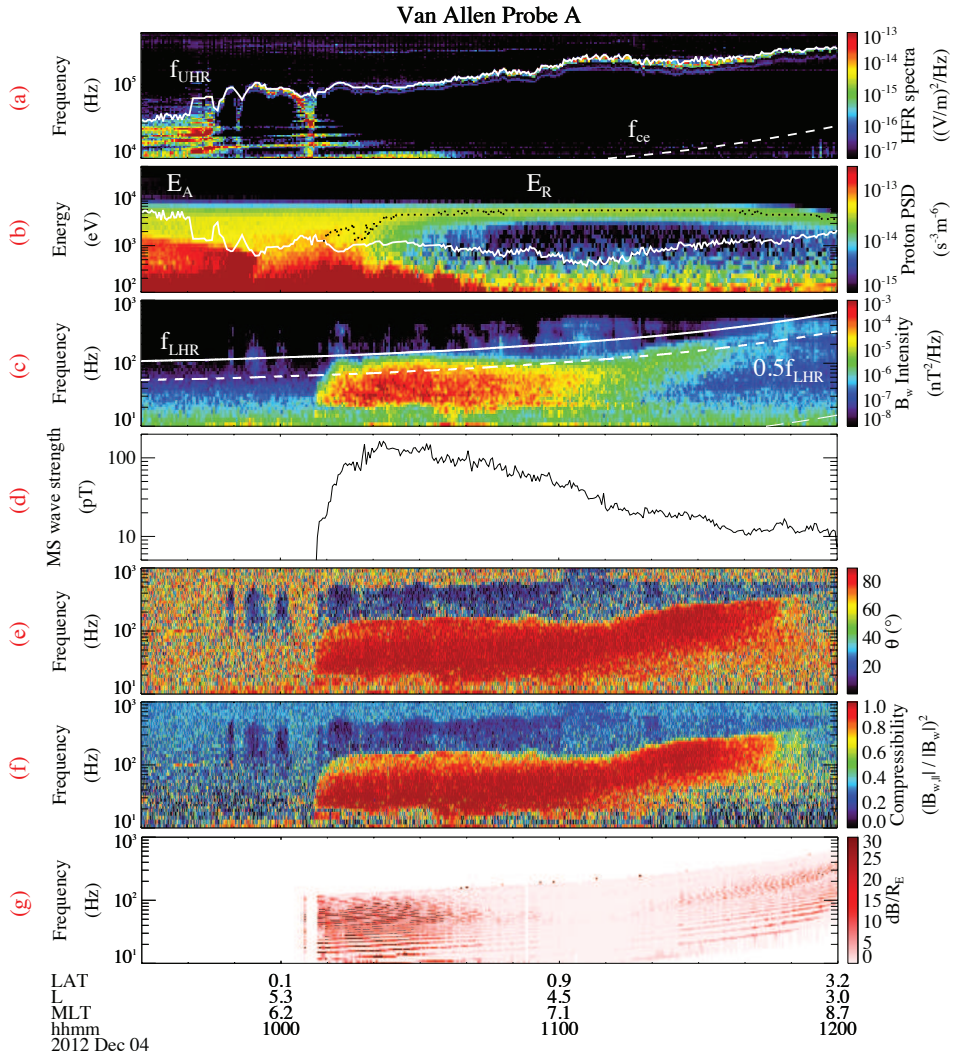

Figure 5.3: Magnetosonic waves observed by Van Allen Probe A on 04 December 2012 and the instability analysis. (a) The electric field power spectral density measured by HFR; (b) proton PSD as a function of energy for a pitch angle of 90°; (c) magnetic field power spectral density measured by WFR; (d) magnetic wave amplitudes of magnetosonic waves; (e) magnetosonic wave normal angles; (f) wave magnetic compressibility; (g) calculated magnetosonic wave local growth rates. In panel (c), the white solid line and the white dashed line represent f_{LHR} and $0.5f_{LHR}$ respectively.

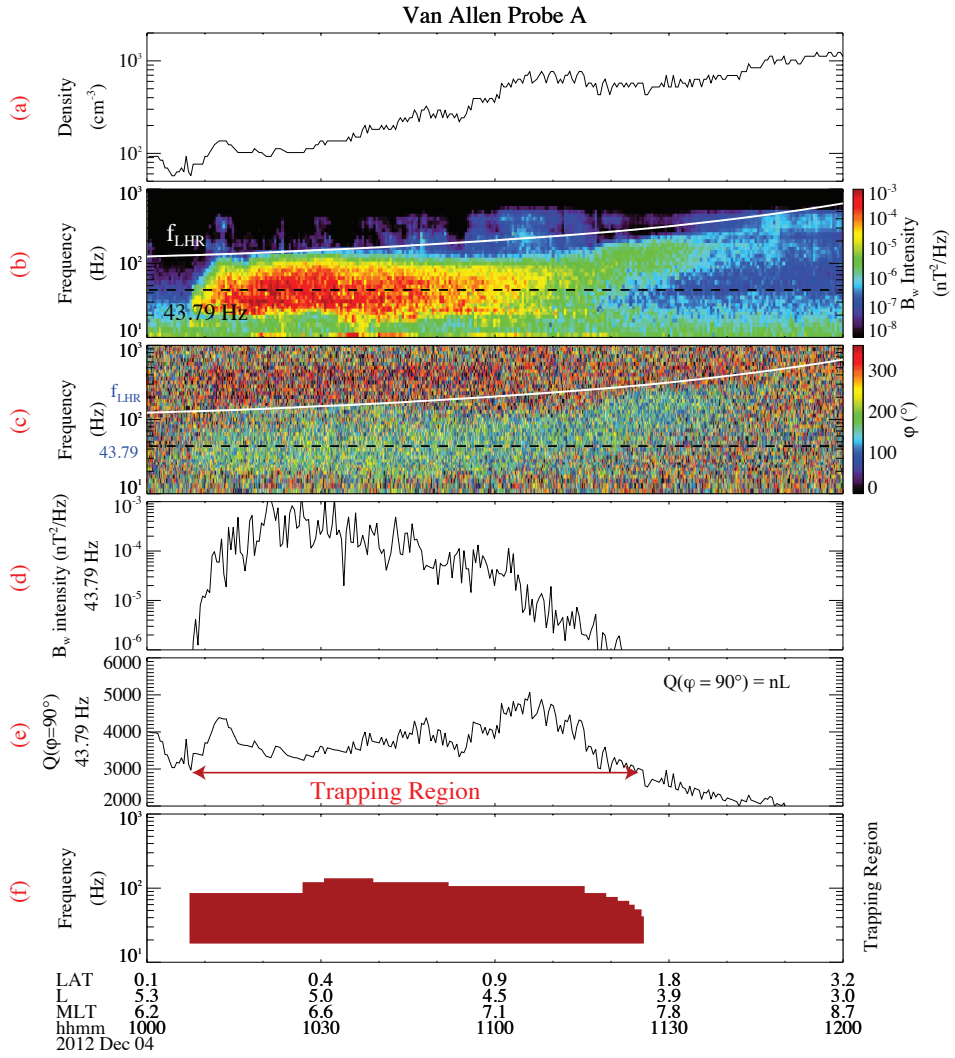

Figure 5.4: Trapping region analysis of magnetosonic wave event on 04 December 2012. (a) The total plasma density; (b) magnetic field power spectral density; (c) azimuthal propagation angle; (d) wave magnetic field power spectral density at 43.79 Hz; (e) calculated $Q(\psi = 90°) = nL$ profile at 43.79 Hz; (f) estimated magnetosonic wave trapping region. In panels (b) and (c), the white solid line and the black dashed line represent f_{LHR} and 43.79 Hz respectively; In panel (e), the red two-way arrow represents the predicted trapping region at 43.79 Hz.

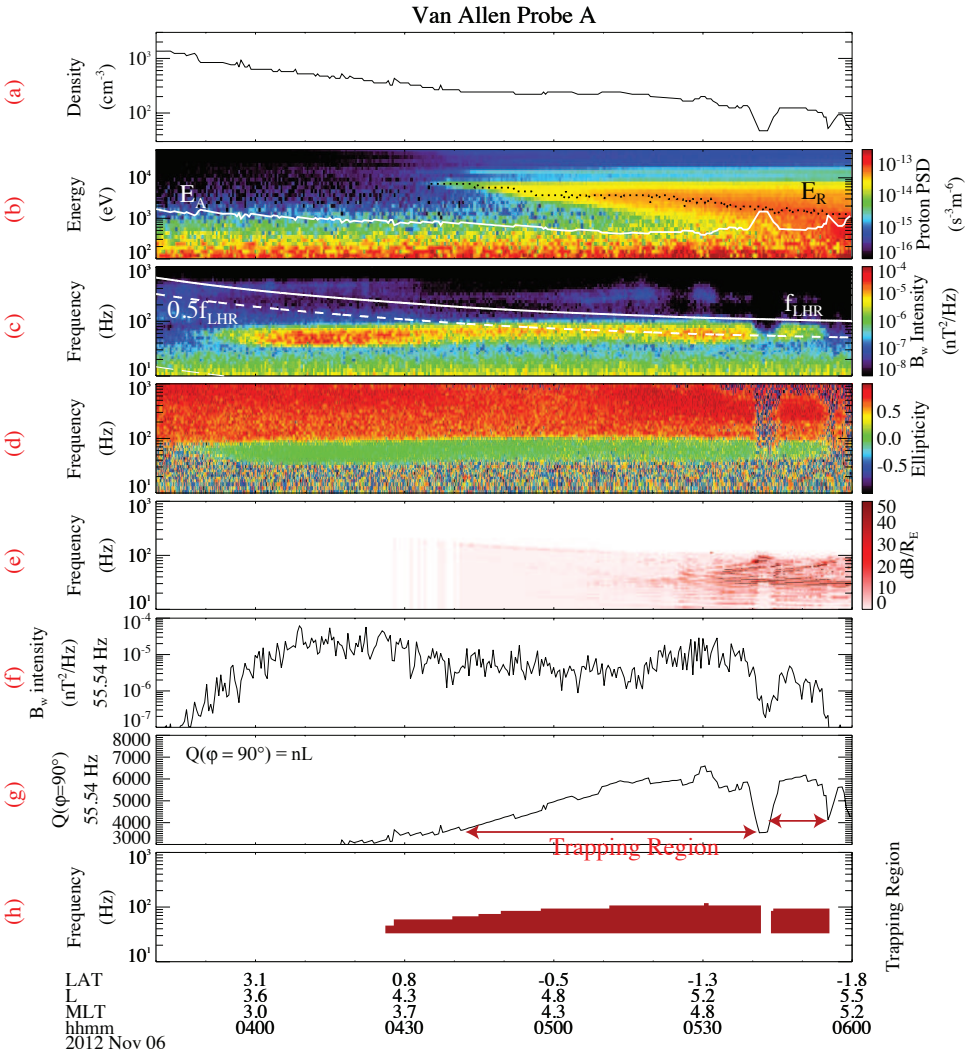

Figure 5.5: The local instability and trapping analysis of magnetosonic wave event on 06 November 2012. (a) The total plasma density; (b) proton PSD as a function of energy for a pitch angle of 90°; (c) magnetic field power spectral density; (d) wave ellipticity; (e) calculated magnetosonic wave local growth rates; (f) wave magnetic field power spectral density at 55.54 Hz; (g) calculated $Q(\psi = 90°) = nL$ profile at 55.54 Hz; (h) estimated magnetosonic wave trapping region. In panel (b), the white solid line and the black dotted line represent E_A and E_R respectively; In panel (g), the red two-way arrows represent the predicted trapping regions.

CHAPTER 6

Electron scattering due to typical magnetosonic waves in the inner magnetosphere

The whistler-mode electromagnetic waves interact with the encountered particles and alter their distributions in the inner magnetosphere. In the previous chapters, we have discussed the global distribution of magnetosonic waves, the wave excitation by ion ring distributions, and the wave propagation effects in the plasmasphere. The general roles of equatorial magnetosonic waves on the particle distributions is another important issue for a complete illustration about the waves in the inner magnetsphere. Therefore, a further study about the electron scattering effects in the outer radiation belts is required.

In this chapter, we investigate the electron acceleration and their phase space density (PSD) evolutoins due to typical magnetosonic waves in the inner magnetosphere. Since we are mostly interested in the general and long-term effects, the purpose of this chapter is to study the typical electron scattering due to statistical magnetosonic wave distributions in absence of other emissions (e.g., plasmaspheric hiss and chorus), rather than an event study about the particle scattering due to intense magnetosonic waves or the additional roles of magnetosonic waves in aid of the hiss wave scattering in the plasmasphere and chorus wave acceleration outside the plasmapause. We perform statistical studies about the magnetosonic wave distributions using THEMIS and the Van Allen Probes wave measurements during the recent years. Both surveys show similar characters on the global distributions of root-mean-square averaged wave strength. We

also use the high resolution wave spectrogram from the Van Allen Probes to perform a statistical survey about the wave frequency distribution. Consistent with the typical magnetosonic wave events, the peak frequency of magnetosonic waves follows closely with the variation of the lower hybrid resonance frequency (f_{LHR}) outside the plasmapause, while the correlation between the wave frequency and f_{LHR} trend is not clear in the plasmasphere. Using the statistical wave frequency and amplitude information, we calculate the wave diffusion rates matrix with the recently developed analytical formula, and find that the electron acceleration due to magnetosonic waves is most effective outside the plasmapause around $L = 5$. However, the time scale of the electron energization during modestly disturbed condition is more than ten days, which is not effective for the electron dynamics compared with the scattering due to other emissions. Using the typical wave amplitude during disturbed conditions, we perform the 2D Fokker-Planck simulation to model the electron PSD evolution due to magnetosonic waves. Outside the plasmapause, the waves causes the electron acceleration between 50° and 70° in time scale of days, therefore forming the butterfly distribution of the electrons between 100 keV and 1 MeV; inside the plasmapause, the electron acceleration effect is weak due to the scattering in much narrower pitch angle bands. Our study suggests that intense magnetosonic waves may cause the butterfly distribution of radiation belt electrons especially outside the plasmapsue, but in general electron acceleration due to magnetosonic waves is not as effective as the chorus acceleration.

This chapter is organized as the following: Section 6.1 provides an introduction about the equatorial magnetosonic waves in the Earth's radiation belts, and we will focus on the particle scattering due to whistler-mode waves and the electron acceleration due to magnetosonic waves; the new statistical study about equatorial magnetosonic waves is presented in Section 6.2 and Section 6.3; the electron scattering effects due to typical magnetosonic waves is presented in Sections 6.4

- 6.7; we summarize our results and discuss the potential roles of magnetosonic waves in the outer radiation belts in Section 6.8.

6.1 Introduction

Fast magnetosonic waves are highly oblique whistler-mode electromagnetic emissions generated between the local proton gyrofrequency (f_{cp}) and the lower hybrid resonance frequency (f_{LHR}) [e.g., *Perraut et al.*, 1982; *Laakso et al.*, 1990; *Santolík et al.*, 2002; *Ma et al.*, 2013]. The wave events are occasionally observed when the spacecraft is within 5° near the Earth's magnetic equator [e.g., *Nemec et al.*, 2005, 2006; *Pokhotelov et al.*, 2008; *Santolík et al.*, 2004]. Near the equatorial plane, the waves occur in a wide region between 2 R_E and 8 R_E both inside and outside the plasmapause [e.g., *Meredith et al.*, 2008; *Ma et al.*, 2013]. The magnetosonic waves are strongest near the equator, near the dayside, between 2 R_E and 8 R_E, outside the plasmapause, and during geomagnetically disturbed conditions [e.g., *Ma et al.*, 2013]. The ion ring distributions provide free energy for the local excitation of magnetosonic waves when the ion ring energy is close to the local Alfven energy, which typically occur in a wide region outside the plasmapause and near the outer edge of the plasmasphere [e.g., *Chen et al.*, 2010; *Ma et al.*, 2014a]. The injected ion populations may account for the existence of magnetosonic waves especially near the dayside outside the plasmapause [e.g., *Chen et al.*, 2011]. Previous satellite observations also provide evidences for the propagation of magnetosonic waves near the equatorial plane, and the wave trajectory simulations have shown different characters of the wave perpendicular propagation paths in various conditions [e.g., *Kasahara et al.*, 1994; *Chen and Thorne*, 2012; *Ma et al.*, 2014b]. The plamsasphere naturally forms a trapping condition for the magnetosonic wave propagation, and provides a reasonable explanation for the existence and observed properties of the waves inside the plasmapause [*Ma*

et al., 2014b].

The electron dynamics in the Earth's outer radiation belt is mainly governed by the diffusion processes through the interactions with various plasma waves [*Kennel and Engelmann*, 1966; *Lyons*, 1974a,b]. The ultra-low frequency (ULF) waves caused by the disturbances in solar wind may lead to the radial diffusion and resultant transport of energetic electrons [e.g., *Cornwall*, 1972; *Shprits et al.*, 2008a; *Ozeke et al.*, 2014]. The high frequency electromagnetic waves may cause the local diffusion and resultant precipitation loss or non-adiabatic acceleration of energetic electrons [e.g., *Albert*, 2007; *Glauert and Horne*, 2005; *Li et al.*, 2007; *Shprits et al.*, 2008b; *Summers*, 2005; *Xiao et al.*, 2010]. The most important plasma waves that may cause the electron local acceleration in the radiation belts are whistler-mode chorus and magnetosonic waves. The Van Allen Probes observations and the related simulation studies have provided solid confirmations that the whistler-mode chorus waves provide sufficient local heating of energetic electrons in the heart of radiation belts during geomagnetic storm periods [*Reeves et al.*, 2013; *Thorne et al.*, 2013a; *Fennell et al.*, 2014; *Foster et al.*, 2014; *Li et al.*, 2014b]. The electron phase space density (PSD) may increase by more than two orders of magnitude during several hours scattering by intense chorus waves. Intense magnetosonic wave events are also observed by the spacecraft in the inner magnetosphere, and have a potential role in electron accelerations [*Horne et al.*, 2007; *Bortnik and Thorne*, 2010; *Li et al.*, 2014a].

Magnetosonic waves are known to cause the electron scattering via Landau resonance and transit-time scattering effects [*Horne et al.*, 2007; *Bortnik and Thorne*, 2010]. During Landau resonant interactions, the electrons experience a constant parallel electric field in the frame of moving electrons. Therefore, after gyro-averaging the magnetosonic waves mainly causes the acceleration of electrons in the parallel direction with respect to the background magnetic field. Landau resonance is most effective for hundreds keV electrons with pitch angles between 50°

and 80°. In addition, *Bortnik and Thorne* [2010] have found that the streaming electrons experience only a fraction of magnetosonic wave periods during their bounce motions. The wave electric fields perpendicular to the background magnetic field in the frame of moving electrons may cause the additional scattering due to the transit-time effects. As a consequence, magnetosonic waves cause electron scatterings in a wider range of pitch angles than Landau resonance regime. Within the Landau resonance regime, the test-particle simulations including transit-time effects agree with the quasi-linear calculations. The timescale of electron acceleration due to the intense magnetosonic wave event with an amplitude of ~ 218 pT is several days [*Horne et al.*, 2007; *Bortnik and Thorne*, 2010; *Li et al.*, 2014a].

The general role of equatorial magnetosonic waves in particle scattering is another important issue in the Earth's radiation belt dynamics. The evaluation of electron acceleration due to typical magnetosonic waves at different locations and under different conditions could provide information about their potential effects and references for inclusion of those waves in radiation belt simulations. The equatorial spacecraft THEMIS and the Van Allen Probes provide excellent observation about the magnetosonic wave amplitude distribution, occurrence rate, and the wave frequency spectrum statistics. The statistical information about the waves can be used to estimate the wave scattering rates, especially the energy diffusion coefficients, and obtain an understanding about the averaged effects of magnetosonic waves under typical conditions.

The main part of this chapter is organized into the observation sections and the simulation sections. Using the Van Allen probes data, Section 6.2 presents the global distributions of magnetosonic wave amplitudes, and Section 6.3 presents the statistics of wave frequency spectra at different locations. Section 6.4 presents the analytical formula for calculating the electron diffusion coefficients due to equatorial magnetosonic waves. The energy diffusion coefficients due to magnetosonic waves during modestly disturbed conditions are calculated in Section 6.5. The

electron PSD evolution due to magnetosonic waves during disturbed conditions are simulated inside and outside the plasmapause in Section 6.6 and Section 6.7, respectively.

6.2 Global distribution of magnetosonic waves using recent Van Allen Probes data

The wave amplitude distribution is an important factor in controlling the global scattering rates. In Chapter 3, we have performed a statistical study about the equatorial magnetosonic wave distribution using THEMIS wave dataset from May 2010 to November 2012. The Van Allen Probes have been launched into the Earth's radiation belts environment on 30 August 2012. The orbits of the spacecraft are near equator and highly elliptical, and the spacecraft provide high-resolution measurements about the magnetosonic wave distributions between $\sim 2R_E$ and $\sim 6R_E$ [*Mauk et al.*, 2013].

The background magnetic field and the wave electric and magnetic fields are measured by the Electric and Magnetic Field Instrument Suite and Integrated Science (EMFISIS) [*Kletzing et al.*, 2013], using the magnetometer and the Waves instrument respectively. The Waveform Receiver (WFR) of the Waves instrument measures wave power spectral density from 10 Hz to 12 kHz for all the three components of both electric field and magnetic field. The WFR also provides wave polarization properties including wave normal angle and ellipticity, calculated by the Singular Value Decomposition (SVD) method [*Santolík et al.*, 2003]. The High Frequency Receiver (HFR) of the Waves instrument measures the electric field spectra density from 10 kHz to 400 kHz [*Kletzing et al.*, 2013], which covers the upper hybrid resonance frequency f_{UHR} range in the inner magnetosphere and can therefore be used to identify the location of the spacecraft with respect to the plasmapause.

Figure 6.1 presents the one-day overview of magnetosonic waves observed by Van Allen Probe A on 06 October 2012. The different panels in Figure 6.1 shows the following: (a) the AE index; (b) wave electric field power spectral density from HFR measurements; (c) plasmapause indicator with 0 and 1 denoting inside and outside the plasmapause respectively; (d) wave magnetic field power spectral density from WFR measurements; (e) wave ellipticity; and (f) wave normal angle. The white lines in Figure 6.1b denote the lines of $2f_{ce}$, f_{ce}, and $0.5f_{ce}$; the white lines in Figure 6.1d denote the lines of f_{LHR}, $0.5f_{LHR}$, and f_{cp}.

The electrostatic Electron Cyclotron Harmonic (ECH) wave activities are clearly observed at frequencies higher than the electron gyrofrequency f_{ce} outside the plasmapause by HFR in Figure 6.1b, and the intensity of ECH waves are used to identify whether the spacecraft is in the plasmasphere or the plasmatrough region as shown in Figure 6.1c. The equatorial magnetosonic waves are observed between the proton gyrofrequency f_{cp} and the lower hybrid resonance frequency f_{LHR}. Magnetosonic waves are identified as the highly oblique and nearly linearly polarized electromagnetic emissions, and we require that the absolute value of magnetosonic wave ellipticity (Figure 6.1e) to be lower than 0.2, and the magnetosonic wave normal angle (Figure 6.1f) should be higher than 80°. Using these criteria, the magnetosonic waves are automatically selected among other plasma waves that may co-exist in the same frequency band (e.g., hiss emissions) in the wave power spectrogram. The magnetosonic wave amplitude is obtained by integrating the selected magnetosonic wave magnetic power intensities.

We have surveyed the magnetosonic wave intensity using the Van Allen Probes WFR dataset from October 2012 to November 2014. Figure 6.2 presents the global distribution of magnetosonic wave amplitudes in the magnetic equatorial plane between 2 R_E and 6 R_E. The global distributions of root-mean-square (RMS) averaged wave amplitude are categorized by different AE* conditions, inside or outside the plasmapause, and different magnetic latitudes (LAT). Here AE* is the

maximum AE value during the previous 3 hours. The sample numbers (N_s) is shown on the right bottom panels, which shows that the two years survey provides sufficient data coverage for the wave statistics. The white area represents the locations with N_s less than 100 counts.

Consistent with the previous THEMIS survey, the strongest magnetosonic waves are observed between 3 R_E and 5 R_E, near the dayside, outside the plasmapause, near the equator, and during disturbed conditions. More uniform distribution of magnetosonic waves is observed inside the plasmapause, while the magnetosonic wave intensity is much higher near the dayside than the nightside outside the plasmapause. During disturbed conditions when AE* is higher than 300 nT, the averaged wave amplitude is between 50 and 100 pT near the dayside outside the plasmapause, which is more intense than the waves shown in the previous THEMIS survey. This is because that the previous THEMIS survey is performed near the solar minimum period (May 2010 to November 2012), while the new Van Allen Probes survey is performed closer to the solar maximum period (October 2012 to November 2014) during which more extreme events are measured under the same criterion of $AE* > 300$ nT. We have also extended the THEMIS survey towards November 2014, and the new four years THEMIS survey provides very similar characters and RMS wave amplitudes with the Van Allen Probes survey.

We have investigated the magnetosonic wave occurrence rates for different levels of wave amplitudes. Figure 6.3 presents the global distribution of magnetosonic wave occurrence rates categorized in the same format with Figure 6.2. Strong magnetosonic waves with amplitudes higher than ~ 50 pT may potentially cause scattering effects of radiation belt electrons. Most of the strong magnetosonic waves are observed between 3 R_E and 5 R_E, near the dayside, outside the plasmapause, and near the equator. The highest occurrence rate is 30% to 50% during all different geomagnetic conditions, implying that the strong magnetosonic waves may occasionally have potentially significant local effects in radiation belt

dynamics. The statistical results of the wave distribution will be used to evaluate the global scattering effects of magnetosonic waves.

6.3 Statistics about magnetosonic wave frequency spectrum

The wave frequency spectrum is another important factor that determines the wave scattering rates and the resonance energy of energetic electrons. Although the wave frequency spectrum characters of individual magnetosonic wave event have been investigated in the previous studies, the magnetosonic wave frequency spectrum statistics can be used for the study of long term and general effects. The magnetosonic wave frequency spectrum statistics can be obtained from the Van Allen Probes wave dataset with high frequency resolutions.

Figures 6.4 and 6.5 presents the survey of time-averaged magnetosonic wave intensity distribution as a function of L-shell and wave frequency. The wave intensity distributions are categorized into different magnetic local time (MLT) sectors with a MLT width of 6 h. The white solid lines in each panel denote the lines of f_{LHR} (above) and f_{cp} (below), which are estimated from a dipole magnetic field. It is generally convenient for calculating the scattering rates by assuming a Gaussian wave frequency spectrum. By performing a Gaussian fitting of the wave frequency spectrum, the wave frequency with a peak wave intensity is denoted by the black solid line, and the frequency width is denoted by the two white dashed lines in each panel.

Consistent with the global survey of wave amplitude distributions, the most intense magnetosonic waves are located near the noon sector, between 3 R_E and 5 R_E, and outside the plasmapause, with a peak wave frequency between 30 Hz and 100 Hz. The wave frequency from the statistical survey also follows more closely with the variation of f_{LHR} and f_{cp} outside the plasmapause, while this trend is

not clear inside the plasmapause. This feature is consistent with the frequency features of the observed wave events, and explained as a combined effect of wave local excitation and perpendicular propagation in the previous chapters. The wave frequency spectra at different locations are obtained by normalizing the wave intensity spectra, and we combine the wave frequency information with the wave amplitude distributions in Figure 6.2 to calculate the general scattering rates due to magnetosonic waves.

6.4 Analytical formula for electron scattering due to equatorial magnetosonic waves

The magnetosonic waves are spatially localized near the geomagnetic equator within $\sim 2^\circ - 3^\circ$ according to the previous observations [e.g,, *Nemec et al.*, 2005, 2006; *Pokhotelov et al.*, 2008; *Santolík et al.*, 2004], and *Bortnik et al.* [2015] have found that the motions of electrons streaming through the magnetosonic waves may be simplified with several reasonable assumptions: 1. the wave magnetic field B_w is confined within the geomagnetic latitude width of λ_w and has a Gaussian distribution $B_w = B_{w,0}\exp(-\lambda^2/\lambda_w^2)$; 2. higher harmonic resonances with harmonic number $|N| \geq 1$ are ignored, because generally the first order cyclotron resonance requires a resonance energy higher than ~ 10 MeV; 3. adiabatic variations of the particle's motion are ignored because the interactions occur only in the vicinity of the magnetic equator; 4. the background magnetic field along the bounce trajectory of the electron is assumed as the Taylor expansion of a dipole field strength; 5. the initial pitch angle of the electrons should be less than 80° so that the electrons are able to travel through the wave region.

The electron's momentum equation in the presence of the strong background magnetic field (B_0) and the magnetosonic electric (E_w) and magnetic (B_w) fields could be simplified, and *Bortnik et al.* [2015] have obtained the analytical formula

for calculating the perturbations of the electron's parallel ($\Delta p_{\parallel}$) and perpendicular ($\Delta p_{\perp}$) momentum as following:

$$\Delta p_{\parallel,\perp} = \sqrt{\pi} A_{\parallel,\perp} (\frac{z_w}{v_{\parallel}}) \sin\eta_0 \exp(-(\frac{z_w}{v_{\parallel}})^2 \frac{(\omega - k_{\parallel} v_{\parallel})^2}{4}), \tag{6.1}$$

where the subscripts $\parallel$ and $\perp$ denote the parallel and perpendicular components respectively, z_w is the latitudinal distance of the wave confinement, η_0 is the initial wave phase angle, v is the electron velocity, ω is the wave frequency, and k is the wave vector.

The parameters $A_{\parallel}$ and $A_{\perp}$ are proportional to the wave amplitude B_w and are expressed as the following:

$$A_{\parallel} = \frac{\omega_{\tau m}^2 m_e}{k_{\parallel}} \tag{6.2}$$

$$A_{\perp} = \omega_1 (\frac{p_{\parallel}}{\gamma} + m_e R_1) J_{-1}(\beta) - \omega_2 (\frac{p_{\parallel}}{\gamma} - m_e R_2) J_{+1}(\beta), \tag{6.3}$$

where m_e is the electron mass, e is the elementary charge, J is the Bessel function of the first kind. The other parameters are the same as *Bortnik et al.* [2015] and are repeated here for completeness of the equations:

$$\beta = \frac{k_{\perp} p_{\perp}}{m_e \omega_{ce}} \tag{6.4}$$

$$\omega_{\tau m}^2 = (-1)^{m-1} \omega_{\tau 0}^0 (J_{m-1}(\beta) - \alpha_1 J_{m+1}(\beta) + \gamma \alpha_2 J_m(\beta)) \tag{6.5}$$

$$\omega_{\tau 0}^2 = \frac{\omega_1 k_{\parallel} p_{\perp}}{\gamma m_e} \tag{6.6}$$

$$\omega_1 = \frac{e}{2m_e} (B_{w,x} + B_{w,y}) \tag{6.7}$$

$$\omega_2 = \frac{e}{2m_e} (B_{w,x} - B_{w,y}) \tag{6.8}$$

$$\alpha_1 = \frac{\omega_2}{\omega_1} \tag{6.9}$$

$$\alpha_2 = \frac{e E_{w,x}}{\omega_1 p_{\perp}} \tag{6.10}$$

$$R_1 = \frac{E_{w,x} + E_{w,y}}{B_{w,x} + B_{w,y}} \tag{6.11}$$

$$R_2 = \frac{E_{w,x} - E_{w,y}}{B_{w,x} - B_{w,y}} \tag{6.12}$$

where ω_{ce} is the electron gyrofrequency, and k is related with the refractive index as $k = \omega n/c$. The calculations of the wave dispersion relation and different components of the wave electric and magnetic fields are shown in Chapter 2.

After obtaining the variations in parallel and perpendicular momentums of the streaming electrons, the gyro-phase averaged perturbations in electron pitch angle, energy, and total momentum can also be derived, and the results are averaged over a bounce period (τ_B) of the electrons to obtain the bounce averaged diffusion coefficients.

The bounce-averaged pitch angle diffusion coefficient is expressed as:

$$D_{\alpha\alpha} = \frac{\pi}{2}\frac{A_\alpha^2}{\tau_B}(\frac{z_w}{v_\parallel})^2 \exp(-(\frac{z_w}{v_\parallel})^2 \frac{(\omega - k_\parallel v_\parallel)^2}{2}), \tag{6.13}$$

where α is the pitch angle of the electron, and A_α is expressed as:

$$A_\alpha = \frac{\cos\alpha}{p}A_\perp - \frac{\sin\alpha}{p}A_\parallel. \tag{6.14}$$

The bounce-averaged energy diffusion coefficient is expressed as:

$$D_{EE} = \frac{\pi}{2}\frac{A_E^2}{\tau_B E^2}(\frac{z_w}{v_\parallel})^2 \exp(-(\frac{z_w}{v_\parallel})^2 \frac{(\omega - k_\parallel v_\parallel)^2}{2}), \tag{6.15}$$

where E is the energy of the electron, and A_E is expressed as:

$$A_E = v_\parallel A_\parallel + v_\perp A_\perp. \tag{6.16}$$

The bounce-averaged momentum diffusion coefficient is expressed as:

$$D_{pp} = \frac{\pi}{2}\frac{A_p^2}{\tau_B p^2}(\frac{z_w}{v_\parallel})^2 \exp(-(\frac{z_w}{v_\parallel})^2 \frac{(\omega - k_\parallel v_\parallel)^2}{2}), \tag{6.17}$$

where A_p is expressed as:

$$A_p = \sin\alpha A_\perp + \cos\alpha A_\parallel. \tag{6.18}$$

The bounce-averaged mixed pitch angle-momentum diffusion coefficient is expressed as:

$$D_{\alpha p} = \frac{\pi}{2}\frac{A_\alpha A_p}{\tau_B p}(\frac{z_w}{v_\parallel})^2 \exp(-(\frac{z_w}{v_\parallel})^2 \frac{(\omega - k_\parallel v_\parallel)^2}{2}). \tag{6.19}$$

The calculation of the diffusion coefficients using the analytical formula has been proven to be both computationally efficient and accurate in capturing the important features of Landau resonance and transit-time effects due to equatorial magnetosonic waves. We will use the analytical formula to evaluate the general scattering effects of magnetosonic waves at different locations and under different conditions.

6.5 Energy scattering rates due to typical magnetosonic waves

The electron scattering efficiency are estimated using the diffusion coefficients due to magnetosonic waves. Since the magnetosonic waves mainly causes the electron acceleration by Landau resonance, in this section we focus on the energy diffusion coefficients to estimate the time scale of the electron energization. Using the analytical formula and the wave amplitude and frequency spectrum information from the Van Allen Probes survey, we calculate the diffusion coefficients at different locations and under different geomagnetic conditions. The background magnetic field is approximated as a dipole magnetic field, and we used Sheeley's total plasma density model in the plasmasphere and the plasmatrough regions [*Sheeley et al.*, 2001]. The diffusion coefficients are drift-averaged over different MLT sectors.

Figures 6.6 and 6.7 presents the energy diffusion coefficients at different L-shells calculated under the modestly disturbed condition when 100 nT $\leq AE* \leq$ 300 nT inside and outside the plasmapause, respectively. The energy diffusion coefficients are shown as a function of electron equatorial pitch angle and energy.

The peak profile of the diffusion coefficient is well correlated with the trend of Landau resonance, which requires that the electron pitch angle α and velocity v satisfying $v\cos\alpha = \omega/k_{\|}$. The major feature of the energy diffusion coefficient is caused by Landau resonance. Transit-time effect, on the other hand, causes the additional scattering over much broader pitch angle ranges at different energies.

The energization of electrons due to magnetosonic waves is most efficient around $L = 5$ outside the plasmapause. Inside the plasmapause, the RMS averaged wave amplitudes are weaker, and the scattering occurs over a much narrower pitch angle range than outside the plasmapause. In general, as the ratio f_{pe}/f_{ce} increases, the magnetosonic waves may cause electron scattering at higher and narrower pitch angle ranges. The electrons over the pitch angle range of 50° to 80° and energy range of 10 keV to 1 MeV may be accelerated via Landau resonance. The highest energy diffusion coefficient corresponds to an acceleration time scale of tens of days, which is slower than the electron energization by whistler-mode chorus waves under the similar conditions.

6.6 Electron PSD evolutions due to magnetosonic waves outside the plasmapause

The magnetosonic waves may cause different electron PSD distributions from the influences by whistler-mode chorus waves. The butterfly distribution of the hundreds of keV electrons has been observed in the slot region and inner radiation belt by the Van Allen Probes recently, and scattering by intense magnetosonic waves is a reasonable candidate for the formation of the observed pitch angle distribution. In this section, we will investigate the characters of electron PSD distribution under the influence of magentosonic waves outside the plasmapause.

We have calculated the pitch angle, momentum, and mixed pitch angle-momentum diffusion coefficients as a function of pitch angle and energy at $L = 4.5$ outside the

plasmapause as shown in Figure 6.8. The wave amplitudes are assumed to be 75 pT on the dayside MLT sectors and 25 pT on the nightside, which is equivalent to the RMS averaged wave distributions during disturbed conditions. Because Landau resonance causes the electron acceleration along $v_{\|}$ direction, the increase in electron energy corresponds to the decrease in electron pitch angle, and the major part of $D_{\alpha p}$ is negative. The pitch angle diffusion coefficients are less than 10^{-9} s^{-1} at pitch angles less than $\sim 25^{\circ}$ at different energies, therefore the magnetosonic waves cannot cause electron precipitation in the Earth's radiation belts.

We simulate the electron evolution by numerically solving the following 2D Fokker-Planck equation using the Alternative Directional Implicit (ADI) method [*Xiao et al.*, 2009]:

$$\begin{aligned}\frac{\partial f}{\partial t} &= \frac{1}{S(\alpha)\sin\alpha\cos\alpha}\frac{\partial}{\partial\alpha}(S(\alpha)\sin\alpha\cos\alpha\langle D_{\alpha\alpha}\rangle\frac{\partial f}{\partial\alpha}) \\ &+ \frac{1}{S(\alpha)\sin\alpha\cos\alpha}\frac{\partial}{\partial\alpha}(S(\alpha)\sin\alpha\cos\alpha\langle D_{\alpha p}\rangle\frac{\partial f}{\partial p}) \\ &+ \frac{1}{p^2}\frac{\partial}{\partial p}(p^2\langle D_{p\alpha}\rangle\frac{\partial f}{\partial\alpha}) \\ &+ \frac{1}{p^2}\frac{\partial}{\partial p}(p^2\langle D_{pp}\rangle\frac{\partial f}{\partial p}),\end{aligned} \tag{6.20}$$

where f is the electron PSD, t is time, and $S(\alpha)$ is a function related to the bounce period and in a dipole field it can be approximated by $S(\alpha) = 1.38 - 0.32\sin\alpha - 0.32\sqrt{\sin\alpha}$ [*Lenchek et al.*, 1961].

The lower and higher energy boundary condition are set as constants at energies of 10 keV and 10 MeV respectively. $f(\alpha \leq \alpha_{LC}) = 0$ is assumed at different energies to simulate an empty loss cone, where α_{LC} is maximum equatorial pitch angle within the loss cone. At the higher pitch angle boundary, we assume $\frac{\partial f}{\partial\alpha}|_{\alpha=0^{\circ}} = 0$ following the previous studies.

For simplicity, the initial PSD distribution of the electrons are modeled using a kappa distribution with the kappa index $\kappa = 6$ following the study by *Xiao et al.*

[2008]:

$$f(\alpha, p) = (1 + \frac{p^2}{\kappa\theta^2})^{-(\kappa+1)} \sin\alpha, \tag{6.21}$$

where θ is the effective thermal parameter scaled by the electron rest-mass and is set as $\theta^2 = 0.15$. The PSD values are normalized and do not contain units.

Figure 6.9 presents the four day simulation of the electron PSD evolution at $L = 4.5$ by magnetosonic waves under disturbed conditions. The PSD at different energies are shown as a function of electron equatorial pitch angle. The scattering effects of magnetosonic waves are small in a time scale of several hours. However, the electron PSD at pitch angles between 50° and 80° increases and the PSD at higher pitch angles decreases after several days, forming the butterfly distributions at energies of hundreds of keV. It is worth noting that the analytical formula for diffusion coefficients calculations may be not valid at extremely high pitch angles due to the assumptions, therefore the lack of magnetosonic wave scattering near 90° may be not valid. The magnetosonic waves can scatter the electrons with a extremely high pitch angles by bounce resonance interactions [e.g., *Maldonado and Chen*, 2014; *Shprits and Schulz*, 2014], but that is out of the scope of our current study. The simulation demonstrates that intense magnetosonic waves may be an important factor for the formation of the observed butterfly distribution of energetic electrons in absent of other wave effects. A careful examination on the electron evolution shows that the electron PSD increase occurs earlier at higher pitch angles, and the particles are subsequently transported from higher pitch angles and lower energies towards lower pitch angles and higher energies. The PSD evolution character is consistent with the scenario of electron acceleration by Landau resonance, which mainly increases the parallel velocity of the electrons.

6.7 Electron PSD evolutions due to magnetosonic waves inside the plasmapause

For the completeness of the electron scattering evaluations, we also perform a similar analysis and simulation for the electron PSD evolution inside the plasmapause, although the effects of magnetosonic waves are expected to be weaker than outside the plasmapause. For comparison with the simulations outside the plasmapause, we perform the simulation at $L = 4.5$, and choose the wave amplitudes as 75 pT near the dayside and 25 pT near the nightside. The total plasma density is calculated using Sheeley's density model in the plasmasphere [*Sheeley et al.*, 2001]. The other model parameters and simulation inputs are the same as the parameters in Section 6.6.

The pitch angle, momentum, and mixed pitch angle-momentum diffusion coefficients are presented as a function of electron equatorial pitch angle and energy Figure 6.10. The electron scattering is limited within a narrower and higher pitch angle range inside the plasmapause due to the higher ratio of f_{pe}/f_{ce}, although the peak diffusion rates are higher than the scattering outside the plasmapause. The pitch angle scattering rates become extremely weak at pitch angles below $\sim 30°$, indicating that the magnetosonic waves cannot cause precipitation loss of energetic electrons. The major energy band of effective Landau resonance is slightly lower than the energy band outside the plasmapause, but is also located within the 10 keV - 1 MeV energy range. Figure 6.11 presents the electron PSD distribution evolution in the same format as Figure 6.9. Because the electron energization is only effective within a narrow pitch angle band, the electron PSD distribution is only slightly scattered in a time scale of four days. The magnetosonic waves cannot effectively transport electrons from lower energies and higher pitch angles towards higher energies and lower pitch angles. The energization of electrons by RMS averaged magnetosonic waves is inefficient in the plasmasphere.

6.8 Summary

The electron scattering effects due to typical magnetosonic waves in the Earth's radiation belts are analyzed in this chapter. Using the recent Van Allen Probes wave data products, we have performed a new statistical study about the global distribution of magnetosonic waves in the Earth's inner magnetosphere. The two years survey of wave frequency spectra is also obtained from the Van Allen Probes statistics. The analytical formula for electron scattering analysis provide a time efficient and accurate means to evaluate the scattering rates due to Landau resonance and transit-time effects of magnetosonic waves. The diffusion rates matrix of magnetosonic waves at different locations and under different conditions are calculated, and the simulations of the electron PSD evolution during the interactions with magnetosonic waves are performed inside and outside the plasmapause.

Our studies are summarized into the following points. (1) The global distribution of magnetosonic waves based on the Van Allen Probes survey shows similar characters with the previous THEMIS survey, but the wave intensities are higher during the recent two years than the period 2010 - 2012. (2) The wave frequency spectrum statistics present different properties between outside and inside the plasmapause, and the wave frequency spectra more closely follow the radial variation of f_{LHR} outside the plasmapause. (3) The magnetosonic waves mainly scatter electrons via Landau resonance, and the transit-time effects cause additional electron scatterings in much broader pitch angle ranges. (4) During modestly disturbed conditions, the magnetosonic waves can cause electron acceleration in hundreds of keV energy range in a time scale of tens of days, which is not as efficient as whistler-mode chorus waves. (5) During disturbed conditions, the RMS averaged magnetosonic waves may cause the butterfly distributions of the energetic electrons outside the plasmapause in a time scale of several days. (6) The electrons are mainly accelerated via Landau resonance, therefore the lower

energy and higher pitch angle electron populations are transported into higher energy and lower pitch angle regime during the interactions with magnetosonic waves. (7) The magnetosonic waves cannot cause the precipitation of energetic electrons. (8) In general, the electron acceleration due to magnetosonic waves are inefficient compared with the electron heating by whistler-mode chorus.

Our simulations show that the intense magnetosonic waves may potentially account for the formation of butterfly distribution of hundreds keV electrons in the inner magnetosphere. Extremely strong magnetosonic wave events with an amplitude of several nT are occasionally detected by the recent spacecraft in the Earth's radiation belts [e.g., *Zhou et al.*, 2014]. The extremely strong magnetosonic waves are expected to efficiently cause the electron acceleration and form the butterfly distribution in a short time scale of several minutes to hours. Magnetosonic waves can also interact with energetic protons in the inner magnetosphere. The magnetosonic waves are excited by the proton ion ring distributions, and the waves may also cause the energy diffusion of the protons, which results in smoothing the proton PSD profile and eliminating the positive gradients in proton PSD distribution as a function of energy. Magnetosonic waves may also cause the pitch angle scattering of the protons. The recent study by *Xiao et al.* [2014] shows that the magnetosonic waves cause the precipitation loss of plasma sheet protons and provide an explanation for the proton aurora generation. The interaction between magnetosonic waves and protons in the radiation belts would be interesting and will be addressed in future studies. This chapter provides information about the roles of magnetosonic waves in the radiation belts and references for incorporating magnetosonic waves in the future radiation belt modeling.

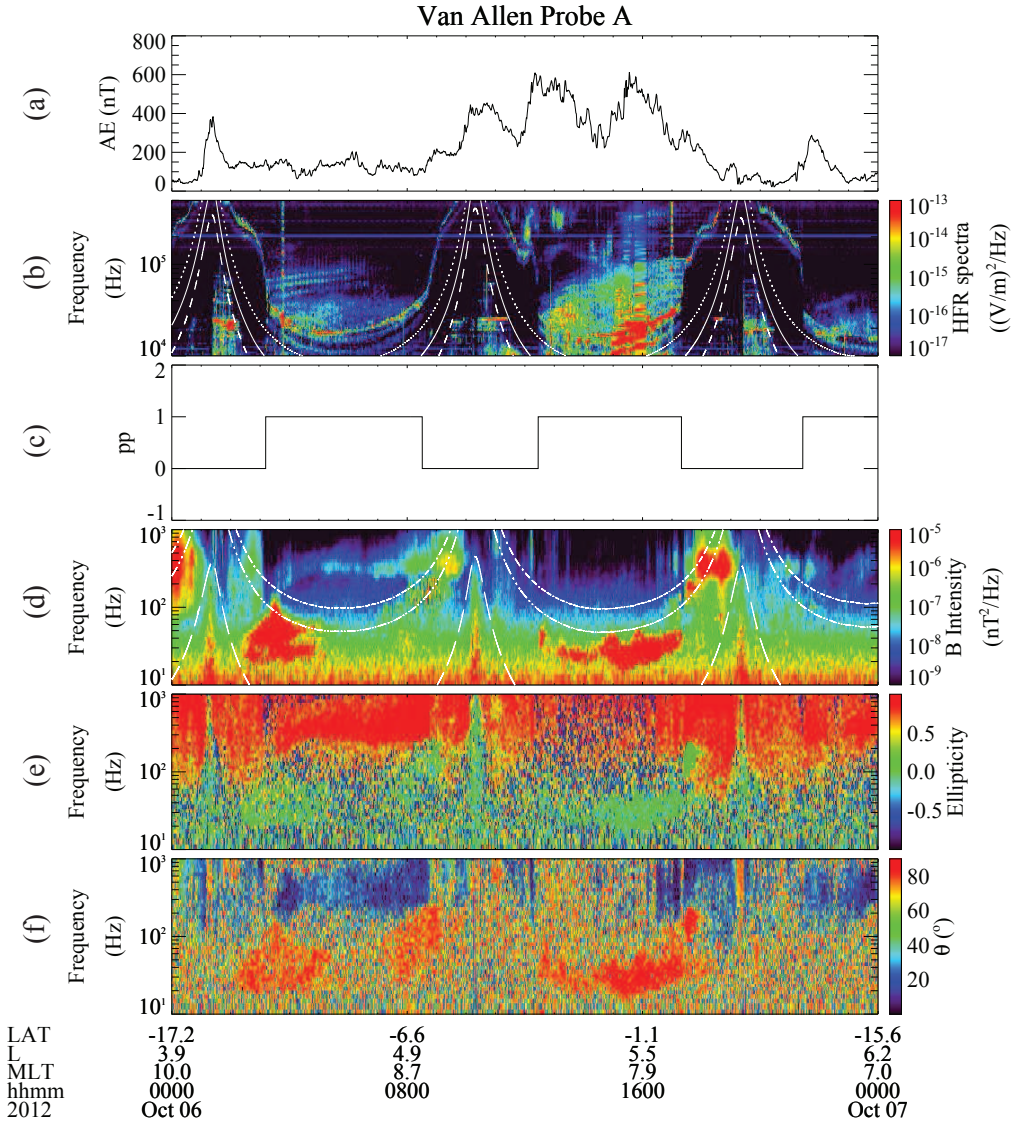

Figure 6.1: The Van Allen Probes observation of magnetosonic waves on 06 October 2012. (a) The AE index; (b) the electric field power spectral density measured by HFR; (c) the plasmapause indicator inferred from ECH wave intensities; (d) the magnetic field power spectral density measured by WFR; (e) the wave ellipticity; (f) the wave normal angle. The dotted, solid, and dashed lines in panel (b) represent $2f_{ce}$, f_{ce}, and $0.5f_{ce}$; the white dashed lines in panel (d) represent f_{LHR}, $0.5f_{LHR}$, and f_{cp}, respectively.

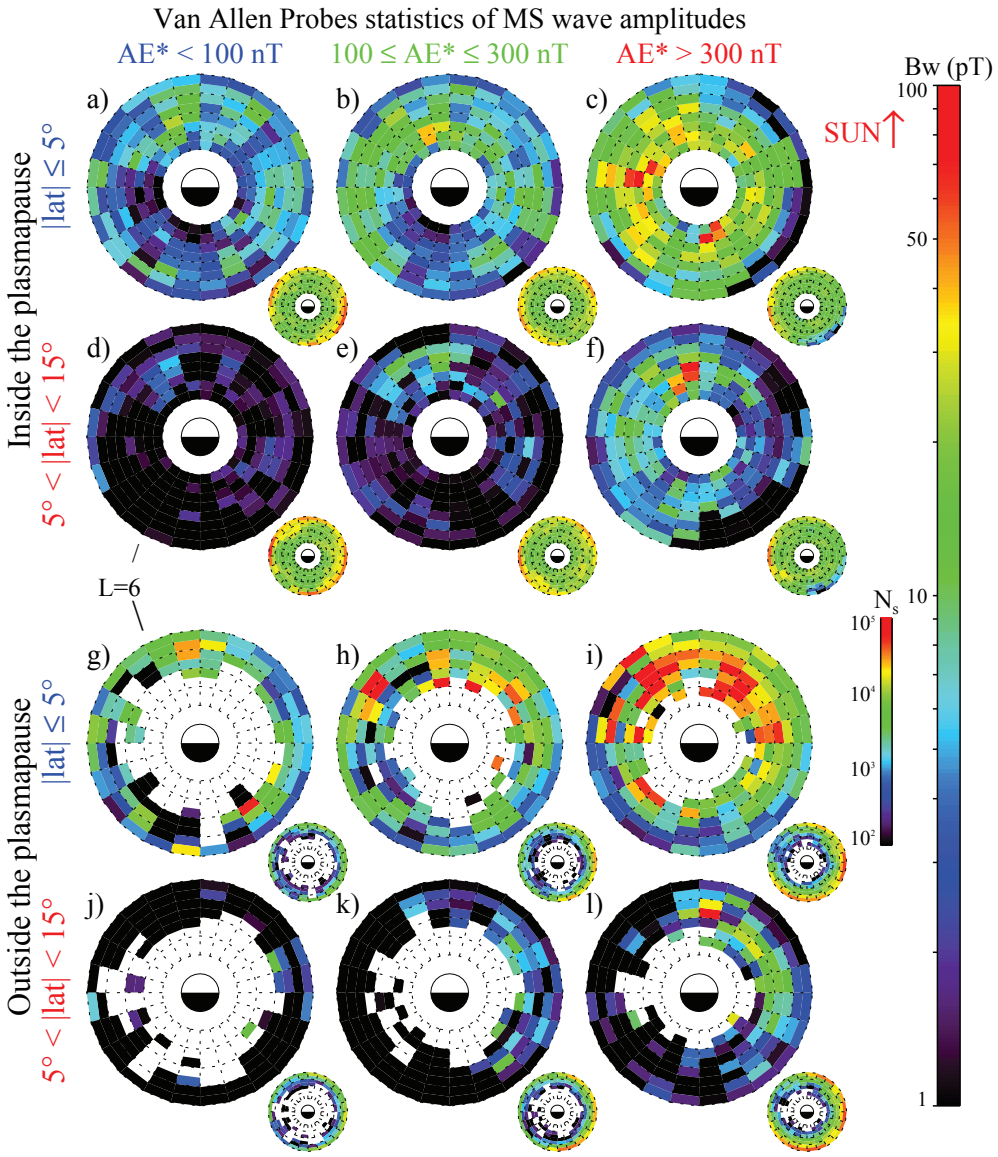

Figure 6.2: The global distribution of RMS wave amplitude B_w for $2 < L < 8$. The wave intensity is categorized by magnetic latitude and AE*, and shown for locations inside (top panels) and outside (bottom panels) the plasmapause. The sample number (N_s) is shown as smaller plots at the right bottom corner for each panel. White area represents the region where N_s is less than 100.

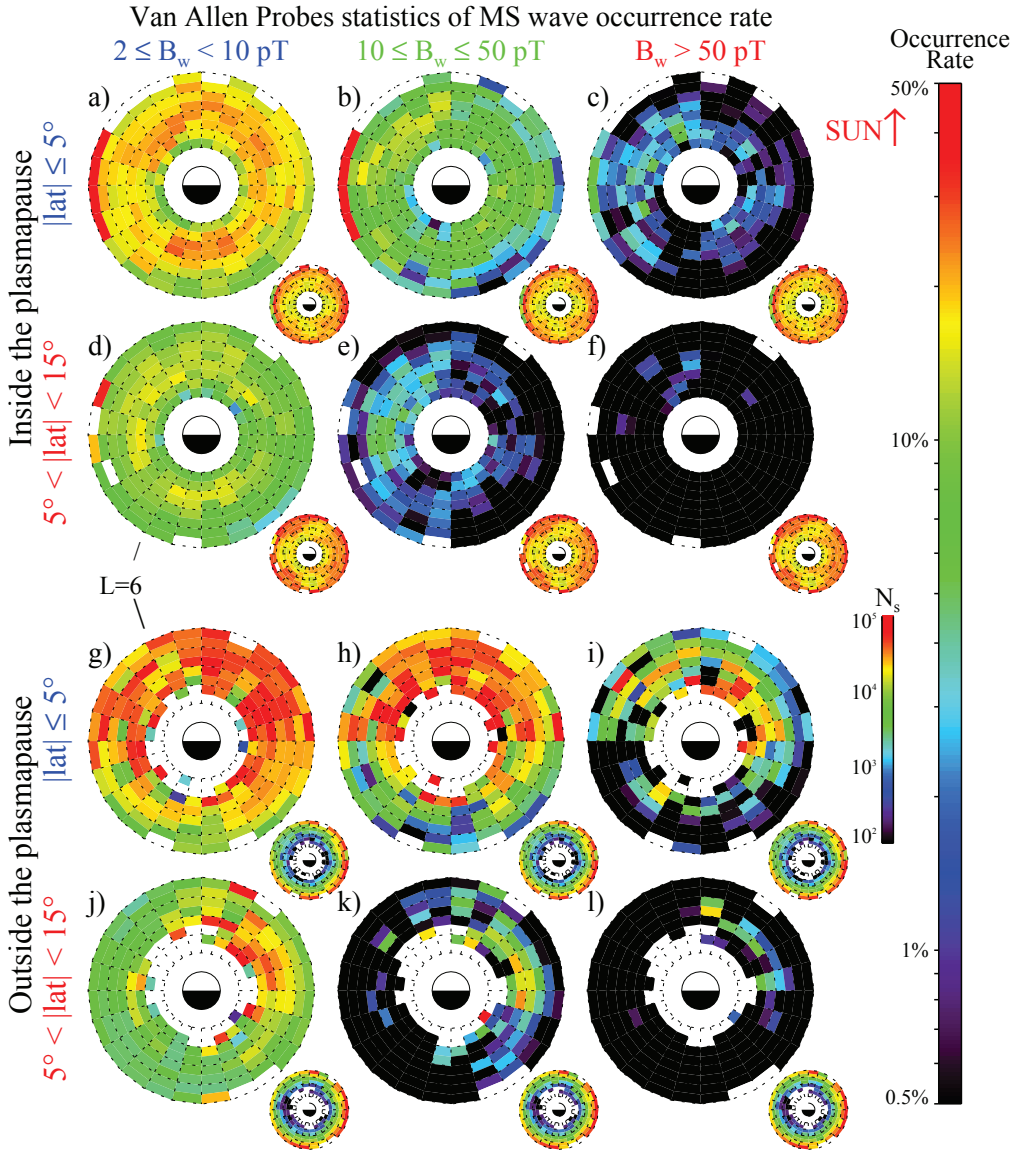

Figure 6.3: The global distribution of magnetosonic wave occurrence rate for $2 < L < 8$. The wave occurrence rate is categorized by magnetic latitude and wave amplitude range, and shown for locations inside (top panels) and outside (bottom panels) the plasmapause. The sample number is shown as smaller plots at the right bottom corner for each panel. White area represents the region where N_s is less than 100.

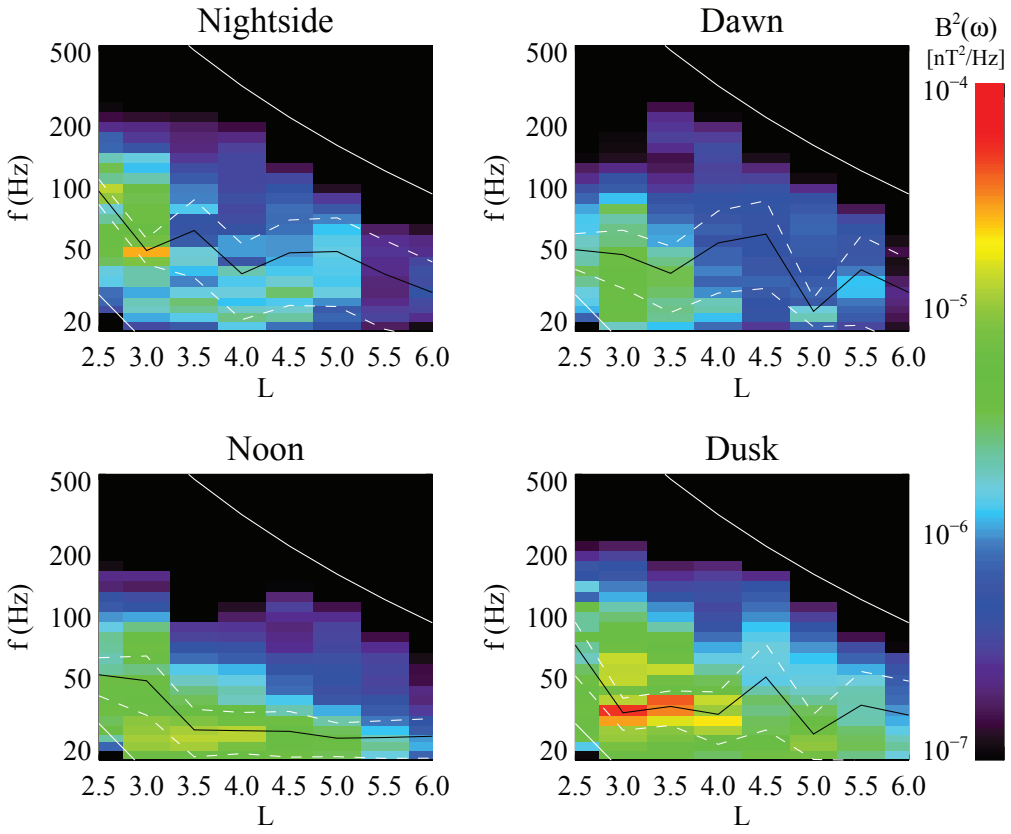

Figure 6.4: The survey of magnetosonic wave magnetic field power intensity inside the plasmapause, as a function of wave frequency at different L shells and different magnetic local time sectors. The two white solid lines represent f_{LHR} and f_{cp}; the black solid line represents the frequency with peak wave intensity; the two dashed lines represent the standard derivations of the wave power.

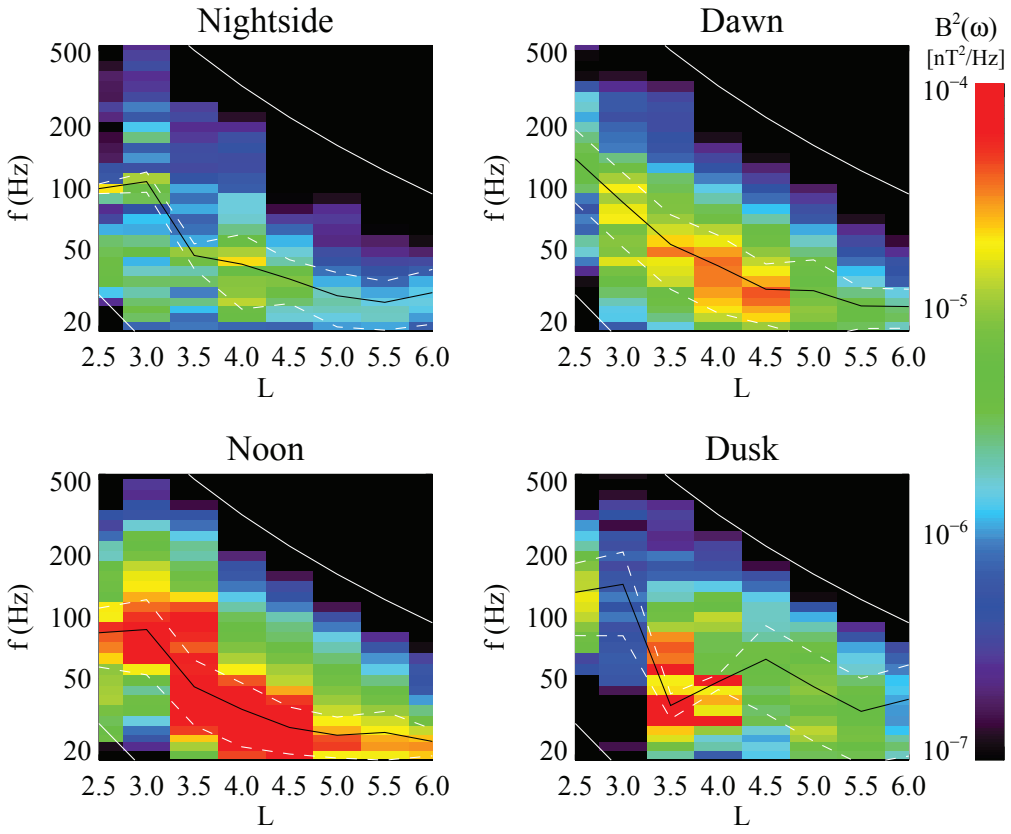

Figure 6.5: The survey of magnetosonic wave magnetic field power intensity outside the plasmapause, as a function of wave frequency at different L shells and different magnetic local time sectors. The two white solid lines represent f_{LHR} and f_{cp}; the black solid line represents the frequency with peak wave intensity; the two dashed lines represent the standard derivations of the wave power.

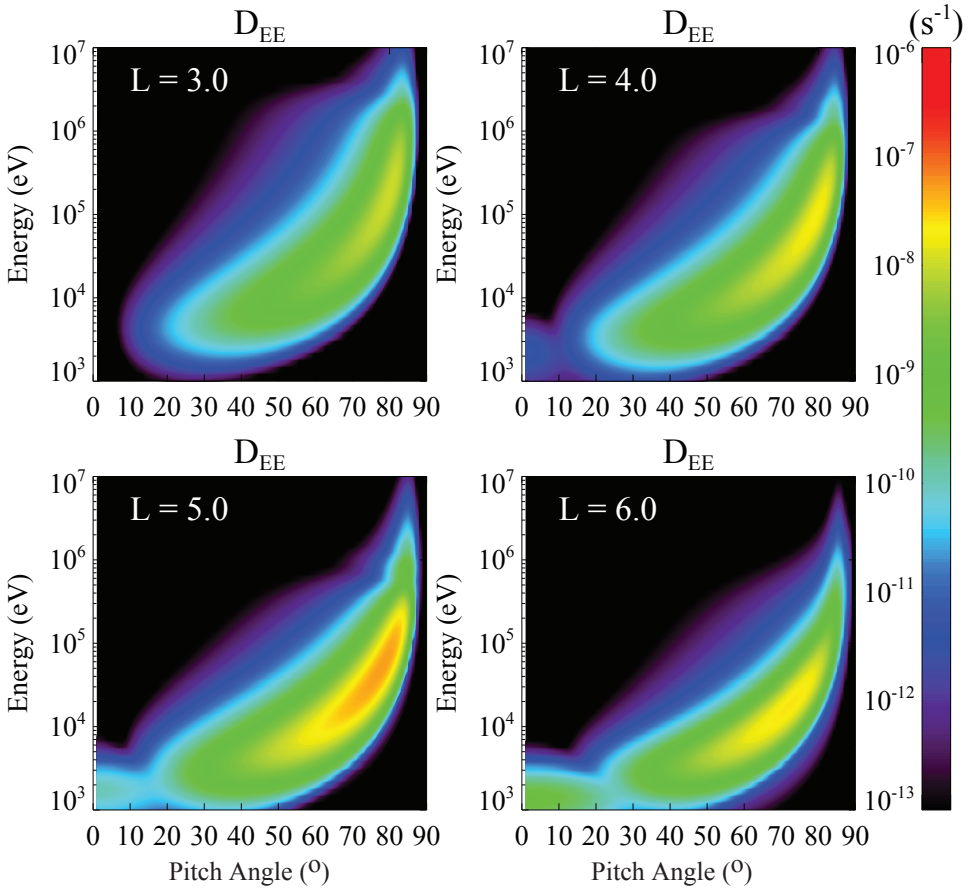

Figure 6.6: The calculated energy diffusion coefficients due to magnetosonic waves as a function of pitch angle and energy inside the plasmapause, at different L shells from $L = 3$ to $L = 6$. The statistical wave frequency spectra and the wave amplitudes inside the plasmapause during modestly disturbed conditions are used. The density model is Sheeley's density model inside the plasmapause [*Sheeley et al.*, 2001]. The energy diffusion coefficients are drift and bounce averaged.

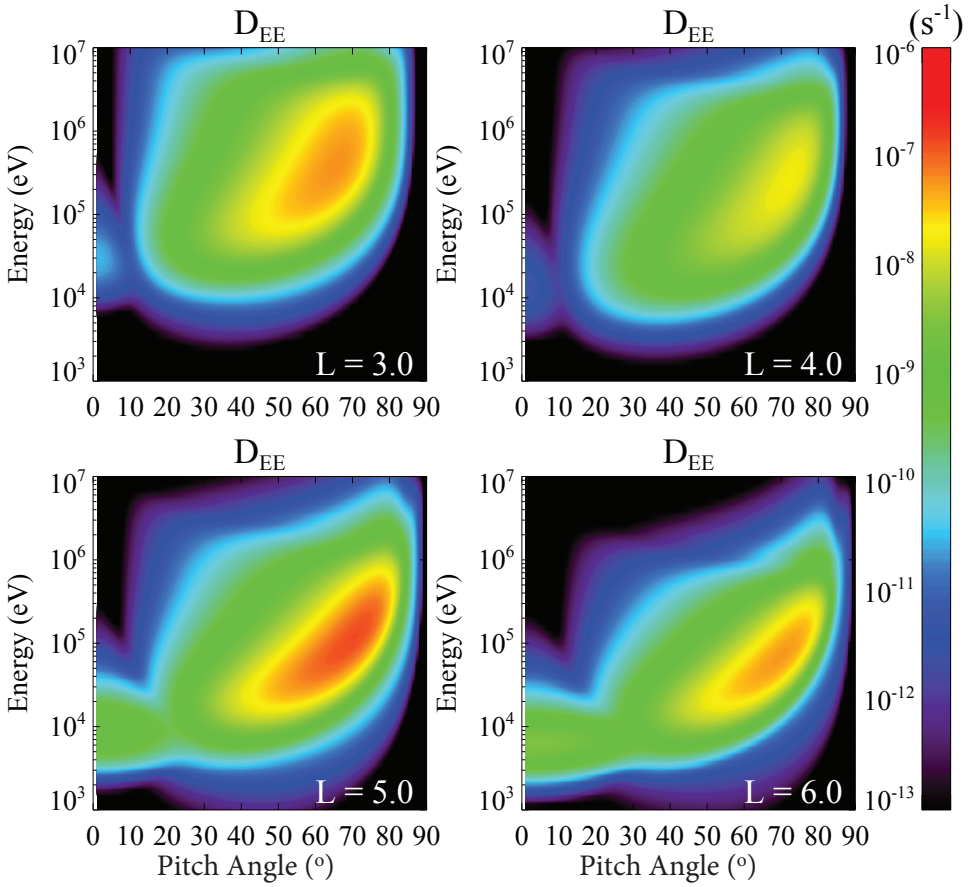

Figure 6.7: The calculated energy diffusion coefficients due to magnetosonic waves as a function of pitch angle and energy outside the plasmapause, at different L shells from $L = 3$ to $L = 6$. The statistical wave frequency spectra and the wave amplitudes outside the plasmapause during modestly disturbed conditions are used. The density model is Sheeley's density model outside the plasmapause [*Sheeley et al.*, 2001]. The energy diffusion coefficients are drift and bounce averaged.

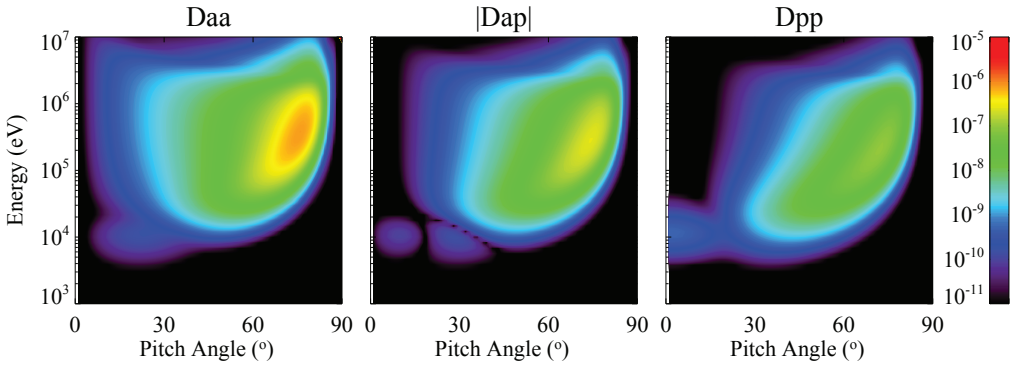

Figure 6.8: The pitch angle, absolute values of mixed pitch angle-momentum, and momentum diffusion coefficients as a function of pitch angle and energy calculated at $L = 4.5$ outside the plasmapause during disturbed conditions. Most of the mixed pitch angle-momentum diffusion coefficients are negative. The diffusion coefficients are drift and bounce averaged.

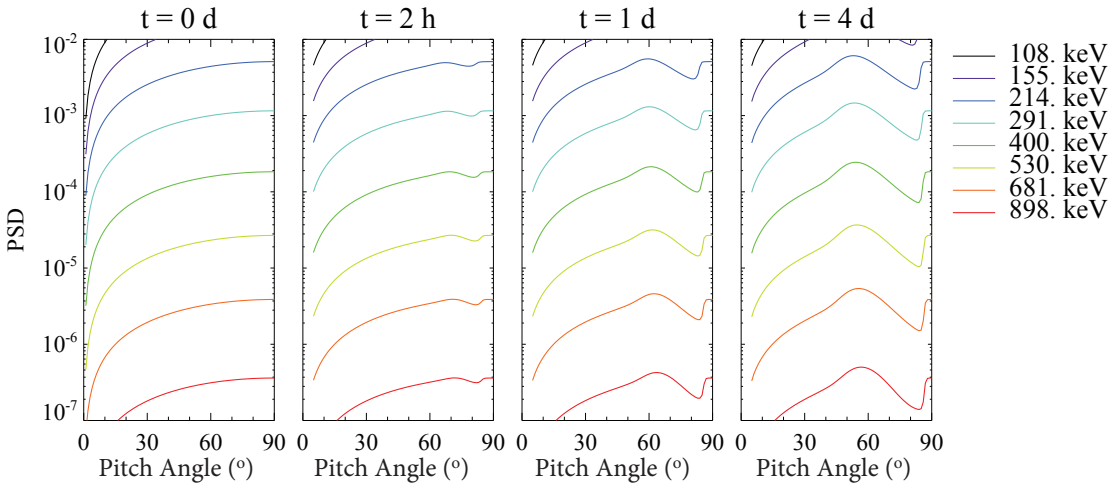

Figure 6.9: The 2D Fokker-Planck simulation of the energetic electron PSD evolution due to the interactions with magnetosonic waves during disturbed conditions outside the plasmapause, for a period of 4 days. The electron PSD are plotted as a function of pitch angle at different energies. The diffusion coefficients in Figure 6.8 are used. The initial electron PSD distributions are normalized and assumed to be Kappa distribution with $\kappa = 6$.

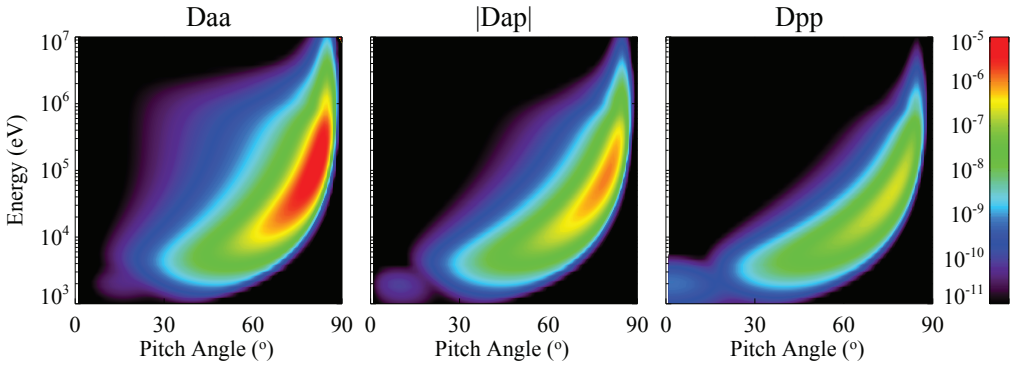

Figure 6.10: The pitch angle, absolute values of mixed pitch angle-momentum, and momentum diffusion coefficients as a function of pitch angle and energy calculated at $L = 4.5$ inside the plasmapause during disturbed conditions. Most of the mixed pitch angle-momentum diffusion coefficients are negative. The diffusion coefficients are drift and bounce averaged.

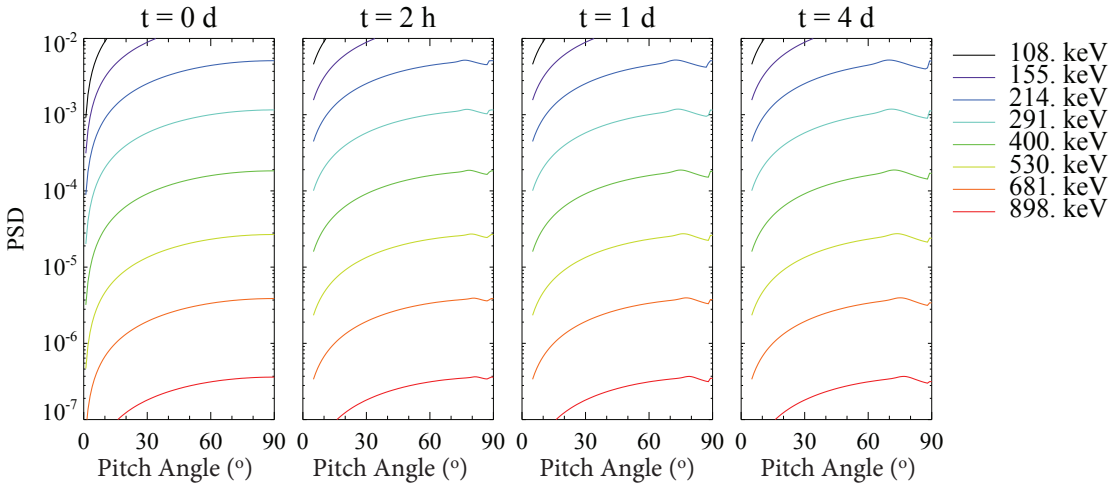

Figure 6.11: The 2D Fokker-Planck simulation of the energetic electron PSD evolution due to the interactions with magnetosonic waves during disturbed conditions inside the plasmapause, for a period of 4 days. The electron PSD are plotted as a function of pitch angle at different energies. The diffusion coefficients in Figure 6.10 are used. The initial electron PSD distributions are normalized and assumed to be Kappa distribution with $\kappa = 6$.

CHAPTER 7

Summary and Future Works

7.1 Summary

In this thesis, we have performed a comprehensive study about the equatorial magnetosonic waves in the Earth's inner magnetosphere. The global distribution, excitation mechanism, propagation properties, and electron scattering effects of magnetosonic waves have been investigated both in the plasmasphere and the plasmatrough. As the significant roles of various plasma waves in the Earth's radiation belts have been confirmed by both observational evidences and theory developments, our studies provide a more complete understanding about the magnetosonic waves and provide references for future researches on the radiation belt dynamics.

Chapter 1 is a brief introduction about the Earth's inner magnetosphere, with a focus on the important plasma wave distributions and properties, particle motions, and the particle diffusion dynamics in the radiation belts.

In Chapter 2 we have derived the dispersion relations and polarization properties of fast magnetosonic waves. The magnetosonic waves are highly oblique electromagnetic emissions at frequencies between the proton gyrofrequency (f_{cp}) and the lower hybrid resonance frequency (f_{LHR}). The waves are nearly linearly polarized, the wave electric field perturbations are mostly longitudinal, and the wave magnetic field perturbations are mostly compressional. The waves propagate nearly perpendicular to the background magnetic field.

In Chapter 3 we have performed a statistical survey about the magnetosonic wave distributions observed by THEMIS. The oblique magnetosonic waves and the ion differential energy flux are measured by THEMIS both inside and outside the plasmapause. We have used THEMIS fff wave data products from May 2010 to November 2012 to obtain the global distribution of magnetosonic wave amplitudes at different locations and under different conditions. The strongest magnetosonic waves are mainly observed between 3 R_E and 5 R_E, near the dayside, outside the plasmapause, near the geomagnetic equator, and during disturbed conditions. The waves inside the plasmapause present a more uniform distribution in different L shells and magnetic local times (MLT), while the dayside magnetosonic waves are much stronger than the nightside waves outside the plasmapause. The magnetosonic waves tend to present constant frequency bands inside the plasmapause, while the wave frequency band varies with the trend of f_{LHR} outside the plasmapause, which implies different properties in wave local excitation and propagation effects. The majority of magnetosonic wave power is contained within the lower frequency band below $0.5f_{LHR}$ under different categorizations. The strong magnetosonic waves with wave amplitude higher than 50 pT are mostly observed near the dayside outside the plasmapause, with an occurrence rate of $\sim 30\%$, implying that the magnetosonic waves may have potential roles in particle scattering in the radiation belts.

The local excitation of magnetosonic wave by ion ring distributions in the Earth's inner magnetosphere is analyzed in Chapter 4. A typical magnetosonic wave event in association with the simultaneous ion ring distributions is observed by the THEMIS spacecraft. Outside the plasmapause, the ion ring distributions with a peak ion energy (E_R) slightly lower than the local Alfven energy (E_A) provide free energy for the excitation of magnetosonic waves in higher and narrower frequency band. Near the edge of the plasmapause boundary, the ion ring distributions with E_R slightly higher than E_A provide free energy for the wave

excitation in lower and broader frequency band. Deep inside the plasmapause, although the ion ring distribution is still present, E_R is much larger than E_A, and the excitation of magnetosonic wave becomes extremely inefficient. In addition, the magnetosonic waves have nearly constant frequency band over a large radial distance inside the plasmapause, indicating that the waves may originate from a source near the plasmapause boundary. The waves are mostly excited at highly oblique wave normal angles, and the wave growth rates and the unstable frequency bands are dependent on the wave normal angle. The wave growth rates also depend on the background magnetic field and the total plasmapause density. We have also simulated the broad frequency band magnetosonic waves outside the plasmapause with E_R slightly larger than E_A. Our simulation of the wave growth rates as a function of frequency at different locations agrees fairly well with the observed wave power spectrum, demonstrating that the ion ring distributions efficiently excite magnetosonic waves outside the plasmapause and near the plasmapause boundary.

In Chapter 5 we have analyzed the perpendicular propagation of equatorial magnetosonic waves, to provide an illustration of the wide existence of magnetosonic waves in the plasmasphere. We have studied an intense magnetosonic wave event in association with the ion energy flux distributions observed by the Van Allen Probes in the plasmasphere. The observed ion ring distributions provide free energy for magnetosonic wave excitation near the plasmapause boundary, but the wave growth rates become small when the spacecraft is deeper inside the plasmasphere with $E_A \ll E_R$. However, the magnetosonic waves are observed in a much larger radial extent. Based on a simple wave perpendicular propagation model, the magnetosonic waves may become trapped within a trapping region in the plasmasphere, which is determined by the profile of Q. We have calculated the Q values at different wave frequencies, and confirmed the existence of a trapping region for the wave trajectories. In addition, the calculated trapping region agrees

fairly well with the observed radial extent of the magnetosonic waves at various frequencies. Therefore, the waves are excited near the plasmapause boundary in the plasmasphere, subsequently propagate in the perpendicular direction with respect to the background magnetic field, and become trapped within a limited radial distance. We have also analyzed the magnetosonic waves modulated by the plasmaspheric density structures in the plasmasphere. We have demonstrated that the magnetosonic waves are trapped by the local density structures in agreement with observations. The wave trapping is an important factor in controlling the wave distributions in the plasmasphere.

We have studied the general particle scattering effects due to statistical magnetosonic waves at different locations in Chapter 6. The statistical survey of the magnetosonic waves distribution using the recent Van Allen Probes wave data products shows similar characters with the THEMIS survey, and the strongest magnetosonic waves have an averaged amplitude of 50 - 100 pT near the dayside outside the plasmapause. The statistical wave frequency spectra shows different properties between inside and outside the plasmapause. The wave diffusion coefficients are evaluated using the analytical approximation of the electron's motion when streaming through the magnetosonic waves in the vicinity of the Earth's magnetic equator. The electrons are scattered by Landau resonance and transit-time effects. The energy diffusion coefficients calculations show that the magnetosonic waves mainly cause the electron acceleration at pitch angles from 50° to 70°, energies of hundreds of keV, and around $L = 5$ outside the plasmapause. The time scale of electron energization is tens of days during modestly disturbed conditions, which is slower than the typical time scale of electron acceleration due to chorus waves. We also performed a 2D Fokker-Planck simulation on the evolution of energetic electron phase space density (PSD) distributions during disturbed conditions for a time scale of four days. The electrons at higher pitch angles (higher than 80°) and lower energies ($\sim 100keV$) are accelerated into lower

pitch angles ($\sim 50°$) and higher energies (hundreds of keV) ranges, due to the Landau resonance effects. The magnetosonic waves can cause the typical butterfly distribution of electrons in the radiation belts. The wave scattering inside the plasmapause is much less efficient than the scattering outside the plasmapause, because of the much narrower scattering rates as a function of pitch angle.

7.2 Future works

We will investigate other interesting features of equatorial magnetosonic waves as our future works, with three promising projects listed in this section.

7.2.1 The rising tone structures of magnetosonic waves

The rising tone structures of fast magnetosonic waves have been recently reported by *Fu et al.* [2014] using THEMIS wave data products. The authors have shown that the magnetosonic waves have discrete wave elements with rising tone features in both electric and magnetic power spectrograms, with a frequency sweep rate of ~ 1 Hz/s. Most of the rising tone structures are observed outside the plasmapause in association with the ion ring distributions, and the waves generally cannot penetrate the plasmapause boundary.

The rising tone structures of chorus waves is widely known and probably due to the non-linear interactions with the an-isotropic electrons [e.g., *Cully et al.*, 2011; *Tao*, 2014]. The rising tone structure of magnetosonic waves is a new topic and its formation is not clear yet. Since the fast magnetosonic waves are excited by the ion ring distributions, and the linear wave growth simulation agrees fairly well with the long period observations, the rising tones of magnetosonic waves may be related to some non-linear interactions with the proton source. Another probable source of the rising tone feature is the wave propagation effect [e.g., *Boardsen et al.*, 2014]. Since the wave phase speed is different for different frequency band

magnetosonic waves, the rising tone feature may form when the waves propagate away from the energy source. This still requires that the periodic magnetosonic waves are generated at the source region, but the modulations in plasma density, background magnetic field, or the ion ring distributions are generally not observed. The theory approach and numerical simulation works would help our physical understanding about the source of the rising tone features of magnetosonic waves.

A survey of the rising tone structures of magnetosonic waves will provide important information about the conditions and preferred locations for rising tone generation. The rising tone structures are occasionally observed by the WFR instruments on-board the Van Allen Probes. Figure 7.1 shows an example of the rising tone event. The high frequency wave measurements from HFR instrument indicate that the spacecraft is located outside the plasmapause before 07:15 UT. The PSD measurements show a clear ion ring distribution with a peak in PSD at energies between 10 keV and 20 keV. The observed ion ring distribution is potentially important for magnetosonic wave excitation. The rising tone magnetosonic waves are continuously observed for more than one hour outside the plasmapause in both wave electric field and wave magnetic field measurements. The waves are classified as magnetosonic waves because they are highly oblique with wave normal angles higher than 80°. With high time and frequency resolutions, the Van Allen Probes provide ideal observation on the occurrence of the structures, and each wave elements are clearly observed and well separated without interference. The statistical study about the occurrence of the rising tone structures under different conditions would be useful in studying the general features of the fine structure magnetosonic waves.

7.2.2 The relation between magnetosonic waves and proton distributions

We have demonstrated that the magnetosonic wave distributions are closely related to the proton distributions in Chapter 4. The magnetosnic waves are excited by the ion ring distributions when the ion ring energy is close to the Alfven energy. Our simulations have shown that this condition is typically satisfied outside the plasmapause or near the plasmapause boundary. However, a statistical study about the ion ring distributions that are potentially capable of efficiently excite magnetosonic waves would be another interesting topic. Using the particle data from CRRES spacecraft, *Meredith et al.* [2008] have performed a survey of the proton ring distributions and compared with the global distribution of magnetosonic waves. The proton rings present similar characters with the distributions of magnetosonic waves. However, the data coverage of CRRES spacecraft is limited, especially near the dayside of the inner magnetosphere where the occurrence rates of magnetosonic waves are expected to be high. The recent equatorial spacecraft THEMIS and the Van Allen Probes are equipped with high resolution plasma wave and particle measurement instruments. After several years of operation, the spacecraft provide excellent coverage for a statistical study of the magnetosonic waves and the associated particle distributions. It will be interesting to perform a survey of the ion ring distributions, and specially focus on the ion ring distributions satisfying the condition that E_R is close to E_A. The similarity between the ion ring distributions and the magnetosonic waves will be another evidence that the source of magnetosonic waves is closely related with the drifting of the ions and the formation of the positive slopes in ion PSD distributions as a function of ion energy. In addition, since the magnetosonic waves with different properties are excited when the relation between E_R and E_A varies, this study will provide information about the magnetosonic wave frequency and other properties based on the ion ring distributions. The statistical studies about the ion ring distribu-

tions will also provide the information about the occurrence of the magnetosonic waves. Since the spacecraft measurements are generally limited especially in MLT for the events study about the magnetosonic waves, using the simulated ring current distributions and the empirical relation between the ion ring distributions and the magnetosonic waves from the statistical surveys, the global distribution of magnetosonic waves can be inferred during specific wave events. The reconstructed global distribution of magnetosonic waves is useful for the simulations in the radiation belt dynamics.

The electron scattering effects of magnetosonic waves are investigated in Chapter 5. Our studies have shown that the electron scattering due to magnetosonic waves are slower than other plasma wave emissions (e.g., whistler-mode chorus). However, the magnetosonic waves may efficiently interact with the proton distributions. The general effects of the magnetosonic waves on the energetic proton distributions are not clear yet and are important in the dynamics of the Earth's inner magnetosphere. The positive slopes in proton PSD distribution provide free energy for the excitation of magnetosonic waves; as a consequence, the positive gradients are expected to become flat and the normal Maxwellian or Kappa distributions are expected to form. Therefore, after being excited, the magnetosonic waves are expected to interact with the proton ring distributions and lead to the smoothing of the proton PSD profile. *Xiao et al.* [2014] have performed a simulation about the evolution of low energy plasma sheet proton distributions in the presence of magnetosonic waves. The several keV protons are effectively scattered into the loss cone and precipitate towards the Earth's atmosphere. In the meanwhile, the dayside proton aurora phenomena are observed on the Earth, demonstrating that the observed proton aurora are generated by the dayside magnetosonic waves. It would be interesting to investigate the relation between the occurrences of the ground observed proton aurora and the in-situ observed magnetosonic waves. In addition, the authors have also shown that the magnetosonic

waves cause the an-isotropic distributions of the protons in a short time scale. This may provide a source for EMIC wave generations [e.g., *Chen et al.*, 2009a,b]. The simulation of those processes would demonstrate the efficient energy transfers through the proton distributions and various plasma waves. Finally, a general study about the proton scattering effects due to magnetosonic waves using the statistical distributions would be significant in simulating the proton dynamics in the radiation belts.

7.2.3 The additional electron scattering effects due to magnetosonic waves in presence of other plasma waves

Although the electron acceleration due to statistically averaged magnetosonic waves are weaker than the whistler-mode chorus waves, the magnetosonic waves still have potentially important effects in altering the electron distributions in addition to the scattering by other plasma wave modes. Extremely strong magnetosonic waves with peak amplitudes of several nT are observed by the recent spacecraft [e.g., *Zhou et al.*, 2014]. Based on the simulation results shown in Chapter 6, the extremely strong magnetosonic waves are expected to cause the butterfly distributions of hundreds keV electrons in a short time scale. The butterfly distribution properties of energetic electrons are also observed in the slot region of the Earth's radiation belts [*Zhao et al.*, 2014]. The confirmation of the existence of magnetosonic waves and the simulation of the electron PSD distributions will confirm that the observed butterfly distributions are due to the Landau resonance by magnetosonic waves.

Whistler-mode chorus, plasmaspheric hiss, magnetosonic waves, and EMIC waves cause the formation of different pitch angle distributions of electrons. Therefore, magnetosonic waves may cause the additional scattering of electrons at some pitch angle and energy ranges where the scattering by other plasma waves are not efficient. Magnetosonic waves may cause the scattering of nearly equatori-

ally mirroring electrons via bounce resonances [*Shprits*, 2009; *Shprits and Schulz*, 2014; *Maldonado and Chen*, 2014]. In addition to the hiss wave scattering, the scattering at 90° pitch angle would remove the equatorially mirroring electrons, reducing the typical bottle neck distributions due to plasmaspheric hiss [*Ni et al.*, 2013, 2014]. It is worth noting that the magnetosonic waves are also observed at frequencies below f_{cp}. Although the magnetosonic waves cannot propagate at frequencies higher than f_{LHR}, the waves are occasionally observed to cross the frequency of local f_{cp} as the waves propagate towards the Earth in the plasmasphere. The scattering of electrons due to the highly oblique wave power below f_{cp} is not investigated yet. We plan to perform event studies about the interactions between electrons and intense magnetosonic waves under the above circumstances.

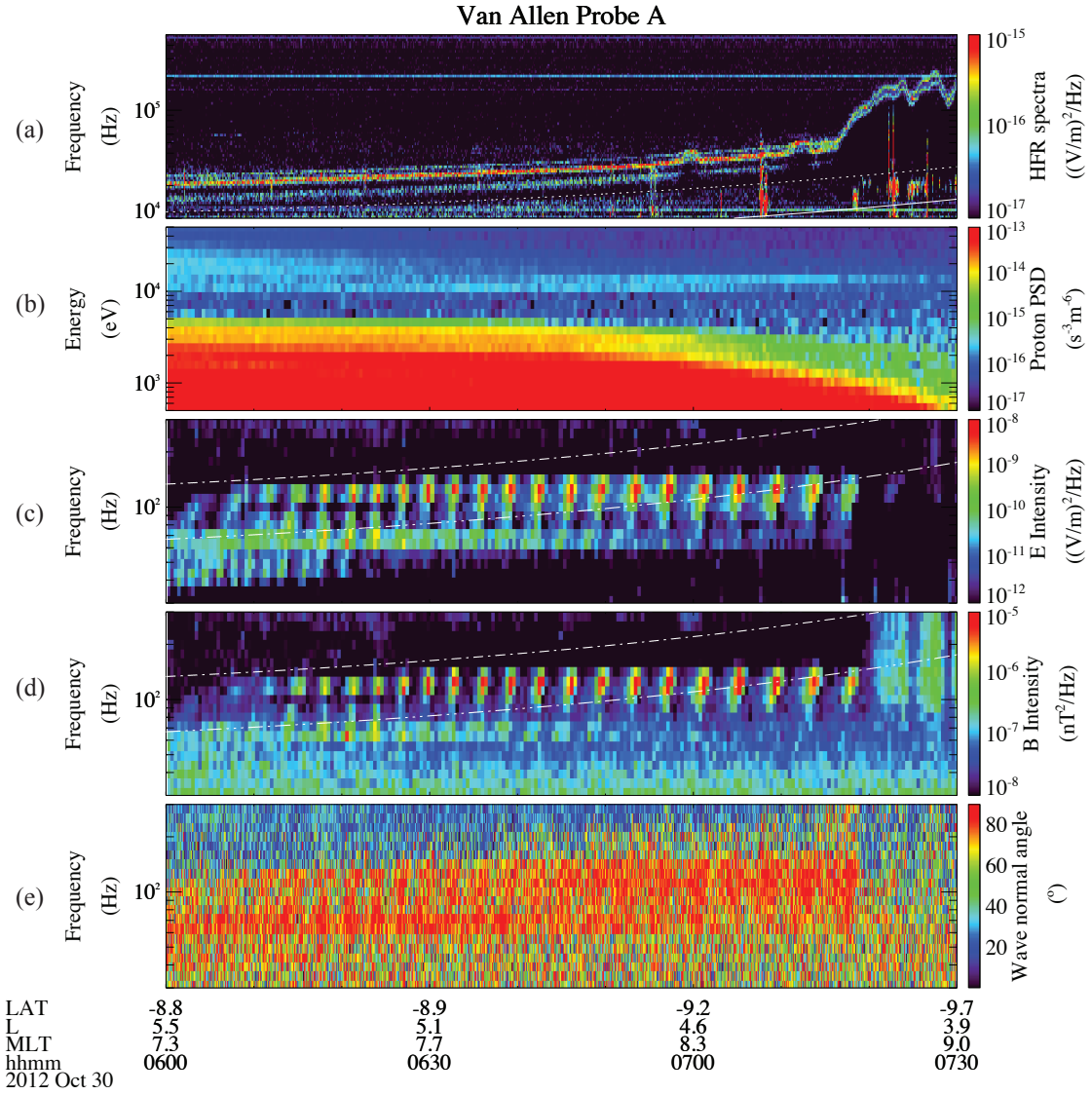

Figure 7.1: The rising tone structures of magnetosonic waves observed by the Van Allen Probes on 30 October 2012. (a) The wave electric intensity spectrogram measured by HFR; (b) the proton PSD as a function of energy at a pitch angle of 90°; (c) the wave electric field power spectral density measured by WFR; (d) the wave magnetic field power spectral density measured by WFR; (e) wave normal angle. The dashed lines in panels (c) and (d) represent f_{LHR} and $0.5f_{LHR}$, respectively.

Bibliography

Akasofu, S.-I., and Y. Kamide (1987), *The Solar Wind and the Earth*, Terra Scientific Pub. ; D. Reidel Pub.

Albert, J. M. (2003), Evaluation of quasi-linear diffusion coefficients for emic waves in a multispecies plasma, *Journal of Geophysical Research: Space Physics*, *108*(A6), doi:10.1029/2002JA009792.

Albert, J. M. (2004), Using quasi-linear diffusion to model acceleration and loss from wave-particle interactions, *Space Weather*, *2*(S09S03), doi: 10.1029/2004SW000069.

Albert, J. M. (2007), Simple approximations of quasi-linear diffusion coefficients, *Journal of Geophysical Research: Space Physics*, *112*(A12), doi: 10.1029/2007JA012551.

Albert, J. M. (2009), The coupling of quasi-linear pitch angle and energy diffusion, *Journal of Atmospheric and Solar-Terrestrial Physics*, *71*(16), 1664 – 1668, doi: http://dx.doi.org/10.1016/j.jastp.2008.11.014.

Albert, J. M., and S. L. Young (2005), Multidimensional quasi-linear diffusion of radiation belt electrons, *Geophysical Research Letters*, *32*(14), doi: 10.1029/2005GL023191.

Angelopoulos, V. (2008), The themis mission, *Space Science Reviews*, *141*(1-4), 5–34, doi:10.1007/s11214-008-9336-1.

Auster, H., K. Glassmeier, W. Magnes, O. Aydogar, W. Baumjohann, D. Constantinescu, D. Fischer, K. Fornacon, E. Georgescu, P. Harvey, O. Hillenmaier, R. Kroth, M. Ludlam, Y. Narita, R. Nakamura, K. Okrafka, F. Plaschke, I. Richter, H. Schwarzl, B. Stoll, A. Valavanoglou, and M. Wiedemann (2008),

The themis fluxgate magnetometer, *Space Science Reviews*, *141*(1-4), 235–264, doi:10.1007/s11214-008-9365-9.

Baker, D. N., S. G. Kanekal, V. C. Hoxie, M. G. Henderson, X. Li, H. E. Spence, S. R. Elkington, R. H. W. Friedel, J. Goldstein, M. K. Hudson, G. D. Reeves, R. M. Thorne, C. A. Kletzing, and S. G. Claudepierre (2013), A long-lived relativistic electron storage ring embedded in earths outer van allen belt, *Science*, *340*(6129), 186–190, doi:10.1126/science.1233518.

Baker, D. N., A. N. Jaynes, X. Li, M. G. Henderson, S. G. Kanekal, G. D. Reeves, H. E. Spence, S. G. Claudepierre, J. F. Fennell, M. K. Hudson, R. M. Thorne, J. C. Foster, P. J. Erickson, D. M. Malaspina, J. R. Wygant, A. Boyd, C. A. Kletzing, A. Drozdov, and Y. Y. Shprits (2014), Gradual diffusion and punctuated phase space density enhancements of highly relativistic electrons: Van allen probes observations, *Geophysical Research Letters*, *41*(5), 1351–1358, doi:10.1002/2013GL058942.

Bell, T. F. (1984), The nonlinear gyroresonance interaction between energetic electrons and coherent vlf waves propagating at an arbitrary angle with respect to the earth's magnetic field, *Journal of Geophysical Research: Space Physics*, *89*(A2), 905–918, doi:10.1029/JA089iA02p00905.

Boardsen, S. A., D. L. Gallagher, D. A. Gurnett, W. K. Peterson, and J. L. Green (1992), Funnel-shaped, low-frequency equatorial waves, *Journal of Geophysical Research: Space Physics*, *97*(A10), 14,967–14,976, doi:10.1029/92JA00827.

Boardsen, S. A., G. B. Hospodarsky, C. A. Kletzing, R. F. Pfaff, W. S. Kurth, J. R. Wygant, and E. A. MacDonald (2014), Van allen probe observations of periodic rising frequencies of the fast magnetosonic mode, *Geophysical Research Letters*, *41*(23), 8161–8168, doi:10.1002/2014GL062020.

Bonnell, J., F. Mozer, G. Delory, A. Hull, R. Ergun, C. Cully, V. Angelopoulos, and P. Harvey (2008), The electric field instrument (efi) for themis, *Space Science Reviews*, *141*(1-4), 303–341, doi:10.1007/s11214-008-9469-2.

Bortnik, J., and R. M. Thorne (2010), Transit time scattering of energetic electrons due to equatorially confined magnetosonic waves, *Journal of Geophysical Research: Space Physics*, *115*(A7), n/a–n/a, doi:10.1029/2010JA015283.

Bortnik, J., R. M. Thorne, and N. P. Meredith (2008), The unexpected origin of plasmaspheric hiss from discrete chorus emissions, *Nature*, *452*(7183), doi:10.1038/nature06741.

Bortnik, J., W. Li, R. M. Thorne, V. Angelopoulos, C. Cully, J. Bonnell, O. Le Contel, and A. Roux (2009), An observation linking the origin of plasmaspheric hiss to discrete chorus emissions, *Science*, *324*(5928), 775–778, doi:10.1126/science.1171273.

Bortnik, J., R. M. Thorne, B. Ni, and J. Li (2015), Analytical approximation of transit time scattering due to magnetosonic waves, *Geophysical Research Letters*, *42*(5), 1318–1325, doi:10.1002/2014GL062710.

Boyd, T., and J. Sanderson (2003), *The Physics of Plasmas*, Cambridge University Press.

Brautigam, D. H., and J. M. Albert (2000), Radial diffusion analysis of outer radiation belt electrons during the october 9, 1990, magnetic storm, *Journal of Geophysical Research: Space Physics*, *105*(A1), 291–309, doi:10.1029/1999JA900344.

Brautigam, D. H., G. P. Ginet, J. M. Albert, J. R. Wygant, D. E. Rowland, A. Ling, and J. Bass (2005), Crres electric field power spectra and radial diffusion coefficients, *Journal of Geophysical Research: Space Physics*, *110*(A2), n/a–n/a, doi:10.1029/2004JA010612.

Chang, J., and G. Cooper (1970), A practical difference scheme for fokker-planck equations, *Journal of Computational Physics*, *6*(1), 1 – 16, doi: http://dx.doi.org/10.1016/0021-9991(70)90001-X.

Chen, L., and R. M. Thorne (2012), Perpendicular propagation of magnetosonic waves, *Geophysical Research Letters*, *39*(14), doi:10.1029/2012GL052485.

Chen, L., R. M. Thorne, and R. B. Horne (2009a), Simulation of emic wave excitation in a model magnetosphere including structured high-density plumes, *Journal of Geophysical Research: Space Physics*, *114*(A7), n/a–n/a, doi: 10.1029/2009JA014204.

Chen, L., R. M. Thorne, and R. B. Horne (2009b), Simulation of emic wave excitation in a model magnetosphere including structured high-density plumes, *Journal of Geophysical Research: Space Physics*, *114*(A7), n/a–n/a, doi: 10.1029/2009JA014204.

Chen, L., R. M. Thorne, V. K. Jordanova, and R. B. Horne (2010), Global simulation of magnetosonic wave instability in the storm time magnetosphere, *Journal of Geophysical Research: Space Physics*, *115*(A11), doi:10.1029/2010JA015707.

Chen, L., R. M. Thorne, V. K. Jordanova, M. F. Thomsen, and R. B. Horne (2011), Magnetosonic wave instability analysis for proton ring distributions observed by the lanl magnetospheric plasma analyzer, *Journal of Geophysical Research: Space Physics*, *116*(A3), doi:10.1029/2010JA016068.

Chen, L., R. M. Thorne, J. Bortnik, W. Li, R. B. Horne, G. D. Reeves, C. A. Kletzing, W. S. Kurth, G. B. Hospodarsky, H. E. Spence, J. B. Blake, and J. F. Fennell (2014), Generation of unusually low frequency plasmaspheric hiss, *Geophysical Research Letters*, *41*(16), 5702–5709, doi:10.1002/2014GL060628.

Cornwall, J. M. (1972), Radial diffusion of ionized helium and protons: A probe

for magnetospheric dynamics, *Journal of Geophysical Research*, *77*(10), 1756–1770, doi:10.1029/JA077i010p01756.

Cully, C., R. Ergun, K. Stevens, A. Nammari, and J. Westfall (2008), The themis digital fields board, *Space Science Reviews*, *141*(1-4), 343–355, doi:10.1007/s11214-008-9417-1.

Cully, C. M., V. Angelopoulos, U. Auster, J. Bonnell, and O. Le Contel (2011), Observational evidence of the generation mechanism for rising-tone chorus, *Geophysical Research Letters*, *38*(1), n/a–n/a, doi:10.1029/2010GL045793.

Fennell, J. F., J. L. Roeder, W. S. Kurth, M. G. Henderson, B. A. Larsen, G. Hospodarsky, J. R. Wygant, J. S. G. Claudepierre, J. B. Blake, H. E. Spence, J. H. Clemmons, H. O. Funsten, C. A. Kletzing, and G. D. Reeves (2014), Van allen probes observations of direct wave-particle interactions, *Geophysical Research Letters*, *41*(6), 1869–1875, doi:10.1002/2013GL059165.

Foster, J. C., P. J. Erickson, D. N. Baker, S. G. Claudepierre, C. A. Kletzing, W. Kurth, G. D. Reeves, S. A. Thaller, H. E. Spence, Y. Y. Shprits, and J. R. Wygant (2014), Prompt energization of relativistic and highly relativistic electrons during a substorm interval: Van allen probes observations, *Geophysical Research Letters*, *41*(1), 20–25, doi:10.1002/2013GL058438.

Fu, H. S., J. B. Cao, Z. Zhima, Y. V. Khotyaintsev, V. Angelopoulos, O. Santolk, Y. Omura, U. Taubenschuss, L. Chen, and S. Y. Huang (2014), First observation of rising-tone magnetosonic waves, *Geophysical Research Letters*, *41*(21), 7419–7426, doi:10.1002/2014GL061867.

Funsten, H., R. Skoug, A. Guthrie, E. MacDonald, J. Baldonado, R. Harper, K. Henderson, K. Kihara, J. Lake, B. Larsen, A. Puckett, V. Vigil, R. Friedel, M. Henderson, J. Niehof, G. Reeves, M. Thomsen, J. Hanley, D. George, J.-M.

Jahn, S. Cortinas, A. De Los Santos, G. Dunn, E. Edlund, M. Ferris, M. Freeman, M. Maple, C. Nunez, T. Taylor, W. Toczynski, C. Urdiales, H. Spence, J. Cravens, L. Suther, and J. Chen (2013), Helium, oxygen, proton, and electron (hope) mass spectrometer for the radiation belt storm probes mission, *Space Science Reviews*, *179*(1-4), 423–484, doi:10.1007/s11214-013-9968-7.

Gendrin, R. (1974), Phase-bunching and other non-linear processes occurring in gyroresonant wave-particle interactions, *Astrophysics and Space Science*, *28*(1), 245–266, doi:10.1007/BF00642254.

Glauert, S. A., and R. B. Horne (2005), Calculation of pitch angle and energy diffusion coefficients with the padie code, *Journal of Geophysical Research: Space Physics*, *110*(A4), doi:10.1029/2004JA010851.

Gurnett, D. A. (1976), Plasma-wave interactions with energetic ions near magnetic equator, *Journal of Geophysical Research: Space Physics*, *81*(16), 2765–2770, doi:10.1029/JA081i016p02765.

Hamlin, D. A., R. Karplus, R. C. Vik, and K. M. Watson (1961), Mirror and azimuthal drift frequencies for geomagnetically trapped particles, *Journal of Geophysical Research*, *66*(1), 1–4, doi:10.1029/JZ066i001p00001.

Horne, R. B., and R. M. Thorne (1998), Potential waves for relativistic electron scattering and stochastic acceleration during magnetic storms, *Geophysical Research Letters*, *25*(15), 3011–3014, doi:10.1029/98GL01002.

Horne, R. B., G. V. Wheeler, and H. S. C. K. Alleyne (2000), Proton and electron heating by radially propagating fast magnetosonic waves, *Journal of Geophysical Research: Space Physics*, *105*(A12), 27,597–27,610, doi:10.1029/2000JA000018.

Horne, R. B., R. M. Thorne, S. A. Glauert, N. P. Meredith, D. Pokhotelov, and O. Santolk (2007), Electron acceleration in the van allen radiation

belts by fast magnetosonic waves, *Geophysical Research Letters*, *34*(17), doi: 10.1029/2007GL030267.

Inan, U. S., T. F. Bell, and R. A. Helliwell (1978), Nonlinear pitch angle scattering of energetic electrons by coherent vlf waves in the magnetosphere, *Journal of Geophysical Research: Space Physics*, *83*(A7), 3235–3253, doi: 10.1029/JA083iA07p03235.

Jordanova, V. K., S. Zaharia, and D. T. Welling (2010), Comparative study of ring current development using empirical, dipolar, and self-consistent magnetic field simulations, *Journal of Geophysical Research: Space Physics*, *115*(A12), doi:10.1029/2010JA015671.

Jordanova, V. K., D. T. Welling, S. G. Zaharia, L. Chen, and R. M. Thorne (2012), Modeling ring current ion and electron dynamics and plasma instabilities during a high-speed stream driven storm, *Journal of Geophysical Research: Space Physics*, *117*(A9), doi:10.1029/2011JA017433.

Kasahara, Y., H. Kenmochi, and I. Kimura (1994), Propagation characteristics of the elf emissions observed by the satellite akebono in the magnetic equatorial region, *Radio Science*, *29*(4), 751–767, doi:10.1029/94RS00445.

Kennel, C. F., and F. Engelmann (1966), Velocity space diffusion from weak plasma turbulence in a magnetic field, *Physics of Fluids*, *9*, 2377–2388, doi: 10.1063/1.1761629.

Kersten, T., R. B. Horne, S. A. Glauert, N. P. Meredith, B. J. Fraser, and R. S. Grew (2014), Electron losses from the radiation belts caused by emic waves, *Journal of Geophysical Research: Space Physics*, *119*(11), 8820–8837, doi:10.1002/2014JA020366.

Kivelson, M., and C. Russell (1995), *Introduction to Space Physics*, Cambridge atmospheric and space science series, Cambridge University Press.

Kletzing, C., W. Kurth, M. Acuna, R. MacDowall, R. Torbert, T. Averkamp, D. Bodet, S. Bounds, M. Chutter, J. Connerney, D. Crawford, J. Dolan, R. Dvorsky, G. Hospodarsky, J. Howard, V. Jordanova, R. Johnson, D. Kirchner, B. Mokrzycki, G. Needell, J. Odom, D. Mark, J. Pfaff, R., J. Phillips, C. Piker, S. Remington, D. Rowland, O. Santolik, R. Schnurr, D. Sheppard, C. Smith, R. Thorne, and J. Tyler (2013), The electric and magnetic field instrument suite and integrated science (emfisis) on rbsp, *Space Science Reviews*, *179*(1-4), 127–181, doi:10.1007/s11214-013-9993-6.

Krall, N., and A. Trivelpiece (1973), *Principles of plasma physics*, no. v. 0-911351 in International series in pure and applied physics, McGraw-Hill.

Laakso, H., H. Junginger, A. Roux, R. Schmidt, and C. de Villedary (1990), Magnetosonic waves above fc (h+) at geostationary orbit: Geos 2 results, *Journal of Geophysical Research: Space Physics*, *95*(A7), 10,609–10,621, doi:10.1029/JA095iA07p10609.

Lenchek, A. M., S. F. Singer, and R. C. Wentworth (1961), Geomagnetically trapped electrons from cosmic ray albedo neutrons, *Journal of Geophysical Research*, *66*(12), 4027–4046, doi:10.1029/JZ066i012p04027.

Li, J., B. Ni, L. Xie, Z. Pu, J. Bortnik, R. M. Thorne, L. Chen, Q. Ma, S. Fu, Q. Zong, X. Wang, C. Xiao, Z. Yao, and R. Guo (2014a), Interactions between magnetosonic waves and radiation belt electrons: Comparisons of quasi-linear calculations with test particle simulations, *Geophysical Research Letters*, *41*(14), 4828–4834, doi:10.1002/2014GL060461.

Li, W., Y. Y. Shprits, and R. M. Thorne (2007), Dynamic evolution of energetic outer zone electrons due to wave-particle interactions during storms, *Journal of Geophysical Research: Space Physics*, *112*(A10), doi:10.1029/2007JA012368.

Li, W., R. M. Thorne, V. Angelopoulos, J. Bortnik, C. M. Cully, B. Ni, O. LeContel, A. Roux, U. Auster, and W. Magnes (2009), Global distribution of whistler-mode chorus waves observed on the themis spacecraft, *Geophysical Research Letters*, *36*(9), doi:10.1029/2009GL037595.

Li, W., R. M. Thorne, J. Bortnik, Y. Nishimura, V. Angelopoulos, L. Chen, J. P. McFadden, and J. W. Bonnell (2010), Global distributions of suprathermal electrons observed on themis and potential mechanisms for access into the plasmasphere, *Journal of Geophysical Research: Space Physics*, *115*(A12), doi:10.1029/2010JA015687.

Li, W., J. Bortnik, R. M. Thorne, and V. Angelopoulos (2011), Global distribution of wave amplitudes and wave normal angles of chorus waves using themis wave observations, *Journal of Geophysical Research: Space Physics*, *116*(A12), doi:10.1029/2011JA017035.

Li, W., R. M. Thorne, J. Bortnik, G. D. Reeves, C. A. Kletzing, W. S. Kurth, G. B. Hospodarsky, H. E. Spence, J. B. Blake, J. F. Fennell, S. G. Claudepierre, J. R. Wygant, and S. A. Thaller (2013a), An unusual enhancement of low-frequency plasmaspheric hiss in the outer plasmasphere associated with substorm-injected electrons, *Geophysical Research Letters*, *40*(15), 3798–3803, doi:10.1002/grl.50787.

Li, W., R. M. Thorne, Q. Ma, B. Ni, J. Bortnik, D. N. Baker, H. E. Spence, G. D. Reeves, S. G. Kanekal, J. C. Green, C. A. Kletzing, W. S. Kurth, G. B. Hospodarsky, J. B. Blake, J. F. Fennell, and S. G. Claudepierre (2014b), Radiation belt electron acceleration by chorus waves during the 17 march 2013 storm, *Journal of Geophysical Research: Space Physics*, *119*(6), 4681–4693, doi:10.1002/2014JA019945.

Li, X., Q. Schiller, L. Blum, S. Califf, H. Zhao, W. Tu, D. L. Turner, D. Gerhardt, S. Palo, S. Kanekal, D. N. Baker, J. Fennell, J. B. Blake, M. Looper,

G. D. Reeves, and H. Spence (2013b), First results from csswe cubesat: Characteristics of relativistic electrons in the near-earth environment during the october 2012 magnetic storms, *Journal of Geophysical Research: Space Physics*, *118*(10), 6489–6499, doi:10.1002/2013JA019342.

Liu, K., S. P. Gary, and D. Winske (2011), Excitation of magnetosonic waves in the terrestrial magnetosphere: Particle-in-cell simulations, *Journal of Geophysical Research: Space Physics*, *116*(A7), doi:10.1029/2010JA016372.

Lyons, L. R. (1974a), General relations for resonant particle diffusion in pitch angle and energy, *Journal of Plasma Physics*, *12*, 45–49, doi:10.1017/S0022377800024910.

Lyons, L. R. (1974b), Pitch angle and energy diffusion coefficients from resonant interactions with ioncyclotron and whistler waves, *Journal of Plasma Physics*, *12*, 417–432, doi:10.1017/S002237780002537X.

Lyons, L. R., and R. M. Thorne (1973), Equilibrium structure of radiation belt electrons, *Journal of Geophysical Research*, *78*(13), 2142–2149, doi:10.1029/JA078i013p02142.

Lyons, L. R., and D. J. Williams (1984), *Quantitative Aspects of Magnetospheric Physics*, Springer Netherlands, doi:10.1007/978-94-017-2819-5.

Ma, C.-Y., and D. Summers (2001), A numerical scheme for fokkerplanck waveparticle interaction equations in plasmas, *Computer Physics Communications*, *135*(2), 133 – 143, doi:http://dx.doi.org/10.1016/S0010-4655(00)00224-1.

Ma, Q., B. Ni, X. Tao, and R. M. Thorne (2012), Evolution of the plasma sheet electron pitch angle distribution by whistler-mode chorus waves in non-dipole magnetic fields, *Annales Geophysicae*, *30*(4), 751–760, doi:10.5194/angeo-30-751-2012.

Ma, Q., W. Li, R. M. Thorne, and V. Angelopoulos (2013), Global distribution of equatorial magnetosonic waves observed by themis, *Geophysical Research Letters*, *40*(10), 1895–1901, doi:10.1002/grl.50434.

Ma, Q., W. Li, L. Chen, R. M. Thorne, and V. Angelopoulos (2014a), Magnetosonic wave excitation by ion ring distributions in the earth's inner magnetosphere, *Journal of Geophysical Research: Space Physics*, *119*(2), 844–852, doi:10.1002/2013JA019591.

Ma, Q., W. Li, L. Chen, R. M. Thorne, C. A. Kletzing, W. S. Kurth, G. B. Hospodarsky, G. D. Reeves, M. G. Henderson, and H. E. Spence (2014b), The trapping of equatorial magnetosonic waves in the earth's outer plasmasphere, *Geophysical Research Letters*, *41*(18), 6307–6313, doi:10.1002/2014GL061414.

Ma, Q., W. Li, R. M. Thorne, B. Ni, C. A. Kletzing, W. S. Kurth, G. B. Hospodarsky, G. D. Reeves, M. G. Henderson, H. E. Spence, D. N. Baker, J. B. Blake, J. F. Fennell, S. G. Claudepierre, and V. Angelopoulos (2015), Modeling inward diffusion and slow decay of energetic electrons in the earth's outer radiation belt, *Geophysical Research Letters*, *42*(4), 987–995, doi:10.1002/2014GL062977.

Maldonado, A., and L. Chen (2014), Investigate the effect of bounce resonance between fast magnetosonic waves and energetic electrons, *AGU Fall Meeting Abstracts*, p. A7.

Mars, R. E. (2002), Contribution of neutron beta decay to radiation belt pumping from high altitude nuclear explosion, *technical report in Lawrence Livermore National Lab.*, doi:10.2172/15004871.

Matsumoto, H., and Y. Omura (1981), Cluster and channel effect phase bunchings by whistler waves in the nonuniform geomagnetic field, *Journal of Geophysical Research: Space Physics*, *86*(A2), 779–791, doi:10.1029/JA086iA02p00779.

Mauk, B., N. Fox, S. Kanekal, R. Kessel, D. Sibeck, and A. Ukhorskiy (2013), Science objectives and rationale for the radiation belt storm probes mission, *Space Science Reviews*, *179*(1-4), 3–27, doi:10.1007/s11214-012-9908-y.

McFadden, J., C. Carlson, D. Larson, M. Ludlam, R. Abiad, B. Elliott, P. Turin, M. Marckwordt, and V. Angelopoulos (2008), The themis esa plasma instrument and in-flight calibration, *Space Science Reviews*, *141*(1-4), 277–302, doi:10.1007/s11214-008-9440-2.

Means, J. D. (1972), Use of the three-dimensional covariance matrix in analyzing the polarization properties of plane waves, *Journal of Geophysical Research*, *77*(28), 5551–5559, doi:10.1029/JA077i028p05551.

Meredith, N. P., R. B. Horne, and R. R. Anderson (2008), Survey of magnetosonic waves and proton ring distributions in the earth's inner magnetosphere, *Journal of Geophysical Research: Space Physics*, *113*(A6), doi:10.1029/2007JA012975.

Meredith, N. P., R. B. Horne, T. Kersten, B. J. Fraser, and R. S. Grew (2014), Global morphology and spectral properties of emic waves derived from crres observations, *Journal of Geophysical Research: Space Physics*, *119*(7), 5328–5342, doi:10.1002/2014JA020064.

Mourenas, D., A. V. Artemyev, O. V. Agapitov, and V. Krasnoselskikh (2013), Analytical estimates of electron quasi-linear diffusion by fast magnetosonic waves, *Journal of Geophysical Research: Space Physics*, *118*(6), 3096–3112, doi:10.1002/jgra.50349.

Nemec, F., O. Santolik, K. Gereova, E. Macusova, Y. de Conchy, and N. Cornilleau-Wehrlin (2005), Initial results of a survey of equatorial noise emissions observed by the cluster spacecraft, *Planet Space Sci.*, *53*(1-3), 291–298, doi:10.1016/j.pss.2004.09.055.

Nemec, F., O. Santolik, K. Gereova, E. Macusova, H. Laakso, Y. de Conchy, M. Maksimovic, and N. Cornilleau-Wehrlin (2006), Equatorial noise: Statistical study of its localization and the derived number density, *Adv. Space Res.*, *37*(3), 610–616, doi:10.1016/j.asr.2005.03.025.

Ni, B., R. M. Thorne, Y. Y. Shprits, and J. Bortnik (2008), Resonant scattering of plasma sheet electrons by whistler-mode chorus: Contribution to diffuse auroral precipitation, *Geophysical Research Letters*, *35*(11), doi:10.1029/2008GL034032.

Ni, B., R. M. Thorne, N. P. Meredith, R. B. Horne, and Y. Y. Shprits (2011), Resonant scattering of plasma sheet electrons leading to diffuse auroral precipitation: 2. evaluation for whistler mode chorus waves, *Journal of Geophysical Research: Space Physics*, *116*(A4), doi:10.1029/2010JA016233.

Ni, B., J. Bortnik, R. M. Thorne, Q. Ma, and L. Chen (2013), Resonant scattering and resultant pitch angle evolution of relativistic electrons by plasmaspheric hiss, *Journal of Geophysical Research: Space Physics*, *118*(12), 7740–7751, doi:10.1002/2013JA019260.

Ni, B., W. Li, R. M. Thorne, J. Bortnik, Q. Ma, L. Chen, C. A. Kletzing, W. S. Kurth, G. B. Hospodarsky, G. D. Reeves, H. E. Spence, J. Bernard Blake, J. F. Fennell, and S. G. Claudepierre (2014), Resonant scattering of energetic electrons by unusual low-frequency hiss, *Geophysical Research Letters*, *41*(6), 1854–1861, doi:10.1002/2014GL059389.

Ozeke, L. G., I. R. Mann, K. R. Murphy, I. Jonathan Rae, and D. K. Milling (2014), Analytic expressions for ulf wave radiation belt radial diffusion coefficients, *Journal of Geophysical Research: Space Physics*, *119*(3), 1587–1605, doi:10.1002/2013JA019204.

Perraut, S., A. Roux, P. Robert, R. Gendrin, J.-A. Sauvaud, J.-M. Bosqued,

G. Kremser, and A. Korth (1982), A systematic study of ulf waves above fh+ from geos 1 and 2 measurements and their relationships with proton ring distributions, *Journal of Geophysical Research: Space Physics*, *87*(A8), 6219–6236, doi:10.1029/JA087iA08p06219.

Pokhotelov, D., F. Lefeuvre, R. B. Horne, and N. Cornilleau-Wehrlin (2008), Survey of elf-vlf plasma waves in outer radiation belt observed by cluster staff-sa experiment, *Annales Geophysicae*, *26*(11), 3269–3277, doi:10.5194/angeo-26-3269-2008.

Reeves, G. D., K. L. McAdams, R. H. W. Friedel, and T. P. O'Brien (2003), Acceleration and loss of relativistic electrons during geomagnetic storms, *Geophysical Research Letters*, *30*(10), doi:10.1029/2002GL016513.

Reeves, G. D., H. E. Spence, M. G. Henderson, S. K. Morley, R. H. W. Friedel, H. O. Funsten, D. N. Baker, S. G. Kanekal, J. B. Blake, J. F. Fennell, S. G. Claudepierre, R. M. Thorne, D. L. Turner, C. A. Kletzing, W. S. Kurth, B. A. Larsen, and J. T. Niehof (2013), Electron acceleration in the heart of the van allen radiation belts, *Science*, *341*(6149), 991–994, doi:10.1126/science.1237743.

Roux, A., O. Le Contel, C. Coillot, A. Bouabdellah, B. de la Porte, D. Alison, S. Ruocco, and M. Vassal (2008), The search coil magnetometer for themis, *Space Science Reviews*, *141*(1-4), 265–275, doi:10.1007/s11214-008-9455-8.

Russell, C. T., R. E. Holzer, and E. J. Smith (1970), Ogo 3 observations of elf noise in the magnetosphere: 2. the nature of the equatorial noise, *Journal of Geophysical Research*, *75*(4), 755–768, doi:10.1029/JA075i004p00755.

Santolík, O., J. S. Pickett, D. A. Gurnett, M. Maksimovic, and N. Cornilleau-Wehrlin (2002), Spatiotemporal variability and propagation of equatorial noise observed by cluster, *Journal of Geophysical Research: Space Physics*, *107*(A12), SMP 43–1–SMP 43–8, doi:10.1029/2001JA009159.

Santolík, O., M. Parrot, and F. Lefeuvre (2003), Singular value decomposition methods for wave propagation analysis, *Radio Science*, *38*(1), doi: 10.1029/2000RS002523.

Santolík, O., F. Němec, K. Gereová, E. Macúšová, Y. de Conchy, and N. Cornilleau-Wehrlin (2004), Systematic analysis of equatorial noise below the lower hybrid frequency, *Annales Geophysicae*, *22*(7), 2587–2595, doi: 10.5194/angeo-22-2587-2004.

Schulz, M., and L. J. Lanzerotti (1974), *Particle Diffusion in the Radiation Belts*, vol. 7, Springer Berlin Heidelberg, doi:10.1007/978-3-642-65675-0.

Sheeley, B. W., M. B. Moldwin, H. K. Rassoul, and R. R. Anderson (2001), An empirical plasmasphere and trough density model: Crres observations, *Journal of Geophysical Research: Space Physics*, *106*(A11), 25,631–25,641, doi: 10.1029/2000JA000286.

Shprits, Y., and M. Schulz (2014), Bounce Resonance Scattering by Magnetosonic Waves, in *40th COSPAR Scientific Assembly*, *COSPAR Meeting*, vol. 40, p. 3048.

Shprits, Y. Y. (2009), Potential waves for pitch-angle scattering of near-equatorially mirroring energetic electrons due to the violation of the second adiabatic invariant, *Geophysical Research Letters*, *36*(12), doi: 10.1029/2009GL038322.

Shprits, Y. Y., and B. Ni (2009), Dependence of the quasi-linear scattering rates on the wave normal distribution of chorus waves, *Journal of Geophysical Research: Space Physics*, *114*(A11), doi:10.1029/2009JA014223.

Shprits, Y. Y., W. Li, and R. M. Thorne (2006), Controlling effect of the pitch angle scattering rates near the edge of the loss cone on electron lifetimes, *Journal of Geophysical Research: Space Physics*, *111*(A12), doi:10.1029/2006JA011758.

Shprits, Y. Y., S. R. Elkington, N. P. Meredith, and D. A. Subbotin (2008a), Review of modeling of losses and sources of relativistic electrons in the outer radiation belt i: Radial transport, *Journal of Atmospheric and Solar-Terrestrial Physics*, doi:10.1016/j.jastp.2008.06.008.

Shprits, Y. Y., D. A. Subbotin, N. P. Meredith, and S. R. Elkington (2008b), Review of modeling of losses and sources of relativistic electrons in the outer radiation belt ii: Local acceleration and loss, *Journal of Atmospheric and Solar-Terrestrial Physics*, doi:10.1016/j.jastp.2008.06.014.

Shprits, Y. Y., A. Runov, and B. Ni (2013), Gyro-resonant scattering of radiation belt electrons during the solar minimum by fast magnetosonic waves, *Journal of Geophysical Research: Space Physics*, *118*(2), 648–652, doi:10.1002/jgra.50108.

Spence, H., G. Reeves, D. Baker, J. Blake, M. Bolton, S. Bourdarie, A. Chan, S. Claudepierre, J. Clemmons, J. Cravens, S. Elkington, J. Fennell, R. Friedel, H. Funsten, J. Goldstein, J. Green, A. Guthrie, M. Henderson, R. Horne, M. Hudson, J.-M. Jahn, V. Jordanova, S. Kanekal, B. Klatt, B. Larsen, X. Li, E. MacDonald, I. Mann, J. Niehof, T. OBrien, T. Onsager, D. Salvaggio, R. Skoug, S. Smith, L. Suther, M. Thomsen, and R. Thorne (2013), Science goals and overview of the radiation belt storm probes (rbsp) energetic particle, composition, and thermal plasma (ect) suite on nasas van allen probes mission, *Space Science Reviews*, *179*(1-4), 311–336, doi:10.1007/s11214-013-0007-5.

Stix, T. (1992), *Waves in Plasmas*, American Institute of Physics.

Su, Z., H. Zheng, and S. Wang (2009), Evolution of electron pitch angle distribution due to interactions with whistler mode chorus following substorm injections, *Journal of Geophysical Research: Space Physics*, *114*(A8), doi:10.1029/2009JA014269.

Subbotin, D., Y. Shprits, and B. Ni (2010), Three-dimensional verb radiation belt

simulations including mixed diffusion, *Journal of Geophysical Research: Space Physics*, *115*(A3), doi:10.1029/2009JA015070.

Subbotin, D. A., and Y. Y. Shprits (2009), Three-dimensional modeling of the radiation belts using the versatile electron radiation belt (verb) code, *Space Weather*, *7*(10), doi:10.1029/2008SW000452.

Summers, D. (2005), Quasi-linear diffusion coefficients for field-aligned electromagnetic waves with applications to the magnetosphere, *Journal of Geophysical Research: Space Physics*, *110*(A8), doi:10.1029/2005JA011159.

Tao, X. (2014), A numerical study of the excitation of rising-tone chorus using the dawn code, in *General Assembly and Scientific Symposium (URSI GASS), 2014 XXXIth URSI*, pp. 1–1, doi:10.1109/URSIGASS.2014.6929881.

Tao, X., A. A. Chan, J. M. Albert, and J. A. Miller (2008), Stochastic modeling of multidimensional diffusion in the radiation belts, *Journal of Geophysical Research: Space Physics*, *113*(A7), doi:10.1029/2007JA012985.

Tao, X., R. M. Thorne, W. Li, B. Ni, N. P. Meredith, and R. B. Horne (2011), Evolution of electron pitch angle distributions following injection from the plasma sheet, *Journal of Geophysical Research: Space Physics*, *116*(A4), doi:10.1029/2010JA016245.

Thomsen, M. F., M. H. Denton, V. K. Jordanova, L. Chen, and R. M. Thorne (2011), Free energy to drive equatorial magnetosonic wave instability at geosynchronous orbit, *Journal of Geophysical Research: Space Physics*, *116*(A8), doi:10.1029/2011JA016644.

Thorne, R., B. Ni, X. Tao, R. Horne, and N. Meredith (2010), Scattering by chorus waves as the dominant cause of diffuse auroral precipitation, *Nature*, *467*, 943–946, doi:10.1038/nature09467.

Thorne, R., W. Li, B. Ni, Q. Ma, J. Bortnik, L. Chen, D. Baker, H. Spence, G. Reeves, M. Henderson, C. Kletzing, W. Kurth, G. Hospodarsky, J. Blake, J. Fennell, S. Claudepierre, and S. Kanekal (2013a), Rapid local acceleration of relativistic radiation-belt electrons by magnetospheric chorus, *Nature*, *504*(7480), 411–414, doi:10.1038/nature12889.

Thorne, R. M. (2010), Radiation belt dynamics: The importance of wave-particle interactions, *Geophysical Research Letters*, *37*(22), L22,107, doi:10.1029/2010GL044990.

Thorne, R. M., W. Li, B. Ni, Q. Ma, J. Bortnik, D. N. Baker, H. E. Spence, G. D. Reeves, M. G. Henderson, C. A. Kletzing, W. S. Kurth, G. B. Hospodarsky, D. Turner, and V. Angelopoulos (2013b), Evolution and slow decay of an unusual narrow ring of relativistic electrons near l? ?3.2 following the september 2012 magnetic storm, *Geophysical Research Letters*, *40*(14), 3507–3511, doi:10.1002/grl.50627.

Tsyganenko, N. A., and M. I. Sitnov (2005), Modeling the dynamics of the inner magnetosphere during strong geomagnetic storms, *Journal of Geophysical Research: Space Physics*, *110*(A3), doi:10.1029/2004JA010798.

Tu, W., G. S. Cunningham, Y. Chen, M. G. Henderson, E. Camporeale, and G. D. Reeves (2013), Modeling radiation belt electron dynamics during gem challenge intervals with the dream3d diffusion model, *Journal of Geophysical Research: Space Physics*, *118*(10), 6197–6211, doi:10.1002/jgra.50560.

Tu, W., G. S. Cunningham, Y. Chen, S. K. Morley, G. D. Reeves, J. B. Blake, D. N. Baker, and H. Spence (2014), Event-specific chorus wave and electron seed population models in dream3d using the van allen probes, *Geophysical Research Letters*, *41*(5), 1359–1366, doi:10.1002/2013GL058819.

Turner, D. L., V. Angelopoulos, W. Li, J. Bortnik, B. Ni, Q. Ma, R. M. Thorne,

S. K. Morley, M. G. Henderson, G. D. Reeves, M. Usanova, I. R. Mann, S. G. Claudepierre, J. B. Blake, D. N. Baker, C.-L. Huang, H. Spence, W. Kurth, C. Kletzing, and J. V. Rodriguez (2014), Competing source and loss mechanisms due to wave-particle interactions in earth's outer radiation belt during the 30 september to 3 october 2012 geomagnetic storm, *Journal of Geophysical Research: Space Physics*, *119*(3), 1960–1979, doi:10.1002/2014JA019770.

Usanova, M., I. R. Mann, and R. D. Sydora (2010), Generation of Electromagnetic Ion Cyclotron (EMIC) Waves in a Compressed Dayside Magnetosphere, *AGU Fall Meeting Abstracts*, p. D5.

Usanova, M. E., A. Drozdov, K. Orlova, I. R. Mann, Y. Shprits, M. T. Robertson, D. L. Turner, D. K. Milling, A. Kale, D. N. Baker, S. A. Thaller, G. D. Reeves, H. E. Spence, C. Kletzing, and J. Wygant (2014), Effect of emic waves on relativistic and ultrarelativistic electron populations: Ground-based and van allen probes observations, *Geophysical Research Letters*, *41*(5), 1375–1381, doi:10.1002/2013GL059024.

Van Allen, J. A., and L. A. Frank (1959), Radiation around the earth to a radial distance of 107,400 km, *Nature*, *183*, 430–434, doi:10.1038/183430a0.

Walt, M. (1994), *Introduction to Geomagnetically Trapped Radiation*, Cambridge University Press.

Xiao, F., C. Shen, Y. Wang, H. Zheng, and S. Wang (2008), Energetic electron distributions fitted with a relativistic kappa-type function at geosynchronous orbit, *Journal of Geophysical Research: Space Physics*, *113*(A5), doi:10.1029/2007JA012903.

Xiao, F., Z. Su, H. Zheng, and S. Wang (2009), Modeling of outer radiation belt electrons by multidimensional diffusion process, *Journal of Geophysical Research: Space Physics*, *114*(A3), doi:10.1029/2008JA013580.

Xiao, F., Z. Su, H. Zheng, and S. Wang (2010), Three-dimensional simulations of outer radiation belt electron dynamics including cross-diffusion terms, *Journal of Geophysical Research: Space Physics*, *115*(A5), doi:10.1029/2009JA014541.

Xiao, F., Q. Zhou, Z. He, and L. Tang (2012), Three-dimensional ray tracing of fast magnetosonic waves, *Journal of Geophysical Research: Space Physics*, *117*(A6), doi:10.1029/2012JA017589.

Xiao, F., Q. Zhou, Z. He, C. Yang, Y. He, and L. Tang (2013), Magnetosonic wave instability by proton ring distributions: Simultaneous data and modeling, *Journal of Geophysical Research: Space Physics*, *118*(7), 4053–4058, doi: 10.1002/jgra.50401.

Xiao, F., Q. Zong, Y. Wang, Z. He, Z. Su, C. Yang, and Q. Zhou (2014), Generation of proton aurora by magnetosonic waves, *Scientific Reports*, *4*(5190), doi:10.1038/srep05190.

Zhao, H., X. Li, J. B. Blake, J. F. Fennell, S. G. Claudepierre, D. N. Baker, A. N. Jaynes, and D. M. Malaspina (2014), Characteristics of pitch angle distributions of hundreds of kev electrons in the slot region and inner radiation belt, *Journal of Geophysical Research: Space Physics*, *119*(12), 9543–9557, doi: 10.1002/2014JA020386.

Zhou, M., B. Ni, S. Huang, X. Deng, M. Ashour-Abdalla, Y. Nishimura, Z. Yuan, Y. Pang, and H. Li (2014), Observation of large-amplitude magnetosonic waves at dipolarization fronts, *Journal of Geophysical Research: Space Physics*, *119*(6), 4335–4347, doi:10.1002/2014JA019796.